IN-OPERANDO STUDIES OF NEXT-GERATION ELECTROCHEMICAL ENERGY STORAGE SYSTEMS

A Dissertation

Presented to the Faculty of the Graduate School

of Cornell University

In Partial Fulfillment of the Requirements for the Degree of

Doctor of Philosophy

by

Michael Andrew Lowe

August 2012

IN-OPERANDO STUDIES OF ELECTROCHEMICAL ENERGY STORAGE SYSTEMS

Michael Andrew Lowe, Ph. D.

Cornell University 2012

Electrochemical energy storage holds the promise to transform modern society's relationship with energy in ways comparable to previous revolutions in agriculture, transportation, and information. However, significant advances in performance and lifecycle are required in order to utilize several of the most promising chemical systems. Addressing the present limitations requires answering fundamental questions about the how the materials store charge, and the conditions in which they fail. These questions are most directly answered through the study of the materials in their electrochemical environment, and ideally, during the electrochemical reactions (*in-operando*). This study demonstrates the utility of several characterization techniques to probe chemical reactivity within the electrochemical environment, including synchrotron x-ray diffraction, synchrotron x-ray absorption spectroscopy, and confocal Raman spectroscopy. By correlating results from electrochemistry, ex-situ and in-operando spectroscopy and diffraction, and computational modeling, reaction mechanisms can be clarified and failure modes identified. Of particular interest is the application of this approach to the lithium-sulfur system for secondary batteries, where spectroscopy reveals the main reaction pathways and identifies promising new designs for lithium-sulfur energy storage.

BIOGRAPHICAL SKETCH

Michael Lowe is from a ranching family in eastern Montana, and has been surrounded by words as long as he can remember. As a young philologist, he found some of the most unfamiliar and intriguing terms on the lists of chemicals on food boxes, thus starting on the long path into chemistry. After a secondary education in public and parochial schools, Michael attended Michigan State University on a Alumni Distinguished Scholarship and conducted research with Professors Thomas Bieler and Greg Swain in the area of chemical vapor deposited diamond. In the midst of his undergraduate program, he took a two year leave of absence to serve a full-time mission for the Church of Jesus Christ of Latter-day Saints in southeastern Colorado and western Kansas. Since coming to Cornell, Michael has benefited from productive interactions with all of his advisors, Professors Hector Abruña, Frank DiSalvo, and Richard Hennig, as well as with outstanding researchers in the Abruña group, the Cornell community, and abroad. His research has primarily pursued the rational development of materials for electrochemical energy storage, with a heavy emphasis on the application of in-situ characterization methods to probe reaction mechanisms and failure modes. Michael and his wife Jenny are the proud parents of three children, Margaret, Daniel, and Elizabeth, and enjoy gardening, home improvement projects, and serving in the local congregation of their church.

Dedicated to the pursuit of truth and the greater good

ACKNOWLEDGMENTS

I first gratefully acknowledge the love and support of my wife, Jenny, and my three wonderful children, Margaret, Daniel, and Elizabeth. The sweet and eternal joy to be found in coming home to loved ones has been my comfort and incentive, and their sacrifices have made it possible for me to invest time and intellectual capital into this research.

Next must come my appreciation for Professor Abruña. I have witnessed and experienced his paternal concern for the success of his students. He is truly concerned about personal growth of individuals, and often sees more in us (his students) than we see in ourselves. As my academic advisor and tutor, he is responsible for most of the good things I have learned about research, and yet he has also given me the freedom to pursue the questions I felt most compelling. The lessons he has taught and the doors he has opened will be cherished and lifelong blessings for my family. The other members of my committee, Professor DiSalvo and Professor Hennig, have also provided inspiring examples of how to work within a collaborative environment, and have provided important constructive criticism through the course of my research at Cornell.

This research was funded by the Energy Materials Center at Cornell (emc^2) and the generous support of Fuji Heavy Industries, Ltd. My tuition, stipend, and immediate expenses were provided by a National Defense Science and Engineering Graduate (NDSEG) Fellowship, funded specifically by the high performance computing sector of the Department of Defense. It has been a privilege to be a NDSEG fellow, and the organization has provided abundant opportunities for networking and outreach.

My parents, Dan and Laura Lowe, provided the intellectual, spiritual, and physical foundation of this and all of my other endeavors. I will always be grateful for their love, lessons, and steadiness. Their service and instruction to their children has already borne fruit in the eyes of the world and will only become more apparent as the generations grow.

I have had many inspiring teachers during my extended path through academia for which I am grateful. My second grade teacher Miss Rollins encouraged me to push myself mentally even as she put up with childish antics. Karen Davidson (now Woodruff) encouraged and enabled me to get my first publication, a short poem in a children's magazine, and was a steady and reassuring presence in the early years of my education. Middle school came with its attendant vicissitudes, and teachers like Miss Torske were willing to be both teacher and friend. In high school, my close advisor Doc Elison – the only person I knew to have a PhD – was my debate coach, math/science teacher, and philosopher. At Michigan State, Dr. Root-Bernstein broadened my perspectives and encouraged critical thought while I was learning the basics of x-ray methods from Prof. Bieler. Later, as a soon-to-be-married sophomore, Prof. Swain agreed to hire me as an undergraduate researcher, giving me practical experience with electrochemistry and my first in-situ studies on a liquid cell atomic force microscope. I am grateful for all of these teachers, and the many others that I have not specified by name.

At Cornell, I have had many influential teachers that were not professors: Dr. Yasuyuki Kiya and Dr. Jay Henderson were early tutors in battery materials, and Dr. Yi Liu taught me the basics of synchrotron x-ray investigations (including how to

align a six-circle diffractometer). Yasu, in particular, taught me by inspiring example the power of scientific diligence mingled with humility.

I have been blessed to interact with excellent researchers at Cornell, and we have enjoyed a great measure of success over the years. Dr. Jie Gao, Dr. Darren Dale, and Dr. Yasuyuki Kiya have special places in this dissertation, since these men have provided significant intellectual and physical assistance to this research. Dr. Gao, in particular, is responsible for the materials that I have characterized. However, there are also collaborators whose contributions to this work are less tangible, but who have strongly influenced my development. I am especially grateful to have spent my time at Cornell in close association with Dr. Stephen Burkhardt. His keen mind, expansive views, and unique capabilities have set the pace and pushed me to do my best in the graduate program.

Finally, and most importantly, I am grateful for spiritual guidance and the gifts of God. He has given opportunities, and strengthened and nourished me as I have turned to Him for help. During my time in Ithaca and at Cornell, He has been able to turn my imperfect efforts to the benefit of others, and I humbly acknowledge His inspiration and power behind, among, and through all good things that I have been able to accomplish.

TABLE OF CONTENTS

LIST OF FIGURES

LIST OF TABLES

CHAPTER 1

INTRODUCTION

1-1. Motivation and Objectives

Science is a voyage of discovery, and yet, like the intrepid seafarers of history, those of us engaged in science are about something far more noble and urgent than a tourist expedition. We search and research to find new phenomena, to establish a name and claim on valuables, to serve our society and open up new worlds of possibility, and perhaps, because we cannot stand still. We believe that more is possible than has yet been accomplished, that there are beautiful and beneficial discoveries to be made, and we enjoy the adventure and challenge to be had on the voyage.

The analogy to epic stories of discovery is particularly true in the study of materials and systems for energy because of their promise and our society's need. The energy systems developed in the last 300 years have had nearly universal impact on the quality and quantity of life around the world, and are largely responsible for the advent of such technologies as mechanical harvesting, commercial textiles, industrial production, global transportation and communication, and computing along with the Information Age. Combined, the discovery and development of systems for energy storage and conversion have resulted in a median standard of living unparalleled in recorded history. However, the systems of the past have also accrued negative impacts. Today, varied sectors of society call for energy independence, decreased environmental impact, increased stability of existing energy infrastructure and a shift to distributed and renewable energy sources; a set of demands that collectively must be satisfied by developing new energy storage systems. New storage systems will permit expanded use of domestically-produced and locally-sourced solar, wind, and hydroelectric power sources, technologies that are rapidly coming of age but that are

inherently limited to a small fraction of the total energy supply due to the inability to store and regulate electricity within the aging electrical grid. However, the most significant impact will come through the electrification of transportation. Currently, petroleum-powered transportation is the single greatest consumer of energy in the United States.[1] Automakers are gradually increasing production of electric-assisted or battery powered electric vehicles, but it questionable how fast the conversion to electric vehicles will happen without systems that cost less and can provide more energy density.

A number of promising energy storage systems are currently in development utilizing natural resources, mechanical, thermal, electrostatic, or chemical phenomena, each of which has an appropriate place in the future energy landscape. However, the need for portable electrical storage systems with high energy density is most likely to be met by electrical energy storage in chemical processes, which is to say electrochemical energy storage.

This dissertation is not about a dramatic new electrochemical energy storage system, nor about the entire process of developing energy storage systems, but rather illustrates a distinct and critical step in system development. Specifically, this work describes the application of chemically-specific characterization techniques on prototype systems, while the system operates, as a means to identify why the system does or does not work. The objective has been two-fold: first, to develop a broadly-applicable and accessible methodology that can be used to answer chemical questions in both near-term technologies (i.e. systems with imminent commercialization) and promising system concepts. Second, this methodology has been implemented in several interesting materials systems, including but not limited to the exemplary results described in this dissertation, with a special emphasis on the lithium-sulfur system.

1-2. An Introduction to Electrochemical Energy Storage Systems

At the most fundamental level, almost all chemical reactions involve the transfer of electrons, including the combustion of hydrocarbons for transportation and heating: the reduced, electron-rich fuel (carbon and hydrogen, C_xH_y) is oxidized by and rapidly transfers atoms and electrons to an electron-poor oxidant (oxygen) to form the more stable compounds of carbon dioxide (CO_2) and water (H_2O), in the process releasing large amounts of energy. Mechanical engines then attempt to convert that energy into work or electrical power.

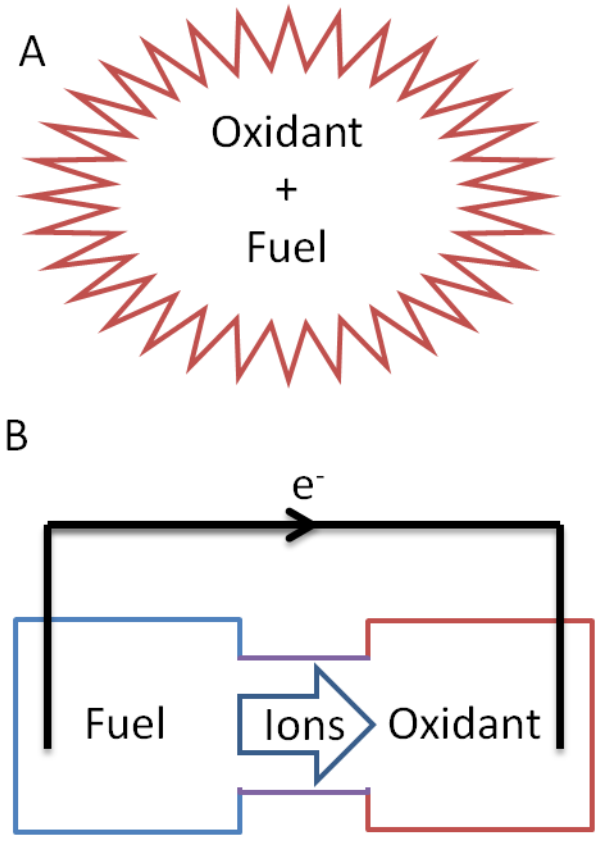

Figure 1-21. Simplified schematic for energy conversion by (A) chemical combustion versus (B) electrochemical reaction.

Electrochemical systems similarly store and release energy through the oxidation and reduction of chemical compounds, but with the critical difference that the electron

transfer event is not spontaneous. Rather, the reaction occurs in half-reactions at defined interfaces, the electrodes, through which the electrons are conducted to an external circuit to perform work, or from which the electrons flow to store energy. In the idealized case of electrochemical hydrocarbon combustion in acidic solutions, the anode would oxidize the hydrocarbon fuel to CO_2 while the cathode would reduce the O_2 to H_2O. Electrons would be transferred through the external circuit at a voltage determined by the difference of thermodynamic stability between the starting and final reaction products, and H^+ ions would transfer through the reaction solution to complete the electronic circuit. The electrochemical system would convert chemical energy to electrical energy.

While most systems are more complex, including any that involve the oxygen reduction reaction, there are a few examples that approach this idealized scenario (e.g. oxidation of formic acid on PtPb). In real systems, the rates of reaction at each electrode are a strong function of the electrode material, the temperature, the chemical composition, and the chemical identity of the oxidant and fuel. In general, the reaction rates tend to decrease with increasing complexity of the chemical oxidation/reduction reaction. The dramatic changes that transpire between the initial hydrocarbon and the final CO_2/H_2O mixture mean that it is very difficult to take electrical energy and convert it back to the original chemical energy at a practical rate. Thus, the oxidation of hydrocarbons system is chemically irreversible, making this system useful for transporting energy but of no use for electrochemical energy storage.

Of much more relevance to energy storage are the often arcane chemistries that are chemically reversible. For example, the most common commercialized lithium-ion battery technology uses graphite and $LiCoO_2$ as reactants. The components are placed in the cell in their stable, discharged states – the states with the least difference in the electron energy in the two dissimilar compounds. Once assembled with electronic

contacts to each electrode and placed in the appropriate ionically conductive electrolyte solution, electrical energy can be applied to drive electrons from the $LiCoO_2$ to the graphite, with lithium ion diffusion in the electrolyte solution completing the circuit. In the charged state, the oxide is deficient in lithium and electrons ($Li_{1-x}CoO_2$), while the graphite has intercalated lithium ions and an excess of energetic electrons (Li_xC_6). This state is thermodynamically less stable (higher energy) than the original compounds: the storage of electrical energy has generated a chemical fuel and oxidant. During battery discharge, the flow of electrons and lithium ions is reversed, reconverting chemical energy to electrical energy. Ideally this reaction could be repeated infinitely, but in practice the materials fail after several hundred cycles from a combination of reactive impurities and structural failure induced by inserting and removing lithium ions.

Table 1-1. Energy densities for commercialized secondary battery systems

Chemical System	*Energy Density (Wh/kg)*
Lead Acid	30-50
Nickel-metal hydride	60-80
Lithium-ion	150-250

The operating principles of electrochemical energy conversion and charge storage can be utilized in two different formats. In battery cells, or batteries, all reactants are contained within the electrochemical reaction volume. If the reaction is irreversible and can only occur a single time, the cell is called a primary battery and is only useful for energy conversion. If the reaction can occur multiple times, then it is called a secondary battery and is a possibility for electrochemical energy storage. Table 1-1 lists a few of the many different chemical systems which have already been developed

for energy storage in secondary batteries. The low formula weight of compounds for lithium-based systems and their high (>3 V) operational voltage make them the highest energy density commercialized battery technology, and the focus of research in this dissertation.

A second format for energy conversion and storage, called a fuel cell, involves moving the fuel and /or oxidant through the electrochemical reaction volume. As with chemical systems for battery cells, primary fuel cell systems are chemically irreversible and intended only for energy conversion, while secondary fuel cell systems are chemically reversible and may be used for electrochemical energy storage. However, since the reactant streams are mobile, the actual device design and evaluation metrics are considerably different. For example, since the reactants need to flow through the electrochemical reactor, both fuel and oxidant need to be soluble or at least stably suspended in fluid media. This is in contrast to battery electrodes, which are solid, immobile matrices of active materials, conductive additives, and polymeric binders. A fuel cell decouples energy density, a property of the reactant solutions, from device power output, which can be controlled by design of the electrochemical reactor, and is a very promising concept for attaining future high energy density electrochemical energy systems. While this dissertation is focused on understanding the chemical reactivity of proposed compounds within the geometric and materials constraints of operational secondary battery cells, many of the techniques and concepts addressed herein are also applicable to the study of operational secondary fuel cells.

1-3. Next-Generation Lithium-Based Energy Storage Systems

Commercialized lithium-ion battery electrodes almost universally store charge via ion intercalation into crystalline structures. For these topotactic reactions, the crystalline

framework both directs and participates in the charge storage process, with the fastest rates and longest cyclability coming from crystalline systems that undergo minimal structural changes during the ionic insertion/deinsertion process (e.g. lithium titanate, $Li_4Ti_5O_{12}$). However, this requirement inherently limits the theoretical capacity by the mass of the crystalline host (e.g. CoO_2 or $Li_4Ti_5O_{12}$) and, in general, no more than one electron can be stored per formula unit. Indeed, for $LiCoO_2$, the practical capacity is limited to approximately half the theoretical value to avoid irreversible chemical and structural degradation.[2]

Table 1-2. Properties of proposed next-generation cathode and anode materials for lithium-based batteries. Capacity based on specified chemical composition.

Material	Theoretical Capacity (mAh/g)	Lithiation Voltage (V vs. Li/Li+)
	Cathodes	
$LiCoO_2$	140	3.8
S_8	1670	2.05
O_2	3350	2.9
FeF_2	571	1.8
	Anodes	
Graphite	372	0.1
Si	4200	0.2
Ge	1620	0.5
Mn_3O_4	700	0.5
Li	3865	0.0

On the other hand, the most promising chemical systems for future energy storage involve chemical reactions between lithium and chemical compounds and do not preserve the original crystalline lattice. Next-generation cathodes are based on

reactions with electronegative molecules[3] or fluorides,[4] while anodes utilize reactions with lithium and group IV elements[5] or transition metal oxides.[6] Table 1-2 shows the specific capacity and lithiation voltage for several of these materials, as often reported in the literature. Many of these materials have been investigated with promising reports of charge storage capacities and operational voltages, at least during the first lithiation/delithiation cycle with a lithium counter electrode. The first cautionary note regarding the materials is found in their chemical composition – with the exception of the lithium anode, none of the next-generation materials natively contain lithium.

Table 1-3. Effect of electrode materials on the specific capacity of the energy storage system.

	Graphite	*Mn_3O_4*	*Metallic Li*
$LiCoO_2$	100	115	140
S_8	282	439	1170

Since these materials access multiple electrons per formula unit, they promise dramatic gains in capacity (>10X that of existing lithium-ion batteries). However, these gains are only realized when they are coupled with another next-generation electrode material. Table 1-3 shows simple capacity calculations for systems composed from commercialized materials (graphite and $LiCoO_2$) and/or next-generation cathode and anode materials investigated in this dissertation. Despite the impressive capacities for the individual materials, it is clear that the actual improvements are more modest if conventional and next-generation electrode materials are used in the same cell. Thus, for a cell with a $LiCoO_2$ cathode, the specific capacity of the system only increases by 15% if a graphite anode is replaced by Mn_3O_4, even though the capacity of the anode nearly doubles. This is because the cell capacity is limited by the poor capacity of $LiCoO_2$. Since energy storage systems are

indeed systems, they cannot defined by a single exceptional material – and if dramatic capacity improvements are desired, it is necessary to develop cathodes and anodes with dramatically increased capacity.

1-4. Understanding Reactions in Complex Energy Storage Systems

Invariably, the increase in capacity comes with significantly increased mechanistic complexity of the charge storage reaction. The 'conversion reactions' of many metal oxides are illustrative: during lithiation, the often crystalline transition metal oxides transform to a mixture of metallic nanoparticles and lithium oxide (Li_2O), and this mixture then transforms back into a metal oxide during delithiation. For the specific case of MnO, the overall reaction has been reported to follow the equations:[7]

$$MnO + 2Li^+ + 2e^- \leftrightarrow Li_2O + Mn$$

There is no simple reaction step that can accomplish this combination of structural and chemical changes. Conversion reactions proceed at room temperature and reasonable rates, despite requiring significant ionic mobility and the unexpected chemical reactivity of Li_2O, and many groups have observed lithium storage capacities that are consistently as high – or even higher – than the theoretical capacity for the expected conversion reaction.[6,8,9]

Unfortunately, electrochemical signals are sensitive but not selective, and so purely electrochemical methods are insufficient to study the complex reactions of next-generation electrode materials. Additional chemical characterization is required to confirm that the charge passed is due to the desired reaction and to confirm the identity and distribution of products. This is particularly true because of the highly reactive species and electrochemical conditions associated with the charge storage events, and the often incomplete understanding of how these conditions affect the prototype cell components. Thus, it is possible to misinterpret complex chemical

reactivity as chemically reversible[10] (or irreversible[11,12]) charge storage. These misconceptions will be clarified by the development and implementation of methods that can more carefully detect chemical processes within batteries.

It is common to characterize the reaction of battery materials ex-situ, that is, after removing the active material from the battery at a specific state of charge. This approach is sufficiently informative to answer many questions about the reactions in lithium-ion batteries, since the crystalline compounds are unlikely to change when removed from the solvated, electrochemical environment. However, this assumption is no longer valid for some of the next-generation electrode materials. Both sulfur and oxygen establish multiphase equilibria during cell operation, and these equilibria can only be probed by in-situ characterization of the cathode materials.

In-situ studies of battery materials provide valuable chemical insights, even when the active material is not involved in a solution-phase equilibria, by enabling the collection of complementary electrochemical and spectroscopic datasets. This effectively increases the dimensionality of the acquired data, improving the ability to extract chemically relevant information from the combined experiment. As discussed through the chapters of this dissertation, several analytical techniques can be applied to electrodes within operational devices. To distinguish these multidimensional datasets from operational cells, this dissertation refers to the approach and results as being *in-operando.* While *in-operando* studies are not novel, they are increasingly necessary to address the chemical complexity of next-generation energy storage systems and to develop chemically-informed approaches to battery design, testing, and characterization.

1-5. Dissertation Overview

This chapter provides a brief introduction to the motivations for and approaches to high energy density electrochemical energy storage.

Chapter 2 summarizes the materials and methods used for the experiments described throughout the dissertation, except as noted in the individual chapters.

Chapter 3 presents a synchrotron x-ray study characterizing the structural and chemical changes that occur in a manganese oxide anode material for lithium-based batteries. This study introduces the tools for data analysis of x-ray diffraction and x-ray absorption spectroscopy and demonstrates the need for multiple techniques to understand the complex chemical transformations that occur during conversion reactions. X-ray absorption spectroscopy is shown to be a valuable technique for understanding chemical and structural changes in complex systems because of its sensitivity to all atoms of the element of interest. Correlation of electrochemical and spectroscopic datasets prove that a significant fraction of the charge storage is not associated with the expected reactions of manganese, raising serious questions about the reactions occurring at other metal oxide conversion anodes.

Chapter 4 is a critical overview discussing how several common analytical techniques can be applied to study chemical reactions and species within operational sulfur-based batteries. Where available, examples of in-operando studies are reviewed for each of the techniques (electrochemistry, UV-Vis absorption spectroscopy, confocal Raman, x-ray diffraction, and x-ray absorption near edge spectroscopy). Evaluation of the techniques reveals that confocal Raman is an attractive technique to address unanswered questions about the mechanism and failure modes of lithium-sulfur batteries.

Chapter 5 presents results from an electroanalytical study of the sulfur reduction mechanism in lithium-containing electrolyte solutions. Through the use of multiple

techniques and quantum chemical modeling of the polysulfides, the early stages of the reduction are shown to proceed via an undiscussed pathway involving long chain radical anions, while the later stages of sulfur reaction are dominated by slow chemical equilibria that are difficult to probe using electroanalytical methods.

Chapter 6 is a combined study using x-ray diffraction (XRD) and sulfur K edge x-ray absorption near edge spectroscopy (XANES) to understand the reaction mechanism of sulfur cathodes with a gel polymer electrolyte. Both techniques show the reversibility of the sulfur reaction during galvanostatic cycling. In-operando XRD reveals the appearance of crystalline lithium sulfide at the end of discharge, while in-operando XANES is able to resolve a limited number of key dominant sulfur species that are present during both discharge and charge processes. The radical anion S_3^- is shown to play a significant role in the reaction mechanism of sulfur cathodes.

Chapter 7 uses optical images to demonstrate how the widely varying solubility of sulfur species in battery electrolytes makes coin and pouch cell battery formats inappropriate for systematic studies of lithium sulfur batteries. A new electrochemical cell design is presented that avoids the pitfalls of traditional cell designs, and also permits study of sulfur in solvents that are unstable at lithium surfaces. This cell will enable fundamental studies of the limiting rates for sulfur reduction.

Chapter 8 discusses general conclusions for the dissertation and proposes several promising directions for additional in-operando studies of lithium-sulfur chemistry. This chapter also presents a list of publications authored during the course of this study.

REFERENCES

(1) Annual Energy Review 2009, *Energy Information Administration*, **2009**.

(2) Manthiram, A.; Choi, J. *Journal of power sources* **2006**, *159*, 249–253.

(3) Bruce, P. G.; Freunberger, S. A.; Hardwick, L. J.; Tarascon, J.-M. *Nat. Mater.* **2011**, *11*, 19–29.

(4) Li, H.; Balaya, P.; Maier, J. *J. Electrochem. Soc.* **2004**, *151*, A1878.

(5) Chan, C. K.; Zhang, X. F.; Cui, Y. *Nano Lett.* **2008**, *8*, 307–309.

(6) Cabana, J.; Monconduit, L.; Larcher, D.; Palacín, M. R. *Advanced Materials* **2010**, *22*, E170–E192.

(7) Fang, X.; Lu, X.; Guo, X.; Mao, Y.; Hu, Y.-S.; Wang, J.; Wang, Z.; Wu, F.; Liu, H.; Chen, L. *Electrochem. Commun.* **2010**, *12*, 1520–1523.

(8) Wang, H.; Cui, L.-F.; Yang, Y.; Sanchez Casalongue, H.; Robinson, J. T.; Liang, Y.; Cui, Y.; Dai, H. *J. Am. Chem. Soc.* **2010**, *132*, 13978–13980.

(9) Gao, J.; Lowe, M. A.; Abruña, H. D. *Chem. Mater.* **2011**, *23*, 3223–3227.

(10) Freunberger, S. A.; Chen, Y.; Peng, Z.; Griffin, J. M.; Hardwick, L. J.; Barde, F.; Novak, P.; Bruce, P. G. *J. Am. Chem. Soc.* **2011**.

(11) Kiya, Y.; Iwata, A.; Sarukawa, T.; Henderson, J. C.; Abru\ na, H. D. *J. Power Sources* **2007**, *173*, 522–530.

(12) Gao, J.; Lowe, M. A.; Conte, S.; Burkhardt, S. E.; Abruña, H. D. *Chemistry–A European Journal In Press*.

CHAPTER 2

EXPERIMENTAL METHODS

2-1. Electrochemistry

Electroanalytical studies were performed using a potentiostat/galvanostat (HSV-100, Hokuto Denko) with digital signal acquisition. Before use, glassy carbon electrodes were polished with 3 sizes of Al_2O_3 powder (1.0, 0.3, and 0.05 micron, in that order), rinsed with highly purified water (>18 MΩ, Millipore), then sonicated in water for at least 5 minutes. Electrodes were then rinsed with acetone and dried on a kimwipe before use. Solutions of sulfur and lithium bis(trifluoromethanesulfon)imide (LiTFSI) electrolyte in tri(ethylene glycol) dimethylether (triglyme) were prepared in an Ar-purged glovebox (Vacuum Atmospheres) at least 12 hours prior to ensure solubilization of sulfur. For rotating disk electrode experiments, solutions were transferred out of the glovbox immediately prior to experiment and the headspace in the electrochemical cell purged with nitrogen before and during data acquisition. Chronoamperometry and cyclic voltammetry experiments were performed inside the glovebox using an electrical feedthrough. All experiments were conducted using a Ag/(50 mM Ag^+) reference electrode in triglyme and referenced to the potential for metallic Li in this solution (-3.4 V vs. Ag/Ag^+).

Constant current potentiometry experiments were performed on in-operando battery cells with either the HSV-100 in galvanostat mode or a Versastat 3 (Princeton Applied Research) galvanostat. The applied current rates were kept low relative to the capacities to maintain quasi-equilibrium conditions in the electroactive material, with an approximate ratio of electrode capacity to rate near 20 (e.g. 30 mA/g for Mn_3O_4, 80

mA/g for sulfur). Battery cells were prepared with either 150 or 200 microliters of electrolyte solution, distributed within the cell in the following manner: 100 microliters on the cathode, 50 microliters on the separator underneath the anode, and 50 microliters on the nickel foam spacer (not between the electrodes). All experiments with coin cells were performed with either a 1:1 volume mixture of ethylene carbonate:diethylcatbonate (EC:DEC) or tetra(ethylene glycol) dimethylether (TEGDME) and 1 M of either LiTFSI, lithium trifluoromethanesulfonate, lithium hexafluorophosphate, or lithium perchlorate.

2.2 In-Situ Coin Cells

In-situ battery cells were prepared by drilling ~3 mm diameter holes in the coin cell casing and epoxying 0.003" (x-ray absorption) or 0.05" (x-ray diffraction) thick kapton on the outer side of the casing. The epoxy (Chemgrip Bonding Kit) was carefully distributed around the hole in the casing prior to placing the window, then carefully pressed to insure uniform coverage over the entire cofacial region. Coin cell casings were then dried for at least 3 days at elevated temperature (90C) prior to use. The casings for the Mn_3O_4 study (Chapter 3) were used after this drying step; the casings for the sulfur study were coated with 50 nm of Al using a bell jar vacuum evaporator. All cells were prepared in an Ar-filled glovebox with oxygen and moisture levels below 0.5 ppm, then stored in an Ar environment until immediately before use. The Mn_3O_4 cells were also contained in a He-purged bag during battery operation.

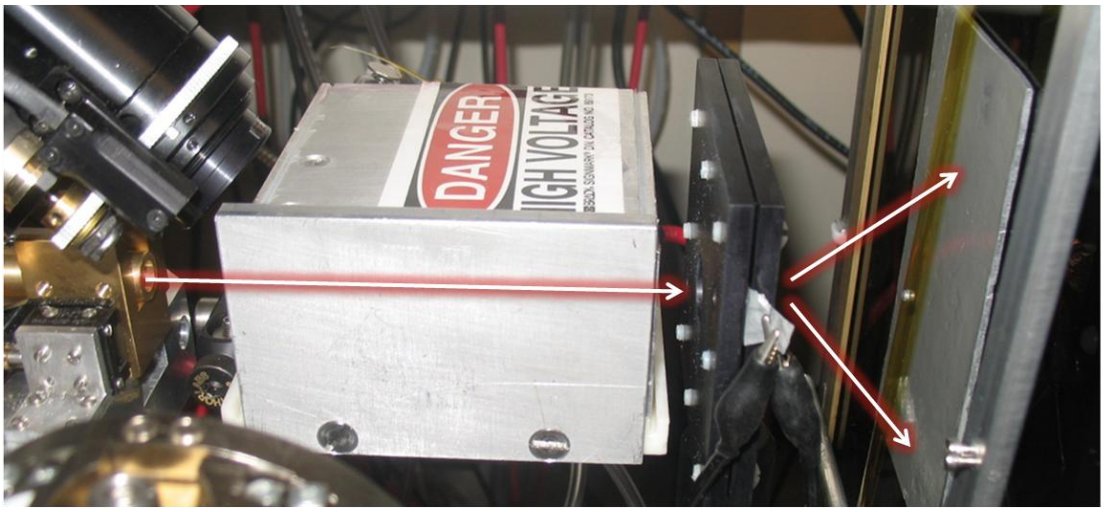

Figure 2-22. Scattering geometry for synchrotron x-ray diffraction studies. Beam path highlighted in white. Incident x-ray beam size was defined by upstream slits (not visible) and the flux measured by a nitrogen-purged ion chamber in center of image. The direct beam was blocked by a small lead beamstop mounted on kapton tape. Diffraction was collected on two-dimensional detector.

Electrical contact to the in-situ coin cells was made using two stainless steel washers pressed against the anode and cathode casings, respectively, and not on the kapton windows.

In-situ spectra were collected as the electrode was lithiated/delithiated at slow rates. While this introduced some ambiguity about the precise state of charge for the spectroscopic result, this imprecision was small because of the ratio between acquisition time (seconds to minutes) and total reaction time (hours).

2.3 X-Ray Diffraction

X-ray diffraction was conducted at either beamline F3 or beamline A2 of the Cornell High Energy Synchrotron Source (CHESS). Data were acquired in transmission geometry using a two dimensional detector, either a Quantum 4U from Area Detector Systems Corporation or large amorphous Si detector from General Electric Medical

Imaging. Figure 2-1 is an image of the typical setup for working at 10 keV incident energy at beamline F3, with typical sample-detector distances near 10 cm. At A2, the higher incident energy (30 keV) and the larger pixel size of the GE detector required working at much longer distances (60-70 cm). Exact sample-detector distance was calibrated using a ceria standard and the program Fit2D.

Datasets were integrated radially using the program Fit2D before being exported as one dimensional diffraction spectra. Background subtraction was then performed. In the case of sulfur diffraction, a spectrum with intermediate state of charge was used as the background, since under typical conditions there were no peaks from crystalline sulfur or lithium sulfide in this regime. In the case of Mn_3O_4, a custom, piece-wise background spectrum was assembled using the following rules:

1. For spectral regions without any diffraction peaks from the phase(s) of interest, an arbitrary spectrum was selected to be used directly as the background.
2. For spectral regions with a transient peak that completely appears or disappears, a spectrum in which the peak was not apparent was used for background.
3. For spectral regions where diffraction peaks are always present from a phase of interest, a linear background was defined between the end-points of the spectral regions on either side.

In some cases, additional fitting of diffraction peaks was done using Origin 8.5 and either a Lorentzian or a Gaussian profile, and in the case of Mn_3O_4, a Williamson-Hall analysis was performed using WinPlotr, part of the FullProf x-ray analysis software suite.

Typical exposure times for diffraction images ranged from 3-30 s, and between

diffraction images, the beam was blocked for periods of 300-600 s. Because of the long time period of data acquisition (~5-10 hours per battery half-cycle), collection of spectra every 5-10 minutes still provided sufficient time resolution.

2.4 X-Ray Absorption Spectroscopy

X-ray absorption spectroscopy (XAS) was collected at beamlines F3 at CHESS (Mn_3O_4 work) and X19A at the National Synchrotron Light Source (NSLS) for the sulfur studies. Data for the Mn_3O_4 study was collected in transmission mode with ion chambers to monitor incident and transmitted x-rays. For the sulfur XAS, data was acquired by measuring the x-ray fluorescence on a large diameter (3000 mm^2) passivated implanted planar silicon (PIPS) detector located ~ 4 cm from the electrode cell. The cell was contained in a He-purged environmental chamber and the PIPS detector was mounted on the chamber wall. All datasets were processed using Athena, part of the IFEFFIT software package.

Each XAS measurement required 5-15 minutes. A common procedure is to collect multiple (>3) XAS measurements for a given electrode state in order to improve counting statistics. However, for the data shown in this dissertation, the signal to noise was sufficiently high that no signal averaging was employed. This has both logistical and statistical motivations. Logistically, it is difficult and inefficient to interrupt the battery operation as many times as would be required to obtain equivalent resolution (~9 mAh/g per spectra). Statistically, multiple spectra per point would be warranted if the data were significantly improved by the signal averaging. However, averaging adjacent spectral datasets did not change the trends apparent in the waterfall plots. Indeed, the presence of a systematic trend in the spectral datasets strongly suggests a

low level of noise in the data. If necessary the trend can be fit to the appropriate functional form, and the reliability of the fit will still be determined by the total signal in the dataset.

2.5 Raman Spectroscopy

Confocal Raman data (Chapter 4) was collected using a Renishaw InVia spectrometer with a 488 nm Argon laser. Before beginning coupled electrochemical and spectroscopic data acquisition, spectra were acquired with increasing incident intensities to identify the onset of radiation damage. For polysulfides in solution, this was typically at 50% of the maximum laser intensity, so later experiments were performed at 10% of the maximum laser intensity. During extended data acquisition on a sample surface, the laser spot was manually rastered over the sample area using a remotely controlled sample stage.

2.6 Computational Methods

Quantum chemical studies of polysulfides were performed at the level of density functional theory. An expanded basis set was used (6-311++g(2df)) to account for the presence of diffuse electron density around the sulfur atoms; however, similar results were obtained using a contracted basis set. Initial geometries were defined using molecular mechanics (MMFF94, as implemented in Avogadro 1.0.3), further relaxed using a semi-empirical model (PM6, as implemented in MOPAC 2009), and then relaxed without symmetry constraints in Gaussian ’03. Gaussian ’03 calculations were performed on a high performance computational cluster at the Cornell Nanofabrication Facility. Rendering of molecular orbitals was performed using Avogadro 1.0.3 on a personal computer.

2.7 Materials and Resources

Unless otherwise noted, all materials were used as received, and were of the highest purity available from Sigma-Aldrich. TEGDME was further dried before use by equilibrating for at least 7 days over anhydrous 4 angstrom molecular sieves.

Several specialized resources available at the Cornell Center for Materials Research (CCMR) were used during cell fabrication and testing. These included air furnaces (drying and electrode preparation) and a bell vacuum evaporation system for deposition of aluminum on in-situ cell windows.

CHAPTER 3

IN-SITU X-RAY STUDIES OF THE CONVERSION REACTION IN MN_3O_4 LITHIUM BATTERY ANODES

3-1. Introduction

The pursuit of next-generation energy storage systems has identified several materials which can access multiple electrons per formula unit, including O_2 and S_8 cathodes and anodes from carbon group elements or metal oxides, all of which have theoretical capacities that are 3-10 greater than the $LiCoO_2$/graphite materials currently commercialized. However, the increased capacity comes with significantly increased reaction complexity. While traditional materials for lithium-ion batteries utilize lithium intercalation into crystalline frameworks and achieve optimal performance with minimal structural alterations during cycling, proposed conversion materials react during lithiation to form entirely new products, often with dramatically different structure and chemistry, and with reaction mechanisms that are still incompletely understood.[1,2] For example, several metal oxides are proposed to react between the following end-points, which clearly do not have a simple elementary step:

$$M_xO_y + 2yLi^+ + 2y\,e^- \rightarrow xM + yLi_2O$$

Metal oxides have been investigated for lithium battery electrodes since at least the early-1980s,[3–5] with initial interest in intercalation[3,4] or conversion[5] reactions at high temperatures. However, reports that selected systems could react at room temperature[6] with apparently theoretical capacities[7] have motivated many additional researchers to study the conversion reactions of metal oxides. Metal oxides remain some of the most

promising materials for next-generation lithium battery anodes due to their high gravimetric capacity, with manganese and iron oxides receiving particular attention due to the abundance, low mass, and low cost of the corresponding elements. However, the dramatic structural and chemical changes during the conversion reaction make it difficult to clearly distinguish the limitations imposed by the mechanism and practical losses from initial particle morphology, synthetic approaches, and electrode preparations. For example, several recent reports[8–10] have identified Mn_3O_4 as an interesting anode material, with reversible capacities near 800 mAh/g and reversible cycling over tens of cycles, while previous[3,11,12] and concurrent[13] studies of the oxide found poorer performance. Additional characterization is necessary to verify the active reactions and distinguish between practical and mechanistic limitations of the system.

Other researchers have studied the reaction mechanism of metal oxide anodes, including Mn_3O_4, but using ex-situ techniques.[10,13] Several recent publications from the Chen group investigated the reaction mechanism of Mn_xO_y compounds,[13–15] with most oxides proposed to store lithium through a related sequence of reactions. In the case of Mn_3O_4, the following pathway was proposed:

$$Mn_3O_4 + Li^+ + e^- \rightarrow LiMn_3O_4 \quad (1)$$

$$LiMn_3O_4 + Li^+ + e^- \rightarrow Li_2O + 3MnO \quad (2)$$

$$MnO + 2Li^+ + 2e^- \rightarrow Li_2O + Mn \quad (1^{st} \text{ discharge}) \quad (3)$$

In subsequent cycling, charge storage involved only MnO and metallic Mn:[15]

$$Li_2O + Mn \leftrightarrow MnO + 2Li^+ + 2e^- \quad (4)$$

These results demonstrated that the first lithiation of the Mn_3O_4 will always have some irreversible lithium insertion due to formation of the first formula unit of Li_2O (2 e^-/

Mn_3O_4, or 234 mAh/g). However, the authors also observed a large irreversible capacity loss during the first lithiation of MnO that was not explained by reaction 4. Moreover, the best performance of Mn_3O_4 anodes exhibited a first discharge capacity (>1200 mAh/g) and reversible capacities (~800 mAh/g) that are larger than predicted by this series of reactions.[8,9,16] The complexity of the conversion process, together with the increased chemical reactivity and sensitivity of most reduced/lithiated species to ambient conditions,[15] requires in-situ characterization to verify the reaction pathway and to assign electrochemical features with specific reactions. Ultimately, the increased use of in-situ characterization techniques can unravel differences in capacity between materials with similar composition and morphology.

X-ray diffraction (XRD) and x-ray absorption spectroscopy (XAS) are particularly well suited for these in-situ studies. Hard x-rays ($h\nu$ >>1 keV) interact weakly with matter, enabling x-rays to probe electrode layers buried within operational battery cells.[17] Diffraction provides phase-sensitive information about long-range order and absorption spectroscopy yields elementally-resolved information about chemical state and short-range order. Thus, a detailed understanding of structural changes is possible by combining the information from both techniques. Moreover, the high flux available at synchrotron radiation sources permits datasets to be acquired from operating cells (*in-operando*).[18–20] In the case of lithium-ion batteries, the time for x-ray data acquisition is much faster than the lithiation reaction and mechanistic insights can be gained by correlating the time-dependent spectral and electrochemical features.[21]

The typical voltage transient for the first galvanostatic lithiation/delithiation cycle of a Mn_3O_4 anode is shown in Figure 3-1. The features shown in Figure 3-1 are consistent in number and voltage with other reports of Mn_3O_4 anodes, although the exact length

and slope differ slightly between reports.[9,11,13,22] Several distinct phases are apparent during the first discharge, including two quasi-plateaus above 0.7 V (phase I), an extended voltage plateau near 0.5 V vs. Li/Li^+ (phase II), and a sloping voltage in the final stages of lithiation (phase III). The total charge passed during the first lithiation of this electrode is near 11 electrons per Mn_3O_4, or 3 e^-/Mn_3O_4 more than expected from reactions 1-3. In contrast, subsequent delithiation of the manganese oxide exhibits a sloping voltage transient with the dominant feature being a quasi-plateau near 1.5 V (phase IV), with a total of approximately 7 e^-/Mn_3O_4 extracted. This again exceeds the theoretical capacity expected from reaction 4. In-situ studies will play an important role in both verifying the proposed reactions and explaining the nature of the additional charge storage.

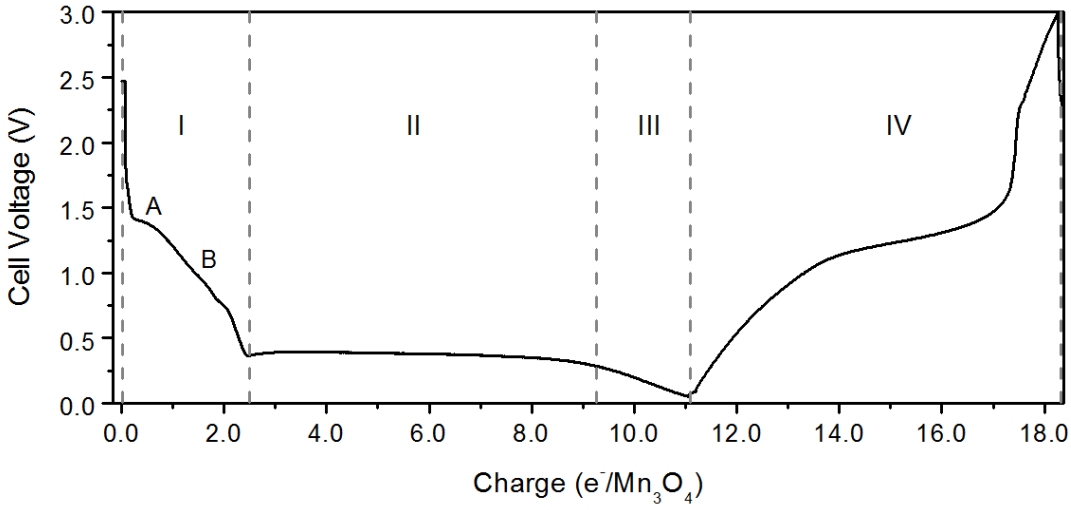

Figure 3-1. Electrochemical voltage profile during first lithiation and delithiation of Mn_3O_4.

Below, we present *in-operando* synchrotron diffraction and spectroscopic results during the first galvanostatic lithiation/delithiation cycle of a Mn_3O_4 anode. The results provide new insights into the series of reactions and make possible assignments

to specific electrochemical features. In-operando XAS clearly shows that a significant fraction of the charge is stored in non-Mn-centered reactions, a result with serious implications for the results reported for Mn_3O_4 and other metal oxide conversion anodes.

3-2. Experimental Setup:

Mn_3O_4 was prepared using a precipitation-calcination method and cast into electrodes on a copper current collector, as reported previously.[9] The electrode matrix consisted of 70 wt.% Mn_3O_4, 20 wt.% carbon black (Super P-Li, Timcal Ltd.), and 10 wt.% poly(vinylidene difluoride). Typical electrodes had loadings of 3-4 mg/cm^2 of Mn_3O_4. In-situ x-ray cells were made from stainless steel CR2032 coin cell casings by drilling 3 mm holes and mounting 125 micron kapton windows with epoxy (Chemgrip, Aetna Plastics). Cells were assembled in an argon-filled glovebox using lithium metal as the anode, a Celgard 2320 separator, and an electrolyte of 1 M $LiPF_6$ in ethylene carbonate (EC)/ diethyl carbonate (DEC) (1:1 by volume). Cells were stored in argon-filled, hermetically-sealed vials during transport to the synchrotron beamline, and during experiments the cells were enclosed in a helium-purged bag. Galvanostatic lithiation/delithiation was performed using a Versastat 3 potentiostat (Princeton Applied Research) with voltage cutoffs at 0.01 and 3.0 V.

Synchrotron powder x-ray diffraction studies were conducted at beamline A2 of the Cornell High Energy Synchrotron Source (CHESS) using Si(111) monochromator

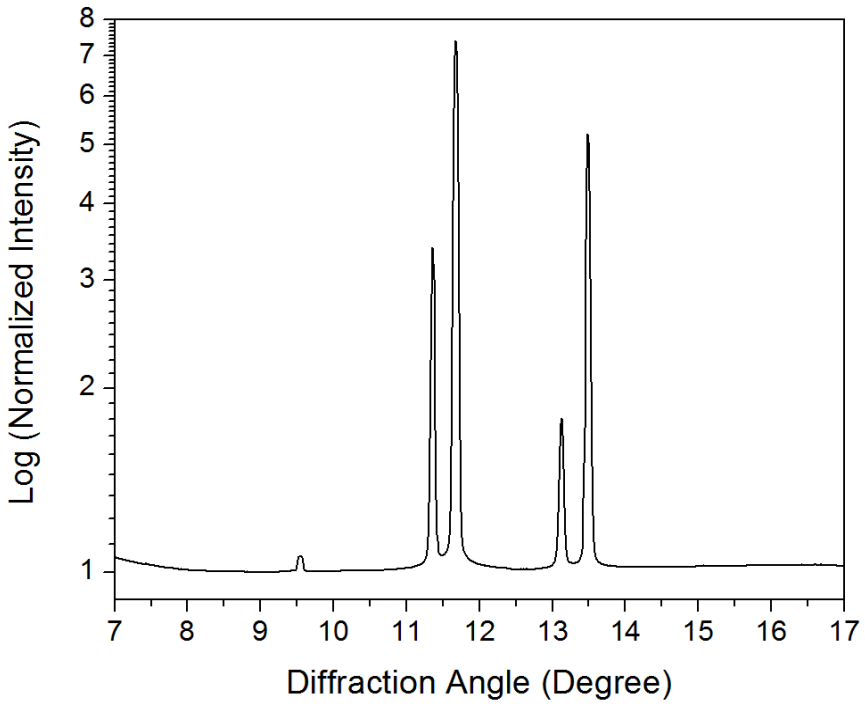

Figure 3-2. Piecewise-constructed background for Mn_3O_4 diffraction dataset.

crystals. Diffraction experiments were conducted in transmission geometry at 30 keV incident energy using a large area amorphous silicon detector (General Electric). Two dimensional data were radially integrated using Fit2D,[23] normalized by the background counts at 8.9 degrees, and background subtracted using a piecewise-constructed profile (Figure 3-2) to obtain data for analysis. Selected peaks were fit using a Lorentz function with a linear background to obtain peak areas and widths. Domain sizes were calculated using the Scherrer equation with an instrumental correction, as determined by the diffraction from microcrystalline CeO_2. Williamson-Hall analysis was performed using the software WinPlotr. X-ray absorption spectra were collected at CHESS beamline F3, in transmission geometry, by scanning the

energy over the range of 6439-7400 eV, and subsequently background subtracted and normalized with the Athena software package.[24]

3-3. In-Operando X-ray Diffraction

Previous studies based on ex-situ XRD proposed that during phase I Mn_3O_4 is reduced to MnO via an $LiMn_3O_4$ intermediate (reactions 1 and 2). The cell voltage during this phase does show two distinct trends (Figure 3-3A, phases IA and IB) with a total capacity near 2 e^-/Mn_3O_4, as expected from two reaction stages to form MnO (Figure 3-1B). However, closer inspection of the electrochemical results raises questions about this assignment. Electrochemically, the cell discharge shows that most of the lithium storage occurs during the sloping phase (IB), unlike the equal capacity anticipated from a serial sequence of reactions 1& 2. Unfortunately, the changed slope in discharge voltage could be due to one of several kinetic or mass transport conditions, including slow charge transfer kinetics, poor charge (electronic or ionic) transport, or increasing electronic resistance between the particles. Additional characterization is needed to distinguish fundamental (e.g. mechanistic) and practical limitations, and since the Mn_3O_4 has crystalline domains, XRD provides straightforward and sensitive insights to the crystallographic changes.

During phase IA, the plateau associated with the first 0.5 e^-/Mn_3O_4, the in-operando XRD results show a monotonic decrease in the area of Mn_3O_4 diffraction peaks as reaction 1 proceeds (Figure 3-3C). Interestingly, the change is not linear, and the derivative (dA/dQ) of the peak change emphasizes that the initial charge storage (<0.25 e^-/Mn_3O_4, before the voltage reaches the plateau) does not consume Mn_3O_4 at the same rate as during the remainder of phase IA. The reaction over this charge

interval is due to amorphous manganese oxides on the particle surfaces and grain boundaries, as detected previously by Raman[9] and evidenced by the higher cell voltage. By extrapolation of the linear change in peak height to 0 e^-/Mn_3O_4 and assuming $1e^-$ per formula unit of amorphous oxide, this amorphous oxide is estimated to contribute 5-10% of the capacity from crystalline Mn_3O_4.

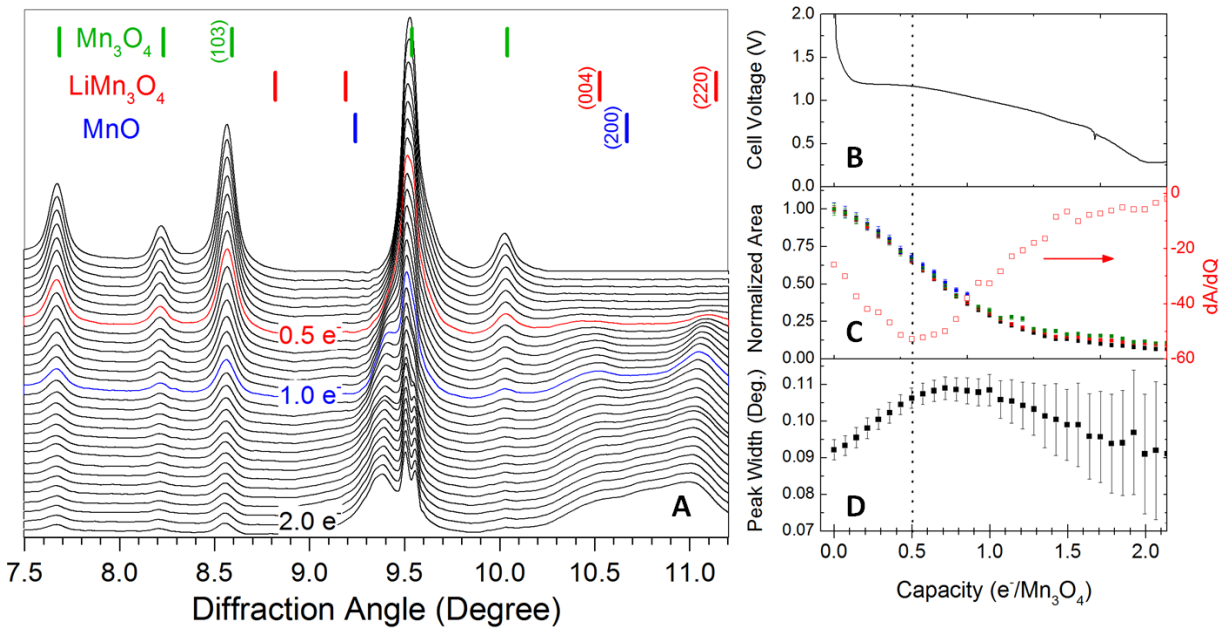

Figure 3-3. X-ray diffraction during Phase I. A. Waterfall plot of spectra. B. Electrochemical voltage profile over the charge storage interval. C. Variation in normalized area of peaks from Mn3O4: (103), black; (200), red; (112), green; (004), blue. Open symbols, derivative in (103) peak area with respect to charge. D. Variation in peak width for (103) reflection.

After 0.25 e^-/Mn_3O_4, the change in Mn_3O_4 peak area remains roughly linear through the rest of phase IA consistent with charge storage dominated by the reaction of Mn_3O_4. By the end of phase IA (0.5 e^-/Mn_3O_4), the peak area is at 66% of its original value (Figure 3-3C) and the diffraction peaks widths have markedly increased. (Figure 3-3D) A Williamson-Hall analysis confirmed that this change is a consequence of both increased strain and a 16% decrease in Mn_3O_4 domain size. Although somewhat

speculative on our part, these changes are consistent with a surface-limiting reaction mechanism, where the lithiation occurs at the surface of the Mn_3O_4 nanocrystals and propagates until limited by diffusion (~2 nm, as estimated from the change in domain size). The relative decrease in peak area (-34%) and domain size (-16%) is also consistent with the reaction of particle surfaces: if the nanoparticles were spheres, a 13.3% change in diameter would represent 35% of the total particle volume. Finally, newly appearing diffraction peaks from $LiMn_3O_4$ in this lithiation range exhibit an (004) peak at 10.5 degrees, shifted due to significant (0.9%) tensile strain along the c axis. (Figure 3-3A) The combination of tensile strain in the c axis of $LiMn_3O_4$ and decreased Mn_3O_4 crystalline domain size further support a mechanism in which reduction occurs first and preferentially at the surface of the nanoparticles.

The limitation of the reaction to the nanoparticle surfaces is likely due to differential ionic transport in the two phases. $LiMn_3O_4$ exhibits significantly higher (~100x) electronic conductivity than Mn_3O_4,[25] but the relative ionic transport may be far worse. From a structural perspective, Mn_3O_4 is a distorted spinel with a 2D network of tunnels formed by stabilization of the Mn^{2+} ions on tetrahedral sites. These tunnels enable facile lithium insertion during the first part of reaction 1 and a corresponding voltage plateau. However, once the surfaces are converted to crystalline $LiMn_3O_4$ the Mn^{2+} ions shift to neighboring octahedral sites, closing the tunnels and decreasing the lithium ion mobility to the nanoparticle cores. (Figure 3-4)

During the 1.5 e^-/Mn_3O_4 of charge storage in phase IB the voltage continuously decreases from 1.2 to 0.3 V, providing little electrochemical evidence of distinct chemical processes, but once again in-operando diffraction is able to provide additional mechanistic information. Between 0.5-1.0 e^-/ Mn_3O_4 there is a linear

decrease in Mn_3O_4 volume (Figure 3-3C) but insignificant shifts in Mn_3O_4 peak positions and widths (Figure 3-3D). This indicates that during this phase the reaction proceeds through the reaction of entire Mn_3O_4 domains and not a progressive thickening of the $LiMn_3O_4$ shell. It is possible that intraparticle stresses provide the driving force for the fragmentation and reaction of individual domains. Over this range of charge storage, the $LiMn_3O_4$ peaks become more pronounced (Figure 3-3A) but the peak width remains relatively constant, with a nanoparticle size as estimated from the Scherrer equation of 13-14 nm.

It is significant that approximately 25% of the crystalline Mn_3O_4 remains even after passing 1 e^-/Mn_3O_4 (Figure 3-3C), suggesting that a concurrent reaction is responsible for some charge storage during phase IB. This is also reflected in the diminishing dA/dQ for the Mn_3O_4 peaks as the reaction proceeds. A careful inspection of the diffraction data shows concurrent growth of the $LiMn_3O_4$ peaks and poorly resolved peaks at the positions expected for MnO (Figure 3-3A). Furthermore, between 0.5-1.0 e^-/Mn_3O_4 there are opposing shifts in (004) and (220) $LiMn_3O_4$ peak positions (10.5 and 11.1 degrees, respectively) as tensile strain decreases along the c axis and increases along the a axis, both of which are consistent with the strain induced by the formation of MnO (Table 1). Together, these results show that even in the early stages of phase IB the charge storage involves both reactions 1 and 2. The higher electronic

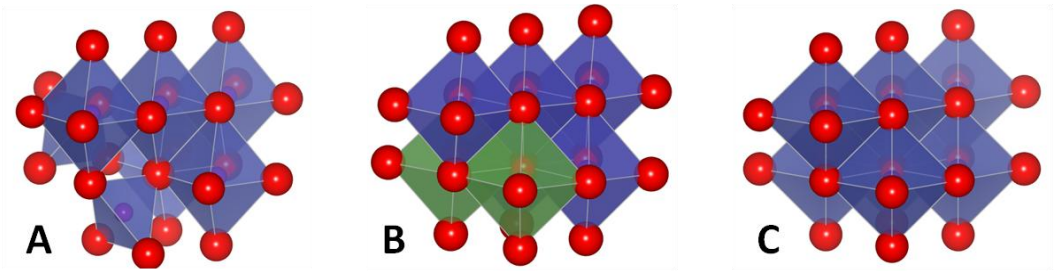

Figure 3-4. Local Structure of manganese oxides present during lithiation of Mn_3O_4. Blue polyhedral are manganese-centered; green octahedra are occupied by either Mn^{2+} or Li^+. (A) Mn_3O_4 (B) $LiMn_3O_4$ (C) MnO

Table 3-1. Lattice parameters for manganese oxides during lithiation of Mn_3O_4.

Oxide Lattice Parameter	Mn_3O_4	$LiMn_3O_4$	MnO*
a	5.762	6.022	6.286
c	9.439	9.010	8.890

* To simplify comparison, the unit cell of cubic MnO (a = 4.445 angstroms) is defined by the same coordinate system as the tetragonal Mn_3O_4 and $LiMn_3O_4$.

conductivity of $LiMn_3O_4$[25] may favor its concurrent reduction to MnO, especially if the remaining Mn_3O_4 is shielded by a layer of ionically-resistive $LiMn_3O_4$.

Through the final 1 e^-/Mn_3O_4 of phase I, all three oxides are present but constantly changing in relative phase fraction. Mn_3O_4 peak areas decrease but at a continually diminishing rate, while the peaks from $LiMn_3O_4$ and MnO both increase with the peaks from MnO becoming more distinct over this interval. Most notably, there is a progressive shift in the $LiMn_3O_4$ (220) peak to lower angles, (Figure 3-3A) indicating an increasing tensile strain along the a, b axes as the equatorial Mn-O bond lengths increase. (Table 1) This equalization of Mn-O bond lengths is a consequence of reducing Mn^{3+} ions in $LiMn_3O_4$, eliminating the Jahn-Teller distortion induced by the high spin d^4 Mn^{3+} ion, and results in the formation of cubic MnO from tetragonal $LiMn_3O_4$. The continual shift of this peak, along with the invariant position of the MnO (200) peak, suggests that reduction of the $LiMn_3O_4$ nanoparticles involves structural evolution to MnO rather than nucleation and growth of a distinct phase within the nanoparticles. Interestingly, the reduction of $LiMn_3O_4$ to MnO involves *delithiation* of the oxide, possibly forming a highly defected rock salt structure. The

structural conversion may be facilitated by a tolerance for cation vacancies on octahedral sites within the MnO phase.[26,27]

The XRD data for the remaining discharge provides somewhat ambiguous conclusions. Diffraction peaks from Mn_3O_4 and $LiMn_3O_4$ persist beyond 5 e^-/Mn_3O_4, eventually being replaced by a broad peak for MnO near 10.7 degrees (estimated domain size ~4 nm) (Figure 3-5). Diffraction peaks from MnO slowly decrease throughout the discharge but never disappear. An abrupt change in the background after 8 e^-/Mn_3O_4, though partially obscured by the Cu (111) peak from the current collector, is consistent with the appearance of very small domains of Mn (~2-3 nm, as estimated from the Scherrer equation). (Figure 3-5) Similar nanoparticle sizes have been observed in fully-reduced electrodes of other metal oxides.[7] Surprisingly, diffraction from Li_2O is not observed at any point in the discharge, in contrast to a previous ex-situ XRD study.[13] This may be a consequence of forming amorphous Li_2O and/or the low scattering cross-section for Li_2O at the incident photon energy of 30 keV.

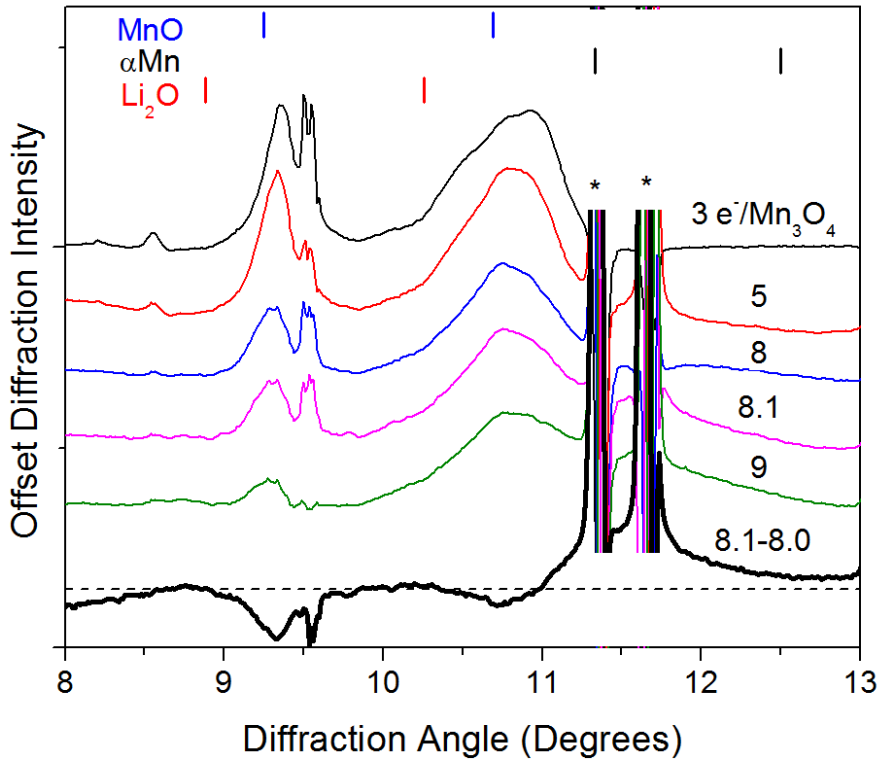

Figure 3-5. Variation of XRD during Phase II, labeled by the charge passed before diffraction, together with a bold line showing the difference between diffraction at 8.0 and 8.1 e^-/Mn_3O_4 showing the abrupt appearance of metallic Mn. Diffraction lines marked by asterisks are from Cu and Ni cell components. The horizontal dashed line indicates zero for the difference spectrum.

The persistence of crystalline Mn_3O_4 and $LiMn_3O_4$ beyond the end of phase I is a somewhat surprising result not expected from reaction 2, but is consistent with some of the previous ex-situ XRD studies in the literature[28] and may be a consequence of poor electronic contact (i.e. isolated Mn_3O_4 nanoparticles) or slow reaction kinetics. Unfortunately, the sensitivity of diffraction to ordered phases, and the increasing amorphization of the oxide through each reaction, means that these XRD results may not accurately represent the relevant electrochemically-active species in the later stages of lithiation. These results also provide a valuable caution: detection of crystalline oxides with diffraction is necessary but not sufficient to prove that the

electrochemically active material is crystalline, particularly when nanoparticles are prepared using precipitation and low temperature calcination as in the case of several of the best-performing manganese oxide anodes. [8,9] Under these conditions, the diffraction from a small fraction crystalline material can disguise the progress of the dominant reaction in the amorphous fraction.

3-4. In-Operando X-Ray Absorption Spectroscopy

Phase I

The presence of amorphous manganese oxide increases the importance of using XAS, which probes the local structure for all atoms of the element of interest. Since XAS signals are averaged over the local chemical environment for all irradiated atoms of a given element (e.g. Mn), the technique requires a limited number of predominant chemical states and structures to give distinct and tractable responses.[29] However, the dependence on chemical state and short-range order makes it ideal to probe changes between disordered and weakly ordered structures, such as those found in the later stages of the Mn_3O_4 lithiation.

Figure 3-6 presents the XAS dataset for phase I of the lithiation. Similarly to the XRD results, two trends are apparent in the data. The first 0.5 e^-/Mn_3O_4 primarily shows a decrease in intensity for signals at 1.3 and 2.3 angstroms that agree with, respectively, the signals from Mn-O bonds in MnO_4 tetrahedra and the Mn-Mn distances between adjacent octahedral and tetrahedral sites. This demonstrates that through phase IA, Mn moves out of tetrahedral sites into an octahedral, $LiMn_3O_4$-like environment. Thackeray et al. have predicted a cooperative displacement of Mn^{2+} from tetrahedral

sites even at very low local concentrations of Li^+ (0.04 Li^+/Mn_3O_4).[3] The XAS data demonstrates that this transition has occurred to an appreciable extent before storing 0.5 e^-/ Mn_3O_4 and that almost all the Mn^{2+} have moved to octahedral sites by 1.0 e^- /Mn_3O_4. Spectra after 1.0 e^-/Mn_3O_4 have two distinct peaks in the Fourier-transformed EXAFS (FT-EXAFS) data from equatorial Mn-O (4 nearest neighbors resulting in the more intense peak at 1.3 angstroms) and axial Mn-O (2 nearest neighbors, peak at 2 angstroms). This transition matches the first discharge plateau, supporting the conclusion that the sloping discharge in phase IB is due to slower lithium diffusion in the $LiMn_3O_4$ structure, where the lithiums must hop between randomly placed octahedral sites, relative to lithium diffusion in the tunnels of Mn_3O_4.

The corresponding XANES data (Figures 3-6B and 3-6C) are sensitive to both the structural and chemical changes during phase I and supports the transformations observed in the EXAFS. During the first electron per Mn_3O_4, the main peak shifts 1.8 eV to lower energies as the electron density on the Mn ions increases, passing through an apparent isosbestic point in the process at 6558 eV that indicates this reaction involves two local environments. The pre-edge feature, due to a spin-forbidden transition from hybridized s-d states and thus particularly sensitive to local geometry,[30] decreases throughout this period as Mn^{2+} ions shift from tetrahedral to octahedral sites, with most of the change occurring during the first 0.5 e^-/Mn_3O_4 (Phase IA).

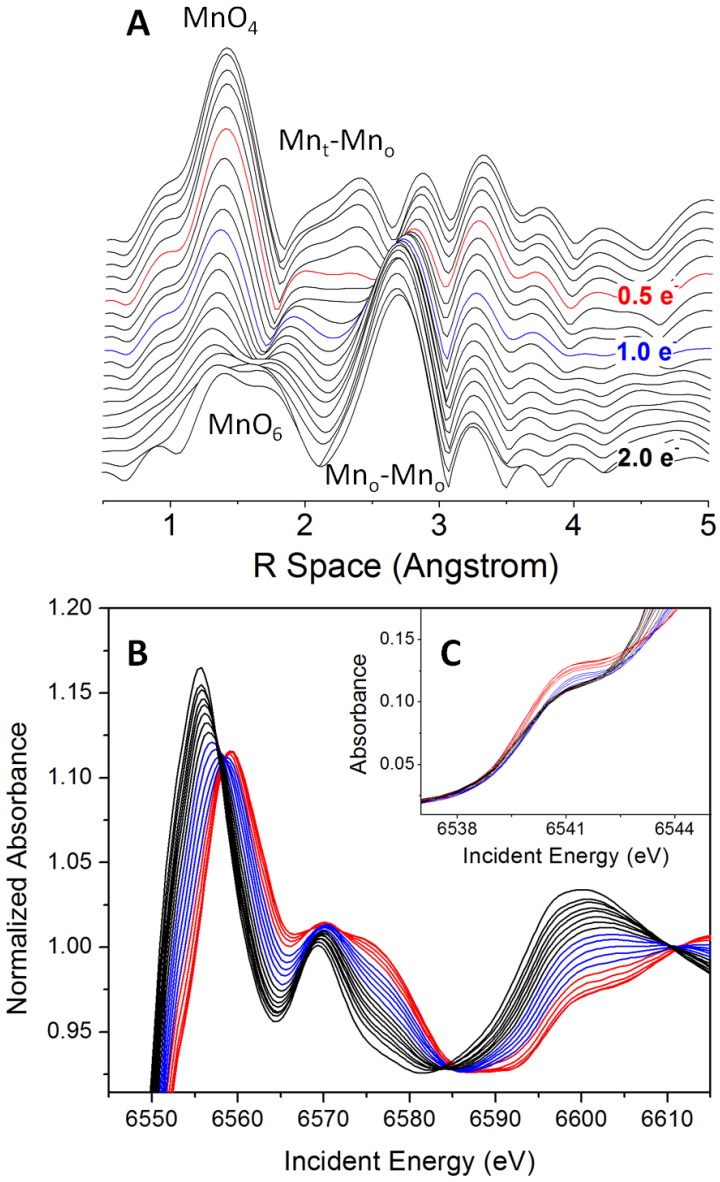

Figure 3-6. XAS dataset during Phase I. (A) EXAFS (B) XANES (C) XANES pre-edge feature. For (B) and (C), red, blue, and black lines are during the charge intervals 0.0-0.5, 0.5-1.0, and 1.0-2.0 e^-/Mn_3O_4.

As shown in the XRD results, the remainder of the high voltage region (phase IB) involves both additional lithiation to obtain the $LiMn_3O_4$ local structure and the reduction of $LiMn_3O_4$ to MnO (reactions 1 and 2). There is some variation in the slope reported during phase IB for different samples of Mn_3O_4,[8–10,13] but since we predict

this depends on lithium mobility in the oxide, the shape of the voltage profile should be sensitive to a number of parameters including the discharge rate, degree of crystallinity and particle morphology. Indeed, the least sloping voltage profile is reported for particles with a thin, plate-like morphology[13] that should have a higher surface to volume ratio than the more spherical nanoparticles in this report.

Both EXAFS and XANES show continuous changes throughout phase IB. Figure 3-6A shows that in the FT-EXAFS, the two peaks from radial and axial Mn-O distances merge to become a single peak by the end of phase IB, with most of the shift from decreasing the axial Mn-O bond. This agrees with the increase in the $LiMn_3O_4$ (220) d-spacing during the same reaction phase (Figure 3-3A). There is also a notable increase in scattering from Mn^{2+} in adjacent octahedral sites (peak at 2.8 angstroms), indicating that during reaction 2 there is concomitant phase separation of Li_2O and ordering of the remaining Mn^{2+} ions. It is likely that the extraction of Li^+ from the $LiMn_3O_4$ matrix forms defect clusters that facilitate Mn^{2+} diffusion and ordering.[27,31]

The corresponding XANES data for phase IB shows another 1.8 eV downshift in main peak position due to reduction of the final Mn^{3+} to Mn^{2+}. (Figure 3-6B) This matches the shift observed during the reduction of the first Mn^{3+}, and is associated with a distinct set of isosbestic points at 6557.7 and 6610.4 eV as the manganese ions shift to the more symmetric MnO local structure. The pre-edge feature (Figure 3-6C) does not change during this period, indicating that all the manganese ions remain in octahedral sites.

Phase II

Charge storage in phase II is proposed to occur from reaction 3, the formation of metallic Mn and Li_2O, which should consume 6 electrons per Mn_3O_4, and the lower voltage plateau for the nanosized Mn_3O_4 is indeed close to this length. At the beginning of phase II, the XANES[15,32] (Figure 3-8) and FT-EXAFS[15] (Figure 3-9) data are consistent with literature reports of MnO, indicating that most Mn ions are in a locally-ordered MnO structure. By the end of phase II, the spectral features have become more like metallic Mn, in broad agreement with the predicted reactions during this voltage plateau.

However, a closer examination of the spectral changes with charge storage provides insights into the specific sequence of reactions. Particularly interesting is the presence of non-manganese-centered reactivity. In the XANES region, for example, the spectra are essentially invariant for 1.7 e^-/Mn_3O_4 (200 mAh/g) as can be seen by the overlapping black lines in Figure 3-8A, indicating that the reaction is not a reduction in the manganese oxidation state. Even the derivative of the pre-peak, a sensitive probe of oxidation state,[30] exhibits no change in position during this charging region (Figure 3-7). The FT-EXAFS does track a slight but systematic increase in the peak height (Figure 3-9C) and sharpness (Figure 3-9A) at 1.5 angstroms over this region due to increased ordering of the O^{2-} ions in the MnO structure, but the changes in local structure could be a time-dependent relaxation rather than proof of Mn-centered reactions. This non-metal-centered reactivity is consistent with unexpectedly extended main lithiation plateaus in several other reports for Mn_3O_4,[8,9,11] as well as other manganese[13,14] and transition metal[7,33,34] oxides.

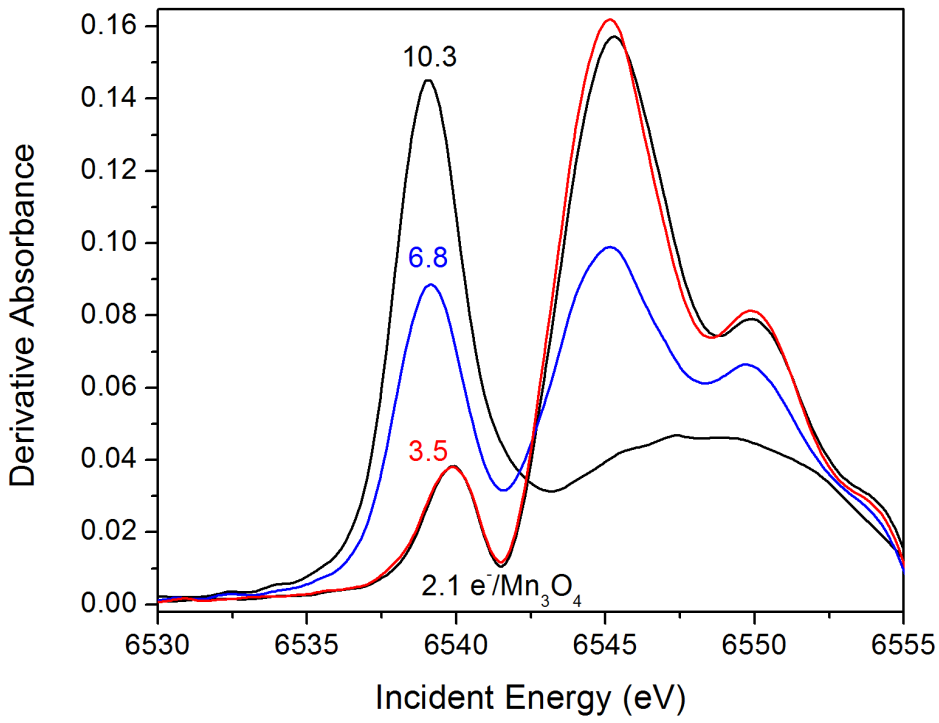

Figure 3-7. Variation in derivative of pre-edge as a function of charge passed.

The non-manganese-centered charge storage is almost certainly due to a catalyzed reduction of the solvent at the surface of the strongly basic MnO nanoparticles. Although not investigated at room temperature, ethylene carbonate is known to be catalytically polymerized under basic conditions.[35] Careful inspection of the potential transient over this regime reveals a nucleation-like dip followed by a slowly rising cell voltage as the solvent reduction is initiated and gradually saturates all the catalytically-active surface sites, creating a polymeric network among the metal oxide nanoparticles. This explanation is consistent with reports from the Tarascon group that discharged CoO forms a partially ionically and/or electronically conductive "polymer/gel-like coating," with spectral features consistent with the carbonate

solvents,[34] that is sufficiently thick to transform loose powders into freestanding films.[34] Although previous researchers have ascribed solvent reduction to the final stages of lithiation based on TEM of discharged electrodes,[34] we are not aware of any studies that have focused on the initial portion of the plateau. It must be emphasized that the charge associated with this process constitutes a significant fraction (~15-20%) of the total charge stored during the first lithiation.

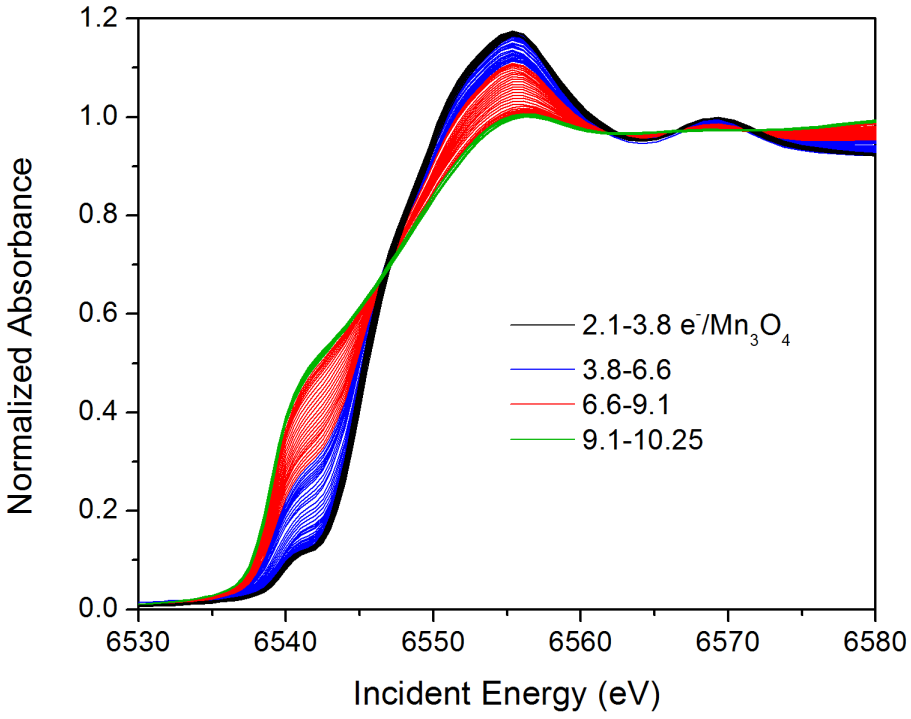

Figure 3-8. XANES data during Phase II-III, colored to show distinct trends over specified charge intervals.

On the other hand, over the next 5.3 e^-/Mn_3O_4 the XAS results clearly show a change in oxidation state and Mn-centered local order. In the XANES, the pre-edge feature of MnO can be seen to downshift in energy and increase intensity throughout the reduction, consistent with formation of metallic Mn and the associated s-p

hybridization of metallic bonding. The results also show clear isosbestic points at 6547, 6561, 6566, and 6571 eV throughout the lithiation (Figure 3-8A), indicating that manganese ions are changing between only the two distinct chemical environments of MnO and Mn. A closer inspection of the XANES as a function of charge suggests two types of reactivity: from 3.8-6.6 e^-/Mn_3O_4 there is a shift of the rising edge to lower energy and slight decreases in oscillation amplitude above the edge, while from 6.6-9.1 e^-/Mn_3O_4 there is a continuous decrease in oscillation amplitude with minimal changes in rising edge position. These trends suggest that the reaction during this plateau is not a simple equilibrium between MnO and metallic manganese, but that metallic Mn is only formed after MnO is sufficiently reduced.

The FT-EXAFS results show similar trends in the local structure. Throughout the range of 3.8-9.1 e^-/Mn_3O_4, there is a steady and concurrent decrease in peaks from within MnO_6 octahedra (1.5 Å, Mn-O) and between adjacent octahedral sites (2.7 Å, Mn-Mn) as seen in Figure 3-9C. Interestingly, metallic Mn bonds do not appear until storing 4.5 e^-/Mn_3O_4 in the second plateau, or alternately, since the first 1.7 e^-/Mn_3O_4 of the plateau is due to non-metal reactions, ~1 e^-/MnO. At this point, there is an abrupt change in the spectra: a new peak appears from Mn metal (2.2 Å, Mn-Mn) and the peak from adjacent MnO_6 octahedra shifts to longer distances (Figure 3-9A) at the same time that both peaks from octahedrally-coordinated Mn become more intense. The peak intensity from within MnO_6 octahedra also increases relative to the inter-octahedral peak intensity, indicating a decreased ordering of the MnO_6 octahedra. (Figure 3-9C) Together, the coulometric and EXAFS data indicate that after the Mn^{2+} is reduced to Mn^{1+}, there is a phase separation of MnO and metallic Mn clusters. This is significantly (~1.3 e^-/Mn_3O_4) earlier than the abrupt appearance of Mn nanoparticles

in the diffraction results because XAS probes the early stages (metallic bond formation) whereas XRD detects the establishment of long-range order (~10 bond lengths).

Passing additional charge results in a coordinated decrease in peaks from MnO_6 and increase in the peak from metallic Mn up to ~9 e^-/Mn_3O_4, when essentially all spectroscopic evidence for MnO_6 has disappeared. If the first 1.7 e^- of the plateau is non-Mn centered, then 9 e^-/Mn_3O_4 corresponds to a charge storage of 1.7 e^-/MnO, about 15% less than predicted by the full reaction 3. It is possible that some oxidized Mn remains in the electrode with a local environment that is too disordered to result in a distinct spectral feature, especially in the final stages of lithiation ($[Mn^{x+}]/[Mn^0] < 0.1$).

Phase III

The only spectroscopic change during the final phase of electrochemical reduction (beyond 9 e^-/Mn_3O_4) is a slight increase in the EXAFS peak intensity from metallic Mn (Figure 3-9C). It is tempting to associate all of the remaining charge with reduction of highly disordered manganese oxide, since this would result in ~6 e^-/Mn_3O_4 of manganese reduction during the second plateau and an excellent agreement (within 3%) of what is expected from reaction 3. However, the spectroscopic dataset cannot quantitatively assign the stored charge to metallic Mn formation. Considering the high surface area of the nanoparticles and the capacitance from a probable surface

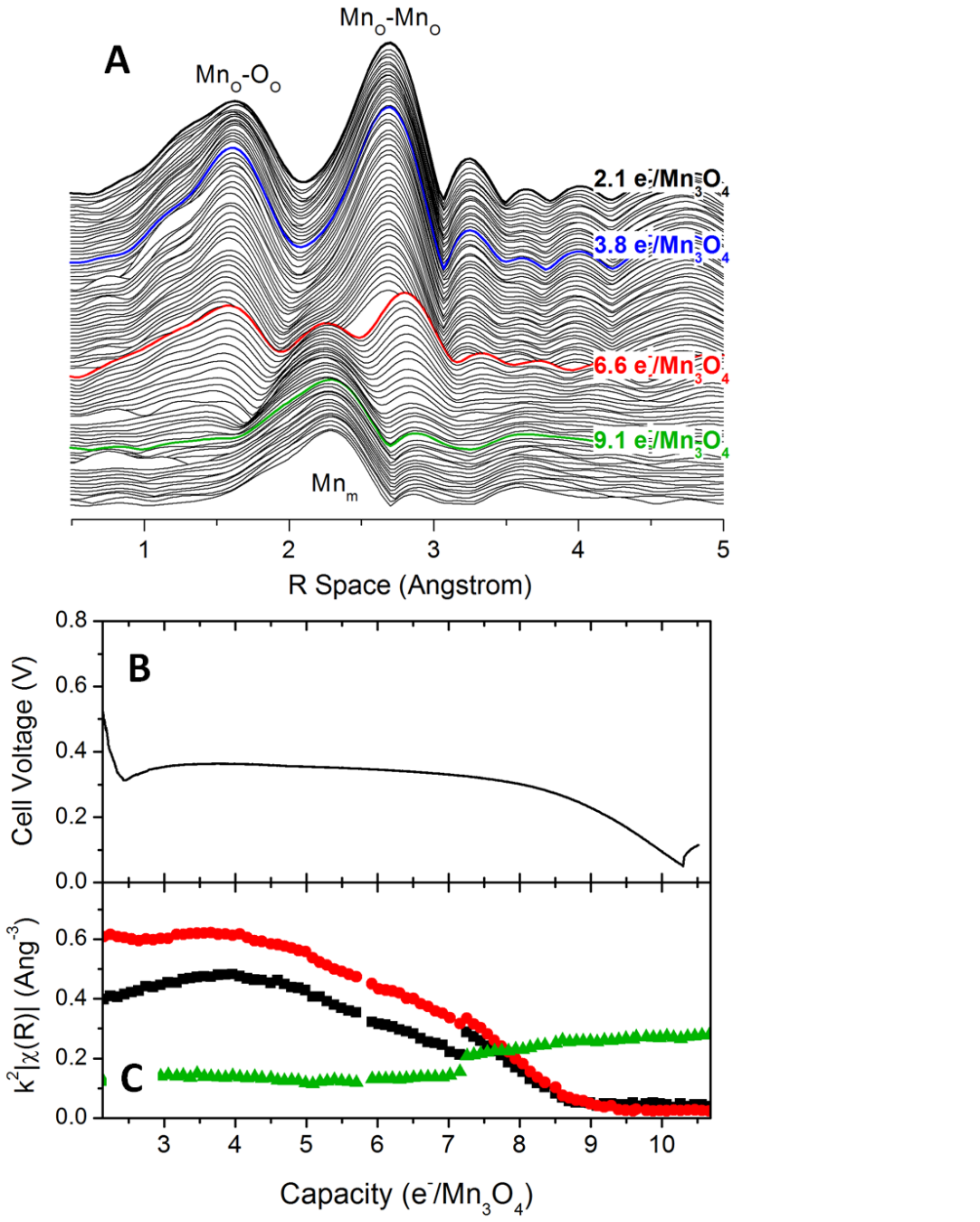

Figure 3-9. FT-EXAFS data during phase II-III. (A) Waterfall plot of data showing decrease in peaks from MnO-like structure and abrupt appearance of metallic bonds at 6.6 e-/Mn3O4. (B) Cell voltage and (C) EXAFS intensity for peaks at 1.5 Å (black, octahedral Mn-O), 2.7 Å (red, Mn-Mn in MnO), and 2.3 Å (green, Mn-Mn in metallic Mn).

film, as well as the slight changes in the XAS dataset, it is probable that phase III is due to both Mn and non-Mn reactivity. Several other researchers have proposed that this sloping voltage is due to reversible film formation,[34] irreversible solvent decomposition,[11] or capacitance at nanoparticle surfaces.[36] Additional spectroscopic techniques (e.g. electron spin resonance[37]) with greater sensitivity to Mn^{2+} ions may further distinguish how much charge storage is metal-centered.

The first delithiation (Figure 3-1) and subsequent lithiation cycles[9] exhibit only sloping voltage plateaus with capacities near 800 mAh/g, indicating a significant difference in reaction mechanism following the initial lithiation. Based on the capacity from with non-Mn reactions during the first discharge, it is reasonable to expect a significant fraction of subsequent capacity is also non-Mn centered. Indeed, observation of the FT-EXAFS shows that there are minimal structural changes until extraction of ~1 e^-/Mn_3O_4, roughly consistent with the charge stored in the phase III of lithiation (Figure 3-10A). This suggests that a significant fraction (10-15%) of the charge cycled is non-Mn centered even at low charge/discharge rates. Since the sloping features represent an increasing fraction of the total response at higher cycling rates,[8,9] this result emphasizes the role of non-metal-centered reactivity at conversion electrode materials and further underscores the need for in-situ probes to insure that the desired reaction is actually occurring.[38]

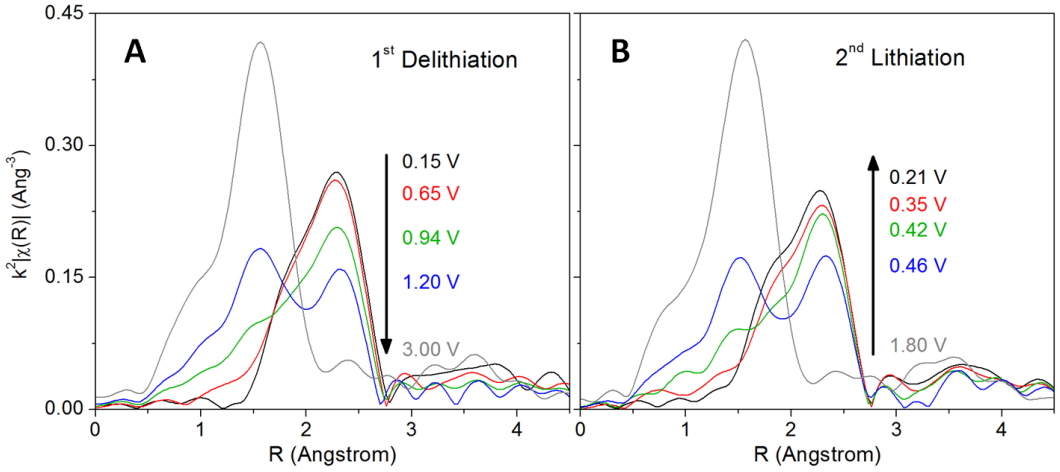

Figure 3-10. Variation of EXAFS at selected voltages during (A) the first delithiation and (B) second lithiation.

Phase IV and beyond

Through the remaining delithiation, the XAS datasets demonstrate that metallic manganese is oxidized to form a MnO-like local structure, with a decrease in FT-EXAFS peaks from metallic Mn at the same time there is an increase in a peak at 1.5 A from Mn-O. (Figure 3-10A) The new oxide peak matches the peak at the start of phase II due to MnO_6 octahedra. (Figure 3-9A) However, the absence of any peaks at longer distances indicates that the octahedra are heavily disordered. A subsequent discharge observed a reconversion between the local structures of MnO_6 and metallic Mn (Figure 3-10B) confirming that subsequent Mn-centered cycling is between these two essentially amorphous endpoints, as predicted in reaction 4. XANES spectra also showed a clear isosbestic point at 6547 eV, consistent with Mn toggling between two distinct chemical states throughout the lithiation/delithiation cycle (Figure 3-11). This limits the Mn-centered charge storage to 6 e^-/Mn_3O_4 (700 mAh/g), with at least ~100 mAh/g contributed by capacitance or electrolyte reactivity.

3-5. Proposed Mechanism and Discussion

The conversion reaction mechanism for Mn_3O_4 is outlined schematically in Figure 3-12. During the first lithiation, the higher voltage profile is due to reactions of specific and progressively more amorphous manganese oxides, roughly in the sequence Mn_3O_4 →$LiMn_3O_4$ → MnO, with the final conversion step involving reduction of MnO to Mn. The x-ray techniques provide additional insights into the sequence of reactions: XRD demonstrates that Mn_3O_4 surfaces react first, with concurrent reduction of both Mn_3O_4 and $LiMn_3O_4$ throughout most of the higher voltage regime, while XAS shows metallic Mn does not appear until the reduction of Mn^{2+} to Mn^{1+}. Subsequent cycling extends between amorphous endpoints, but with additional capacitive contributions that add to the apparent reversible capacity. This

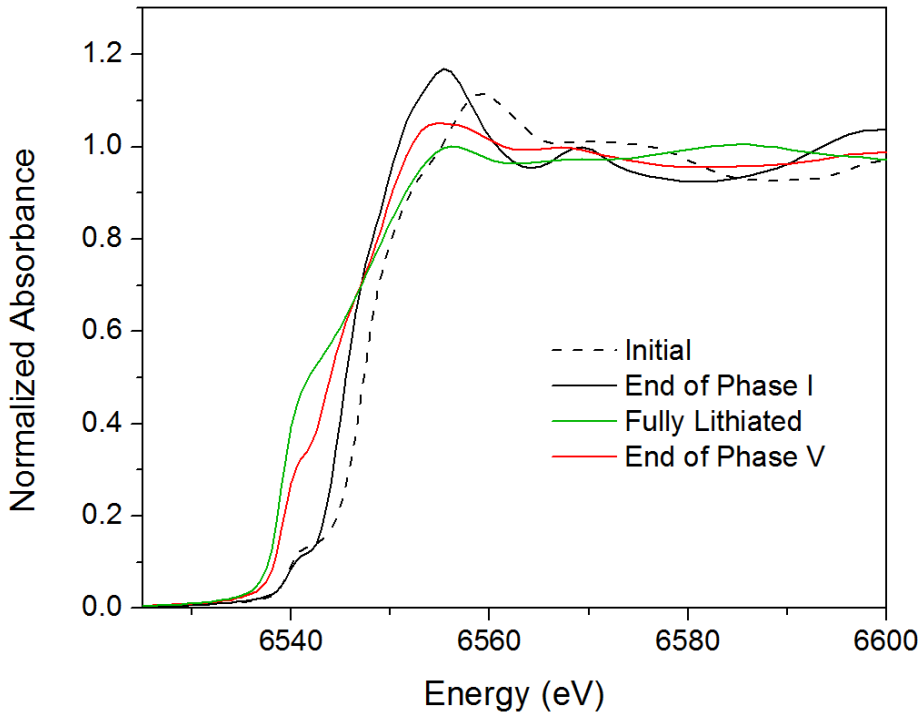

Figure 3-11. Selected XANES spectra at specified points during the first galvanostatic charge/discharge cycle.

sequence of reactions is strongly dependent on the diffusion of several different ions within the intermediate states, which can be suggested based on the observed phases: first lithium into Mn_3O_4 to form $LiMn_3O_4$, then diffusion of Li^+ and O^{2-} *out* of $LiMn_3O_4$ to form MnO, and finally O^{2-} diffusion out of MnO until the oxide is sufficiently reduced and disordered to nucleate Mn clusters. The dependence on diffusion raises the interesting possibility of using the material as an anode material at elevated temperatures, where the kinetics of the diffusion processes are accelerated,[39] although the key question of electrolyte stability will require close attention.[34]

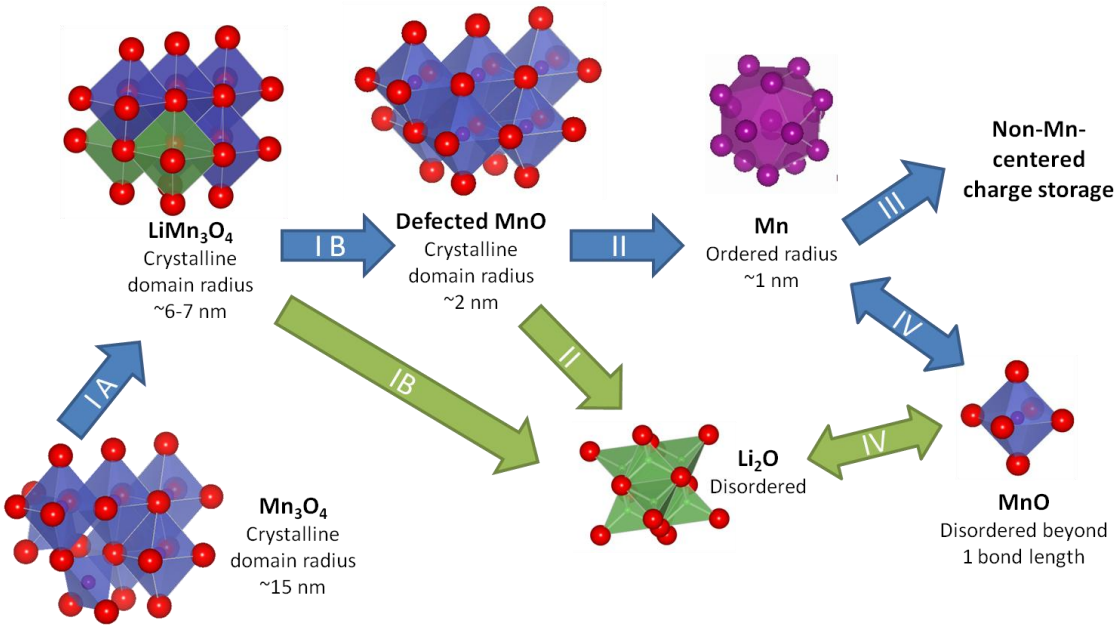

Figure 3-12. Proposed mechanism and observed Mn-based species.

These results verify the broad outlines of the proposed mechanism for Mn_3O_4 anodes[13] and, by providing additional resolution on the number and sequence of reactions, also emphasize that several key questions for these conversion anodes remain unaddressed. Although recent publications have been devoted to the

preparation manganese oxides with optimized synthesis method,[40] particle morphology,[9] and conductive additives,[22,40] less attention has been devoted to the more significant issue of understanding and minimizing solvent decomposition at the nanoparticles, a phenomenon that appears to occur on all the manganese oxide anodes. Furthermore, the apparently significant capacitive-like charge storage at low voltages (>150 mAh/g-Mn_3O_4 in phase III) warrants additional study as a means of storing charge, both to quantify its capacity and identify the faradaic processes.[41]

This study also demonstrates the advantages of in-operando characterization to resolve the sequence and electrochemical dependence of reactions. In-operando characterization is particularly valuable in the case of conversion reactions since the complexity of the overall transformation permits many possible intermediate states and side reactions. In this system, observing the temporal evolution of the electrode enables detection of relative fractions for reactants and intermediates – such as the conversion from MnO to Mn – and indirect detection of side reactions – such as the electrolyte reaction at the beginning of the lower voltage plateau.

5-5. Conclusions

The lithiation of Mn_3O_4 anodes can be probed using in-operando synchrotron XRD and XAS to obtain additional insights into the number and sequence of the conversion reaction. XRD resolves the electrochemically-induced variation of several intermediate phases during the first stages of lithiation, but is of limited value in probing the reaction of the weakly crystalline reduced oxides, while XAS can probe the variation between two weakly ordered phases in the final stages of lithiation. XAS demonstrates that a significant fraction of the first lithiation is associated with non-Mn-centered charge storage, and the results imply that a large fraction of capacity in

subsequent cycles is also non-Mn-centered. In-operando studies are clearly a valuable approach to verify that the observed charge storage is due to the desired electrochemical reactions.

REFERENCES

(1) Cabana, J.; Monconduit, L.; Larcher, D.; Palacín, M. R. *Advanced Materials* **2010**, *22*, E170–E192.

(2) Bruce, P. G.; Freunberger, S. A.; Hardwick, L. J.; Tarascon, J.-M. *Nature Materials* **2011**, *11*, 19–29.

(3) Thackeray, M. M.; David, W. I. F.; Bruce, P. G.; Goodenough, J. B. *Materials Research Bulletin* **1983**, *18*, 461–472.

(4) Thackeray, M. M.; Coetzer, J. *Materials Research Bulletin* **1981**, *16*, 591–597.

(5) Godshall, N. A.; Raistrick, I. D.; Huggins, R. A. *Materials Research Bulletin* **1980**, *15*, 561–570.

(6) Li, H.; Huang, X.; Chen, L. *Solid State Ionics* **1999**, *123*, 189–197.

(7) Poizot, P.; Laruelle, S.; Grugeon, S.; Dupont, L.; Tarascon, J.-M. *Nature* **2000**, *407*, 496–499.

(8) Wang, H.; Cui, L.-F.; Yang, Y.; Sanchez Casalongue, H.; Robinson, J. T.; Liang, Y.; Cui, Y.; Dai, H. *Journal of the American Chemical Society* **2010**, *132*, 13978–13980.

(9) Gao, J.; Lowe, M. A.; Abruña, H. D. *Chemistry of Materials* **2011**, *23*, 3223–3227.

(10) Kim, H.; Kim, S.-W.; Hong, J.; Park, Y.-U.; Kang, K. *Journal of Materials Research* **2011**, *26*, 2665–2671.

(11) Fan, Q.; Whittingham, M. S. *Electrochemical and Solid-State Letters* **2007**, *10*, A48.

(12) Pasero, D.; Reeves, N.; West, a *Journal of Power Sources* **2005**, *141*, 156–158.

(13) Fang, X.; Lu, X.; Guo, X.; Mao, Y.; Hu, Y.-S.; Wang, J.; Wang, Z.; Wu, F.; Liu, H.; Chen, L. *Electrochemistry Communications* **2010**, *12*, 1520–1523.

(14) Zhong, K.; Xia, X.; Zhang, B.; Li, H.; Wang, Z.; Chen, L. *Journal of Power Sources* **2010**, *195*, 3300–3308.

(15) Zhong, K.; Zhang, B.; Luo, S.; Wen, W.; Li, H.; Huang, X.; Chen, L. *Journal of Power Sources* **2011**, *196*, 6802–6808.

(16) Wu, M.-S.; Chiang, P.-C. J.; Lee, J.-T.; Lin, J.-C. *The Journal of Physical Chemistry B* **2005**, *109*, 23279–23284.

(17) Reimers, J. N.; Dahn, J. R. *Journal of the Electrochemical Society* **1992**, *139*, 2091–2097.

(18) Balasubramanian, M.; Sun, X.; Yang, X.; McBreen, J. *Journal of power sources* **2001**, *92*, 1–8.

(19) Braun, A.; Shrout, S.; Fowlks, A.; Osaisai, B.; Seifert, S.; Granlund, E.; Cairns, E. *Journal of Synchrotron Radiation* **2003**, *10*, 320–325.

(20) Nelson, J.; Misra, S.; Yang, Y.; Jackson, A.; Liu, Y.; Wang, H.; Dai, H.; Andrews, J. C.; Cui, Y.; Toney, M. F. *Journal of the American Chemical Society*.

(21) Morcrette, M.; Chabre, Y.; Vaughan, G.; Amatucci, G. G.; Leriche, J.-B.; Patoux, S.; Masquelier, C.; Tarascon, J.-M. *Electrochimica Acta* **2002**, *47*, 3137–3149.

(22) Wang, H.; Cui, L.-F.; Yang, Y.; Sanchez Casalongue, H.; Robinson, J. T.; Liang, Y.; Cui, Y.; Dai, H. *Journal of the American Chemical Society* **2010**, *132*, 13978–80.

(23) Hammersley, A. P.; Svensson, S. O.; Hanfland, M.; Fitch, A. N.; Häusermann, D. *High Pressure Res.* **1996**, *14*, 235–248.

(24) Ravel, B.; Newville, M. *J. Synchroton Radiat.* **2005**, *12*, 537–541.

(25) Lee, K. J.; Iguchi, A.; Iguchi, E. *Journal of Physics and Chemistry of Solids* **1993**, *54*, 975–981.

(26) Okamoto, H. *Journal of Phase Equilibria and Diffusion* **2007**, *28*, 307–308.

(27) Kofstad, P. *Journal of Physics and Chemistry of Solids* **1983**, *44*, 879–889.

(28) Chen, C.; Ding, N.; Wang, L.; Yu, Y.; Lieberwirth, I. *Journal of Power Sources* **2009**, *189*, 552–556.

(29) Eisenberger, P.; Brown, G. S. *Solid State Communications* **1979**, *29*, 481–484.

(30) Farges, F. *Physical Review B* **2005**, *71*.

(31) Catlow, C. R. A.; Mackrodt, W. C.; Norgett, M. J.; Stoneham, A. M. *Philosophical Magazine A* **1979**, *40*, 161–172.

(32) Gilbert, B.; Frazer, B. H.; Belz, A.; Conrad, P. G.; Nealson, K. H.; Haskel, D.; Lang, J. C.; Srajer, G.; De Stasio, G. *The Journal of Physical Chemistry A* **2003**, *107*, 2839–2847.

(33) Poizot, P.; Laruelle, S.; Grugeon, S.; Dupont, L.; Tarascon, J. M. *Ionics* **2000**, *6*, 321–330.

(34) Laruelle, S.; Grugeon, S.; Poizot, P.; Dollé, M.; Dupont, L.; Tarascon, J.-M. *Journal of The Electrochemical Society* **2002**, *149*, A627.

(35) Lee, J.-C.; Litt, M. H. *Macromolecules* **2000**, *33*, 1618–1627.

(36) Li, H.; Balaya, P.; Maier, J. *Journal of The Electrochemical Society* **2004**, *151*, A1878.

(37) Lyu, K. K.; Phan, T. L.; Yu, S. C.; Oh, S. K.; Dan, N. H. *IEEE Transactions on Magnetics* **2010**, *46*, 2028–2031.

(38) Freunberger, S. A.; Chen, Y.; Peng, Z.; Griffin, J. M.; Hardwick, L. J.; Barde, F.; Novak, P.; Bruce, P. G. *Journal of the American Chemical Society* **2011**.

(39) Mestre-Aizpurua, F.; Laruelle, S.; Grugeon, S.; Tarascon, J.-M.; Palacín, M. R. *Journal of Applied Electrochemistry* **2010**, *40*, 1365–1370.

(40) Liu, S. Y.; Xie, J.; Zheng, Y. X.; Cao, G. S.; Zhu, T. J.; Zhao, X. B. *Electrochimica Acta* **2012**.

(41) Guo, X.; Fang, X.; Mao, Y.; Wang, Z.; Wu, F.; Chen, L. *The Journal of Physical Chemistry C* **2011**, *115*, 3803–3808.

CHAPTER 4

UNDERSTANDING SULFUR IN BATTERIES: A CRITICAL SURVEY OF TECHNIQUES FOR IN-OPERANDO STUDY OF LITHIUM-SULFUR BATTERIES

4.1 Introduction

Electrochemical energy storage in sulfur chemistry has attracted attention for at least the last 50 years, dating from the high temperature sodium-sulfur battery project at Dow Chemical and Ford Motor companies[1] and continuing today in the commercialized grid-scale high temperature sodium-sulfur batteries of NGK Insulators. There are indeed many practical motivations for the use of sulfur for energy storage: sulfur is inexpensive, abundant, easily purified, and non-toxic in its elemental form. Since each sulfur atom can store up to 2 e^-, sulfur has an excellent gravimetric charge storage capacity, and when matched with an alkali or alkaline earth anode, the energy storage system can have outstanding theoretical energy density. Prototypes for many of these systems have been already reported, with lithium-sulfur currently receiving the most academic research interest due to its superlative energy density. (Table 4-1) In this chapter, the focus will be on low temperature lithium-sulfur cells with liquid electrolyte solutions; however, many of the challenges and approaches should extend to other sulfur-based energy storage systems.

Table 4-1. Comparison of composition and capacities for energy storage systems based on elemental sulfur cathodes, versus a common lithium ion chemistry

Anode	Electrolyte	Cathode	Theoretical Specific Capacity (Mass of Anode and Cathode, mAh/g)
Graphite	Liquid/Gel	$LiCoO_2$	100*
Lithium	Liquid	S_8	1168
Liquid Sodium[1]	Ceramic	S_8	687
Solid Sodium[2]	Liquid	S_8	687
Magnesium[3]	Liquid	S_8	952

*** Limited to 0.5 electron per unit cell to avoid structural degradation and reaction with electrolyte.**

The promise for each of these systems is defined by the chemical reactivity of elemental sulfur, while the practical limitations of the system are found in the diverse chemistry of the reaction intermediates and products. Sulfur radical anions and dianions are generally described as distorted linear chains, but can also exist as rings and branched chains.[4] Previous extended Huckel studies have suggested that the charge is more localized at the terminal sulfur atoms, especially for dianions.[5] Chemically, this means that sulfur species are both weakly electrophilic (at central atoms) and nucleophilic (at end atoms).[6] The maximum nucleophilicity occurs at intermediate chain lengths [6] and has practical implications on which solvents[7] and metals[8] can be used with reduced sulfur species. The variation of charge with atomic position in the chain likely explains the rapid disproportionation of a given solution-phase polysulfide chain into a range of adjacent chain lengths.[9] These chemical equilibria make preparation of well-defined polysulfide solutions (i.e. standards) virtually impossible to prepare, with the possible exception of specific stoichiometries (i.e. Li_2S_8).[10]

In aqueous solutions, reduced sulfur species range from weakly acidic (pKa2 of HS_8^-

is ~4.4[11]) to strongly basic (pKa2 of HS^- is extrapolated to ~18[12]). In aprotic solvents, the energetics of association between cations and sulfur dianions has not been fully investigated, but the widely varying solubilities of sulfur species have been observed by several researchers (from mM solubility of elemental sulfur in ethereal solvents to >10 M [S] as Li_2S_8 in dimethyl sulfoxide, tetrahydrofuran,[13,14] or tri(ethylenegylcol)dimethyl ether[15] to ~1 mM [S] as Li_2S in liquid ammonia[16]). This variation in solubility drives redistribution of sulfur species within electrochemical cells, with significant practical implications for the design of lithium-sulfur devices. (Chapter 7)

In addition to the practical considerations for cell design and materials, there are imposing challenges to actual understanding of the key reactions under battery conditions (i.e. highly concentrated solutions of sulfur species and ethereal solvents). Reduced sulfur species are highly air- and moisture-sensitive, and react via an unknown number of species and reactions to the completely reduced Li_2S. While several excellent spectroelectrochemical studies have investigated the early stages of sulfur reduction,[10,17–19]these studies have not investigated the more technologically-relevant final stages of sulfur reduction that are responsible for the majority of charge stored. The studies were also conducted with dilute concentrations of sulfur and electrolytes, such as N,N-dimethylformamide, that are impractical for use with lithium. It is thus an open question whether their results can be applied to understand the mechanism of sulfur reduction in highly concentrated solutions, where higher-order reactions become more significant, and in solvents of low polarity, which disfavor formation of highly charged species. Additional complexity is introduced by the close proximity of the lithium anode, which can pass charge to and accumulate atoms from sulfur species in solution. (Figure 4-1) While analytical studies are often done at low concentrations and then extrapolated to explain the response of a system,

in the case of the lithium-sulfur battery system this approximation may not be appropriate.

However difficult they may be, analytical studies of sulfur reduction are important to resolve both mechanistic and practical questions about the sulfur system. A better understanding of the mechanism is an important foundation for future chemical and electrocatalytic approaches to improving the reaction rate, and allows objective comparison of novel materials, electrode architectures, and cell designs. These studies would only be further complicated by taking ex-situ analysis, since removal of the

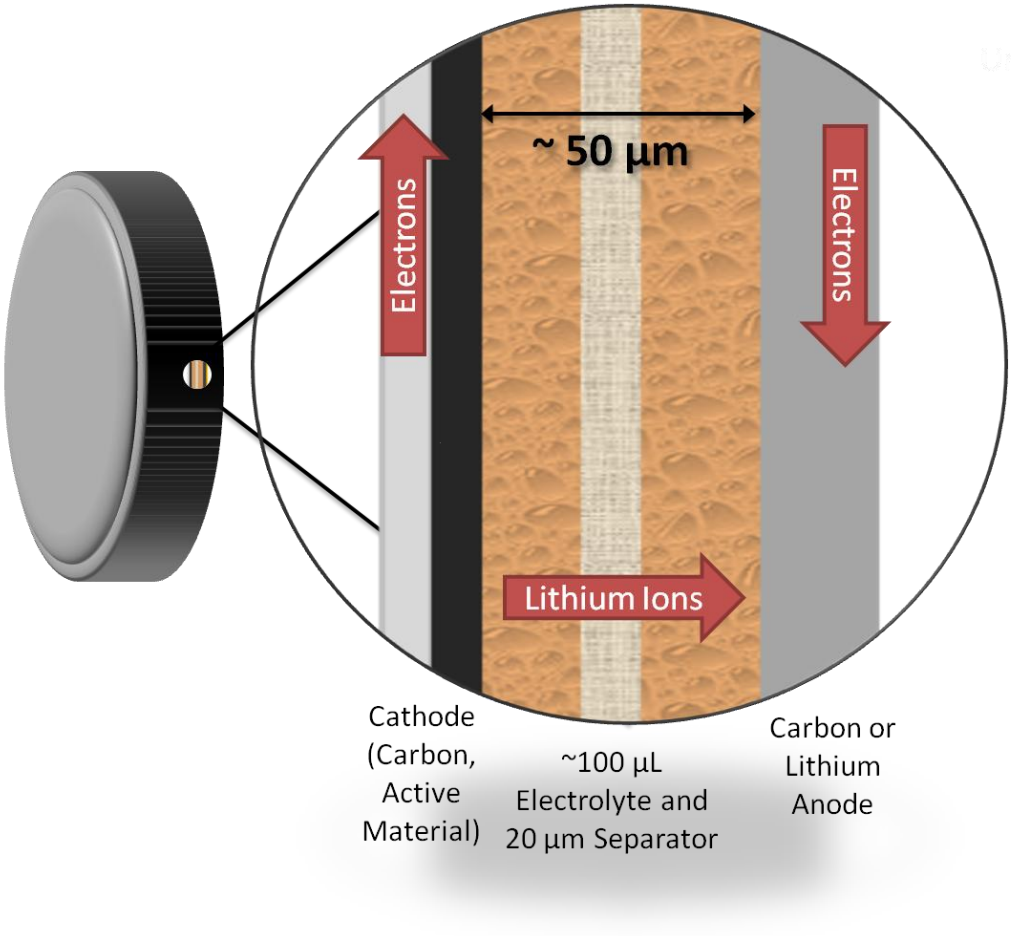

Figure 4-1. Typical configuration of electrodes in prototype lithium-sulfur batteries. Soluble polysulfides easily diffuse the short distances between the sulfur-containing cathode and lithium anode, and lithium interactions with sulfur species cannot be neglected.

cathode from the battery solvent and potential control introduces the variable of time, possibly alters the chemical equilibria, and likely results in a non-representative ensemble of sulfur species. This is particularly true given the range of solubilities for reduced sulfur species. Practically, additional analytical studies of sulfur are important to diagnose why current prototype cell performance falls short of theoretical capacities, and to identify reactivities between reduced sulfur species and cell components.

As demonstrated in Chapter 3, application of analytical techniques to operating battery cathodes (*in-operando*) allows direct correlation between electrochemical and analytical datasets, and can provide sufficient data to extract chemically-relevant data about reaction processes. *In-operando* battery studies are not a new concept, but prior studies have generally studied solid-state materials, including intercalation[20–22] and conversion reactions,[23] or changes to the electrolyte solution due to reactivity with the electroactive material.[24] In contrast, the wide solubility range for sulfur species means that reactions between lithium and sulfur may occur both in solution and in the solid state. Thus, it is important to probe spatial and temporal distributions of sulfur species, all while minimizing changes from typical lithium-sulfur cell conditions.

This chapter surveys the applicability of several standard analytical techniques to detect and resolve reduced sulfur species, as a means of understanding the key chemical reactions and intermediates during the operation of a lithium-sulfur battery. The techniques surveyed here include electrochemical analysis, x-ray diffraction, x-ray and ultraviolet/visible (UV-Vis) absorption spectroscopies, and confocal Raman spectroscopy, several of which are investigated in more detail in later chapters. Many analytical techniques can be applied to the resolution of sulfur species, and the techniques identified here are not an exhaustive list. Instead, it is hoped that consideration of the challenges and possibilities for these common techniques will

facilitate future technique development and implementation.

The following section reviews the typical results from each of the techniques of interest, presenting sample data when available and otherwise referencing examples from the literature. Special consideration is given to the following criteria:

- sensitivity to sulfur species
- selectivity of the technique for specific sulfur species
- number of species resolved
- spatial resolution, both in plane and normal to the sulfur cathode

4.2 Electrochemical Analysis

Electrochemistry directly probes heterogeneous charge transfer kinetics and thermodynamics, and thus it would seem to be an ideal technique to probe the electrochemical reduction mechanism within the lithium-sulfur battery. Indeed, the battery response itself is an electrochemical dataset. Prototype cells are routinely cycled under galvanostatic or potentiostatic conditions, providing controlled current or controlled potential electrolysis datasets, respectively, for which interpretations have been proposed based on coulometry[25,26] or mathematical models.[27] Unfortunately, as demonstrated in Chapter 7, the unknown distribution and quantity of electrolyte in the cells, the high solubility of specific sulfur species, and presence of lithium metal in close proximity to the sulfur cathode all complicate the analysis of whole cell data.

An alternate electroanalytical approach involves insertion of a microelectrode probe or array into the battery. This approach can provide spatial resolution limited only by electrode design and precision in placement and is sensitive to sub-millimolar sulfur concentrations. Actual electrode insertion is challenging using a coin cell due to the crimped seal, but has already been demonstrated for a swagelock cell, albeit with significantly (~5X) more electrolyte than typically used for coin cells.[28] Dominko et

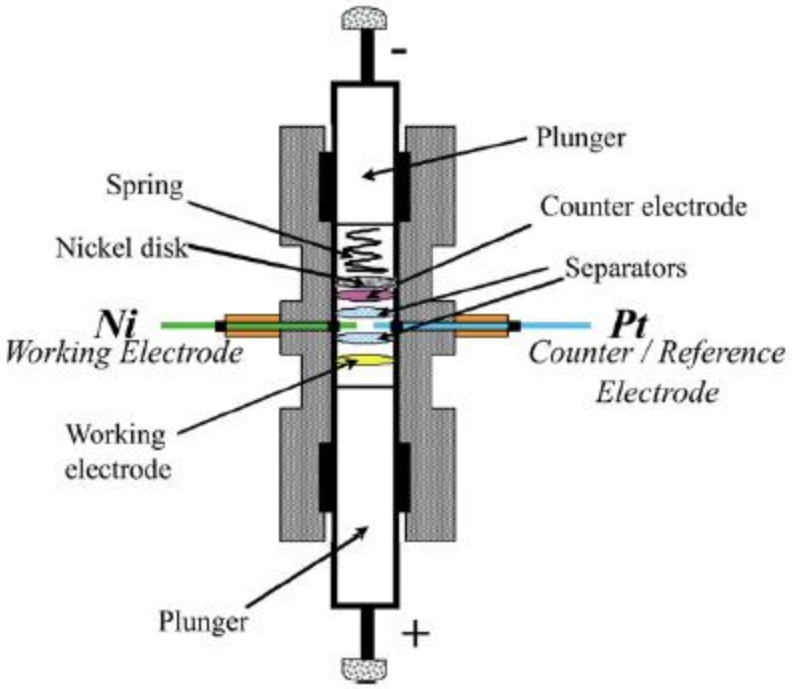

Figure 4-23. Swagelock battery cell modified for in-operando electrochemical detection of soluble polysulfides. Copied from reference [28] with permission from Elsevier.

al. showed that a Ni sensing electrode could be used to conduct cyclic voltammetric experiments during the cycling of a lithium-sulfur battery, and calibrated the charge passed during a voltage cycle with the approximate concentration of sulfur species in solution. However, the actual shape of their cyclic voltammetric results changed with sulfur concentration, identity of carbon-sulfur composite, and average sulfur oxidation state. While there is clearly additional chemical information contained in their results, they were not able to selectively identify sulfur species in solution.

The greatest challenge to electroanalytical methods is the variable sensitivity for sulfur species. Electroanalytical studies at dilute concentrations in N,N-dimethylformamide (DMF) generally have observed two or three reduction peaks, with the first from reduction of S_8 and the latter two from reduction of S_3^- and S_4^- radical anions, S_3^- being the dominant species;[10] even though these three reduction processes can be resolved in cyclic voltammetry, there are clearly additional intermediates and products

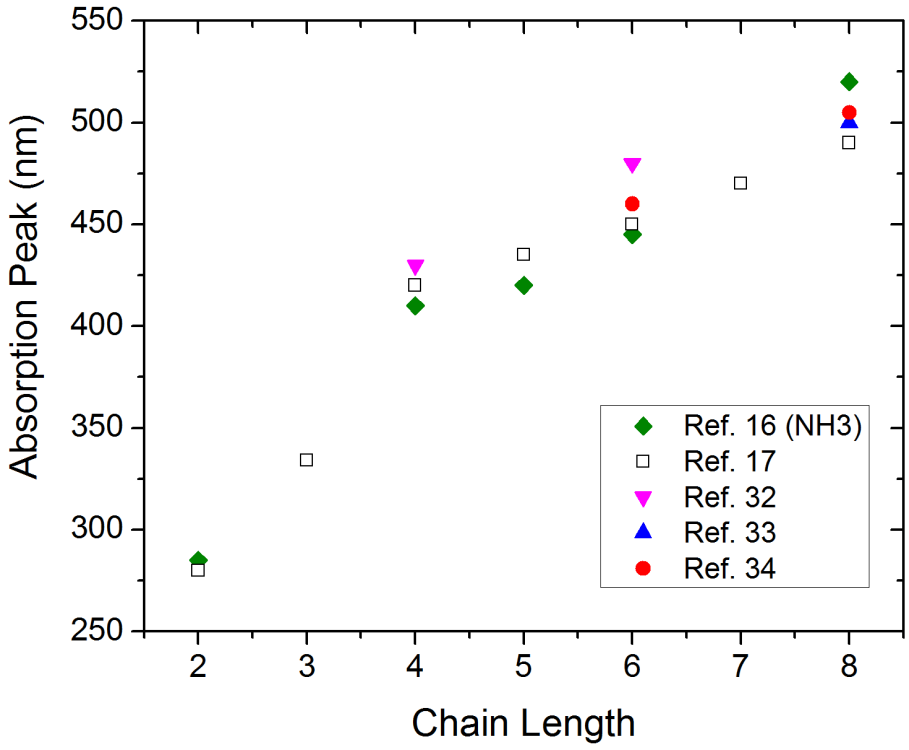

Figure 4-3. Literature reports of lowest-energy UV-Vis absorption peak for dianionic polysulfides as a function of chain length. All positions are reported in DMF solvent unless otherwise indicated.

in the reduction of S_8 that are not active for heterogeneous charge transfer and thus are not detected electrochemically. This includes both dianions, which are not reduced in the typical electrochemical window of 1.5-3.0 V vs. Li/Li^+, as well as insoluble lithium polysulfides which cannot diffuse to the probe electrode. Thus, while electrochemistry is a sensitive technique to probe the concentration of a few specific sulfur species, it cannot provide detailed concentration data for all the sulfur species in the battery.

4.3 UV-Vis Absorption Spectroscopy

Many of the early electroanalytical studies of sulfur coupled electrochemical techniques with in-situ UV-Vis spectroscopy,[16–18,29–34] and the chemical assignments of electrochemical features discussed above are primarily based on those

spectroscopic results. This historical association means that UV-Vis is the most mature of the spectroscopic characterization techniques, with several sets of proposed spectral assignments for reduced sulfur species in different solvents.

Since UV-Vis probes electronic transitions within molecules, the systematic variation of chemical properties among reduced sulfur species would suggest a systematic increase in transition energy from long to short polysulfide chains. This is generally consistent with assignments proposed in the literature for the lowest energy transition for polysulfide dianions.[32–34] (Figure 4-3) It should be noted that the scatter in the assignments is comparable to the difference in wavelengths, making absolute wavelength assignments tenuous. The most complete set of assignments were made based on time-resolved UV-Vis spectroelectrochemical experiments using the explicit assumption that peak energies follow the expected trend. However, in some cases the data presented by the authors do not unambiguously support the presence of reported peaks (e.g. Li_2S_2), and the peak assignments appear to be based on visual observations rather than a rigorous curve fitting.[17] This is worrisome considering that the authors propose to resolve five relatively broad (~50 nm FWHM) peaks within a small (< 100 nm) spectral window.

The most definitive spectral assignment for a reduced sulfur species is that the peak near 620 nm corresponds to the radical anion S_3^-. The presence of a delocalized unpaired electron in the radical anion results in a much lower energy transition than for any of the dianionic species, and has allowed its assignment to be confirmed by electron spin resonance (ESR) in addition to colorimetric titration and temperature dependent spectroscopy.[34] One report has proposed that S_4^- has a peak near 700 nm, but without convincing spectral data.[17]

Given the existence of spectral assignments for many polysulfides, it would be attractive to couple UV-Vis spectroscopy into a lithium sulfur battery to probe the

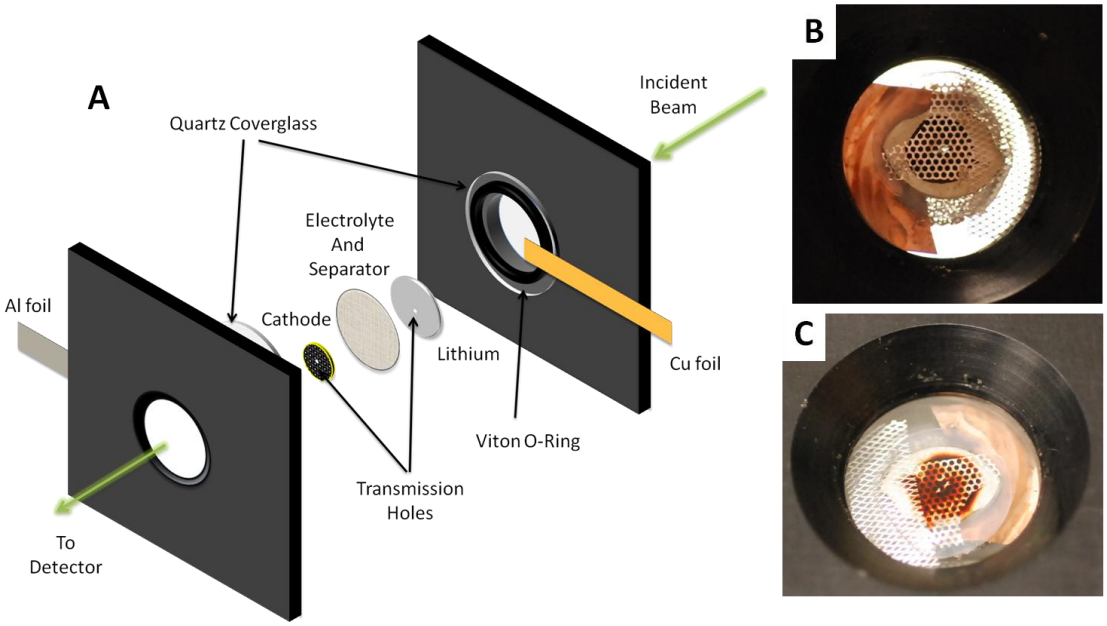

Figure 4-4. Setup for in-operando UV-Vis spectroscopy of soluble sulfur species. (A) Schematic of cell assembly. (B) Optical image of assembled cell before reaction, showing transparent region in center of electrodes. (C) Image of assembled cell during galvanostatic discharge, at 2.3 V vs. Li/Li+. Red color is due to concentrated long-chain polysulfides.

soluble species formed during cycling. There is one report of this having been attempted for elevated temperature lithium-sulfur cells with a polyethylene oxide electrolyte.[35] Marmorstein used several different cell designs before settling on a swagelock cell with a large (~3 mm) hole drilled through all of the opaque components (cathode, anode, and cell components) for light transmission. Using this cell, she could observe an increased concentration of polysulfides in the electrolyte during the course of cycling, with absorbance peaks at 330 and 440 nm. However, the identity of these peaks remain unclear – Marmorstein assigned them to Li_2S_2 and Li_2S_4, respectively, based on similarities to the spectra from the corresponding stoichiometric mixes of Li_2S and S_8, but due to differing solubilities and stabilities of chemical species, these stoichiometric mixtures are not guaranteed to produce the desired product. For example, a nominal concentration of Li_2S_2 can also result in Li_2S_4 + $2Li_2S$ or Li_2S_6 + $3Li_2S$.

While the specific identities of sulfur species may be uncertain, Marmorstein's technique is able to provide an in-operando probe of soluble species. Preliminary experiments demonstrate that this approach should also be feasible for low temperature, liquid electrolyte cells. Figure 4-4 shows a cell design that can pass visible light through both electrodes, with the minimal hole size determined by the specifics of the UV-Vis spectrometer. Unfortunately, the spectrometer used in the preliminary experiments required a large transmission hole (> 1 mm). Under these conditions, it is probable that there is a heterogeneous distribution of sulfur species in the transmission hole, making it difficult to make statements about the relevant species within or at the cathode. Finally, the high local concentration of sulfur species in solution can absorb too much of the incident light, precluding data acquisition at least during the initial stages of discharge (Figure 4-4C).

An attractive approach that has not been reported in the literature is the use of diffuse reflectance (DR) UV-Vis spectroscopy to probe the sulfur species in the cathode. Unlike transmission UV-Vis spectroscopy, DR UV-Vis can obtain signal from opaque samples, including insoluble species on a sulfur cathode or highly concentrated polysulfide solutions. This could reasonably extend UV-Vis beyond the interrogation of species in solution to probe the dominant species at the cathode throughout the discharge. It is anticipated that DR UV-Vis could use a cell similar to that shown in Figure 4-4A, but without a transmission hole.

4.4 Confocal Raman Spectroscopy

Vibrational spectroscopy probes structural vibrations in both crystalline and amorphous materials, and both forms of elemental sulfur have been characterized using infrared and Raman spectroscopy. [36]

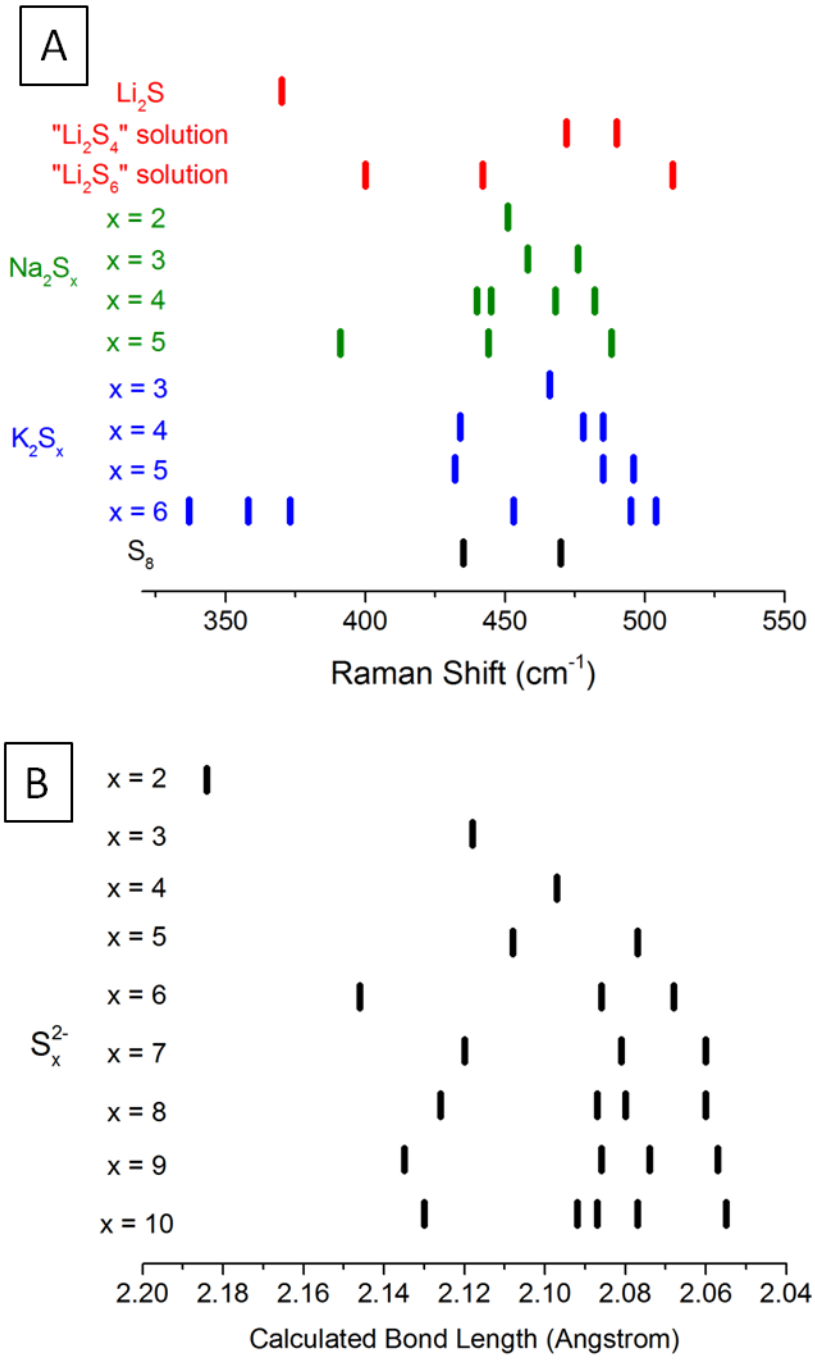

Figure 4-5. (A) Summary of polysulfide Raman peak positions in the sulfur bond stretching region. Potassium[37] and sodium[38] crystalline standards; lithium polysulfide solutions[16] with nominal concentrations as indicated; sulfur and lithium sulfide data acquired as part of present work. polysulfides from literature (B) Summary of calculated bond lengths for polysulfide dianions. Polysulfide dianions calculated as part of work presented in Chapter 5.

The air-sensitivity of polysulfides complicates the use of infrared to characterize the reduced sulfur species, particularly since the observed fundamental modes are at low wavenumbers/incident photon energy. Raman spectroscopy has been more successful since the signal is encoded in energy shifts from a higher energy incident photon. While there are fewer literature reports for polysulfide Raman than for UV-Vis, there are reports of Raman for well-defined crystalline sodium[37] and potassium[38] polysulfides. The vibrational modes should have some dependence on cation identity, but since this variation should be much larger for lattice and intermolecular modes (< 150 cm^{-1}) than for intramolecular sulfur bond bending (150-400 cm^{-1}) and stretching modes (> 300 cm^{-1}), the peak positions of the other alkali polysulfides should be a good indication of where the Raman peaks for lithium polysulfides will be found. Comparison of the known peak positions in the stretching region (Figure 4-5A) suggests that the Raman peaks for lithium polysulfides should also be found between 370-510 cm^{-1}, with peak positions converging towards 450 cm^{-1} as the chain length (and number of distinct S-S bond distances) decreases. In general, the Raman peak position of a sulfur stretching mode is inversely related to the bond length: the longer the bond, the lower energy the Raman shift.[39] As expected, the trend in bond lengths between the various different polysulfides (Figure 4-5B) match the trend in reported peak positions. The spectral range is ~10 times the typical peak FWHM. However, the peaks are not uniformly distributed over the range, resulting in significant peak overlap for polysulfides of similar chain lengths. In contrast, the Raman signals for the radical species S_3^- and S_2^- are shifted to higher energies (535[40] and 580[41] cm^{-1}, respectively), and are more completely resolved.

One of the key challenges for Raman data acquisition is the low quantum efficiency (~0.001%) of Raman scattering, which necessitates the use of an intense

monochromatic (i.e. laser) source. It is also advantageous to couple the Raman spectrometer to a confocal microscope. This enables focusing the incident light into a well-defined volume element, and increases both collection efficiency and spatial resolution. Under these conditions, experimental caution is necessary to avoid artifacts from localized heating or photochemistry. In practice, a high-resolution Raman spectrum for concentrated (1 M) sulfur species required significant accumulation time (>300 s). It is possible to obtain several orders of magnitude more sensitivity for a specific species by using a laser wavelength that is within an electronic transition for the molecule (resonance Raman). However, it is impractical to arbitrarily tune the laser wavelength to select for the sulfur species of most interest. The most general approach for improving sensitivity would be to use an ultraviolet laser (e.g. 288 nm). Polysulfides absorb strongly in the UV and the Raman signal increases strongly with incident photon energy (roughly quartic with frequency, although the higher energy photons may also generate too much background fluorescence.

Confocal Raman spectroscopy can interrogate battery electrodes behind any optically transparent window, such as the cell shown in Figure 4-4A, as long as the focal length of the microscope objective is significantly longer than the window thickness. While in-operando Raman spectroscopy has been reported for a number of inorganic lithium intercalation chemistries,[42,43] to the best of my knowledge this technique has not previously been applied to the lithium-sulfur battery system. There has been one previous in-situ Raman investigation of sulfur reduction, but the authors attempted to collect spectra from dilute concentrations of polysulfides and were only able to detect the S_3^- radical anion.[40]

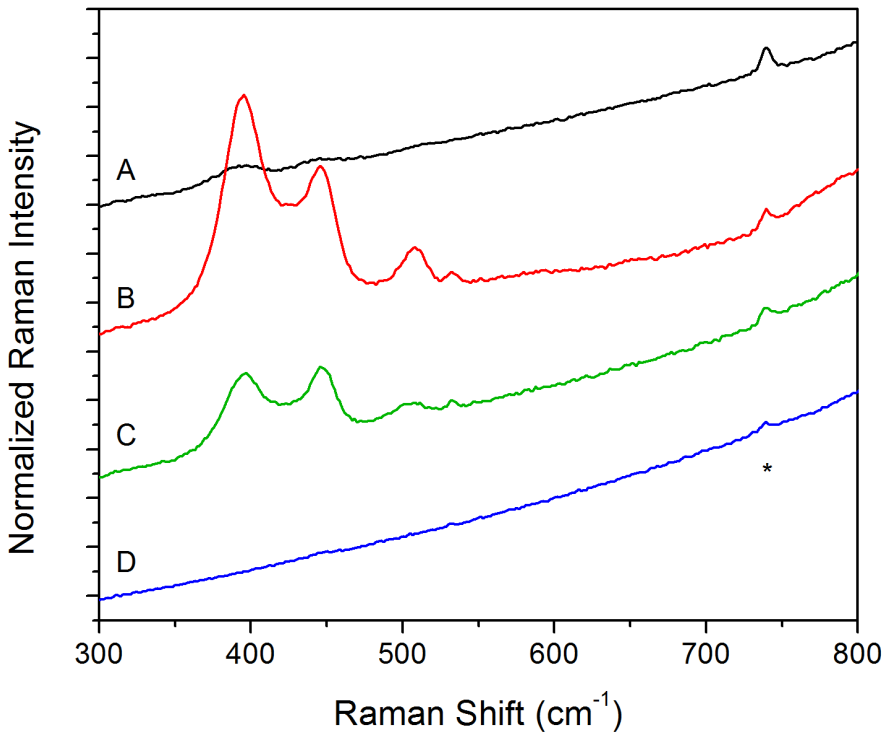

Figure 4-6. In-Situ Raman data acquired during voltage holds of a lithium-sulfur cell. (A) Initial spectra (B) End of 60 minute hold at 2.2 V (C) First 20 minutes at 1.95 V (D) End of 2 hour hold at 1.95 V. Incident wavelength 488 nm with ~5 W incident power. 20 minute acquisition for each spectra. Asterisk indicates peak from $TFSI^-$ anion in solvent.

Sample Raman results using the battery cell shown in Figure 4-4A are summarized in Figure 4-6 to show the type of data accessible from this technique. For these spectra, the microscope was focused on the cathode surface, but some signal from the $TFSI^-$ anion in solution is also seen and can act as an internal standard. When the battery voltage is held just below the first plateau (Figure 4-6B, 2.2 V), distinct peaks appear at 394, 446, and 509 cm^{-1}, consistent with a previous report for Li_2S_5 or Li_2S_6 solutions in liquid NH_3,[16] along with a weak peak at 532 cm^{-1} from S_3^-. There may also be signal from at least one additional peak between the peaks at 394 and 446 cm^{-1}. When the voltage is stepped to below the second plateau (Figure 4-6C, 1.95 V), each peak shifts slightly (1-5 cm^{-1}) but mainly changes in relative intensity. This is

consistent with an increased fraction of for shorter polysulfides (n < 5-6, Figure 4-4A), which do not have long S-S bonds and thus do not contribute to the peak at 394 cm^{-1}. Unfortunately, the combination of minor changes in peak position, an unknown number of superimposed peaks, and a non-negligible noise level even after 20 minutes of accumulation make it improbable that the correct number of polysulfides can be uniquely resolved from the data.

After a short time at 1.95 V the polysulfide Raman signal was overwhelmed by a large increase in luminescence. Surprisingly, the luminescence was even more pronounced with a longer wavelength (785 nm) incident laser, even though longer wavelengths generally have insufficient energy to excite fluorophores. This phenomena may ultimately be useful as an alternate technique for characterizing reduced sulfur species, such as by use of a confocal fluorescence microscope, but has deleterious effects on resolution of the Raman from reduced sulfur species.

A n important advantage of confocal Raman is the ability to collect spatially resolved chemical and morphological observations. This is particularly valuable for the lithium-sulfur system, since the wide variation in solubilities for sulfur species can create chemical heterogeneity within the electrochemical cell. For example, as seen in Figure 4-7A, at the end of the first discharge there are distinct color variations in the electrolyte solution surrounding the sulfur cathode due to a distribution of polysulfides in solution. Immediately around the cathode the solution is clear, indicating a low concentration of polysulfides, while further away from the electrode the solution is green and then red as the average polysulfide length increases. Raman can probe each solution and demonstrate shifts in peak position and relative intensity similar to those observed between spectra B and C of Figure 4-6.

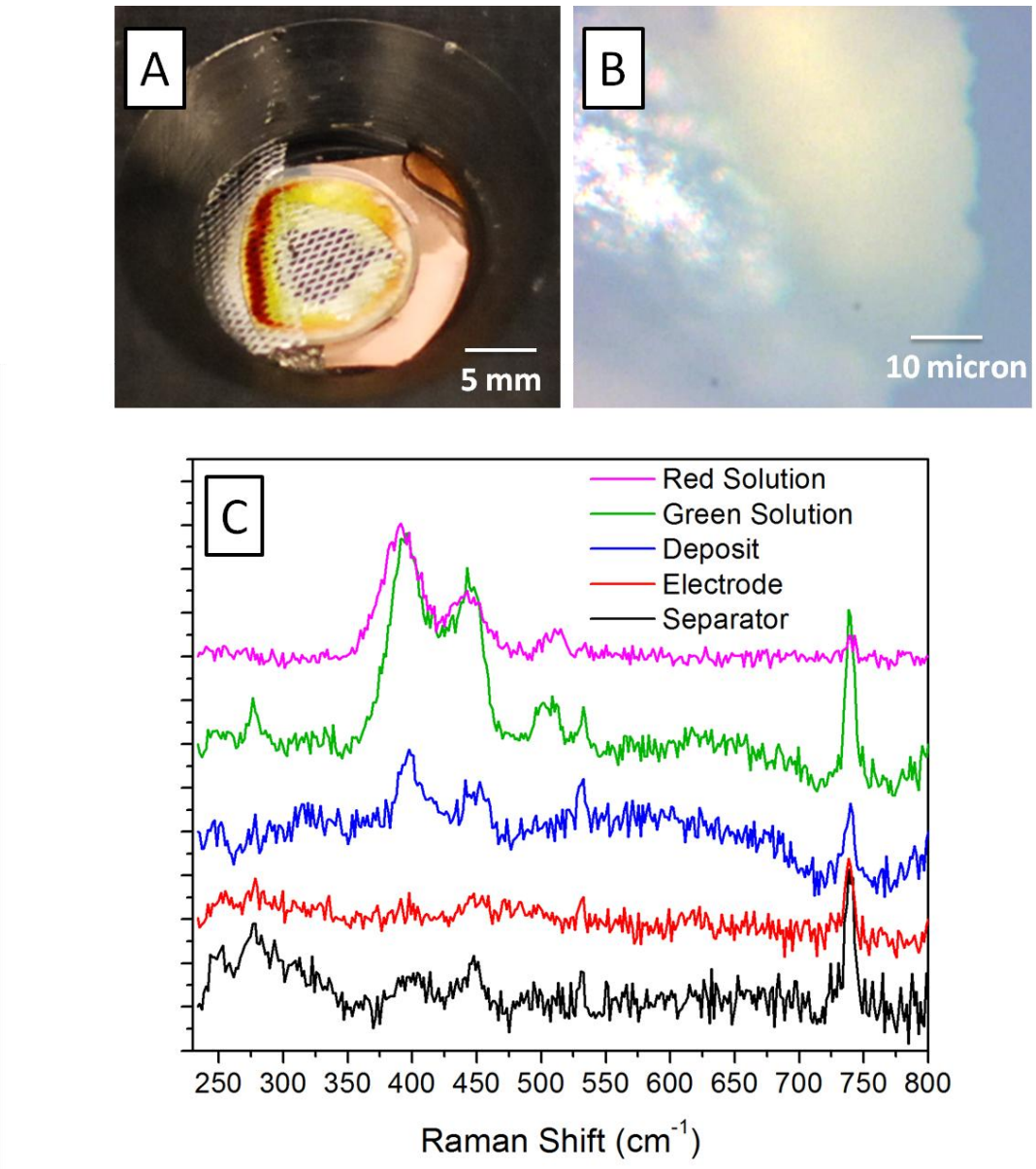

Figure 4-24. Application of confocal Raman to chemical heterogeneity in a lithium-sulfur cell discharged to 1.5 V at a rate of 100 mA/g-sulfur. (A) Image of cell through the cathode window. (B) Micrograph of polysulfide deposit (bright mass to image left) between the electrodes. Cathode is visible as dark shape to image right. (C) Raman spectra at areas of interest within the cell. Spectra collected with ~5 mW incident power and 50X objective for 600 s acquisition times.

However, in addition to the millimeter-scale inhomogeneities of electrolyte solutions, Raman can also probe micron-scale heterogeneity caused by differing polysulfide solubilities. Figure 4-7 B is a micrograph showing reflective deposits that appear near

the cathode after discharge. In all cases (>5 distinct spots), the deposit appeared to be supported on the separator at a focal plane below the cathode, that is, between the cathode and the anode. By itself, it is a powerful capability to monitor the appearance and position of deposits during cell operation. However, in the case of confocal Raman, these deposits can also be interrogated and compared to the surrounding environment. Figure 4-7C compares the spectrum of the deposit with spectra from electrode and the separator, and it is clear that the deposit represents a different ensemble of sulfur species. The absence of a peak near 505 cm^{-1} suggests that the deposit is composed of lower polysulfides (probably $n < 4$, by comparison with Figure 4-5), while the relatively high intensity peak at 532 cm^{-1} suggests that the precipitated sulfur species are in equilibrium with solution-phase S_3^-. One possible equilibrium could be:

$$2\ Li_2S_4 \rightarrow 2\ S_3^- + 2\ Li^+ + Li_2S_2$$

This reaction is also proposed in Chapter 7 based on electrochemical results.

4.5 X-Ray Diffraction

X-ray diffraction (XRD) provides structural information about ordered phases in a sample, and is a routine technique for materials characterization, both ex-situ and in-situ.[21,44] XRD is an excellent technique for chemical resolution of multiphase crystalline mixtures. Diffraction peak widths are typically less than 1% of the diffraction spectrum, and peak positions and intensities can be predicted from first principles. Unfortunately, while elemental sulfur has more crystalline allotropes than any other element,[45] lithium sulfide is the only confirmed crystalline intermediate phase in the lithium-sulfur phase diagram.[46,47] This is in contrast with other alkali metal-sulfur systems, all of which have at least three crystalline intermediates.[48,49] Thus, XRD for the lithium sulfur system can only indirectly probe the complex mechanism of conversion from sulfur to lithium sulfide.

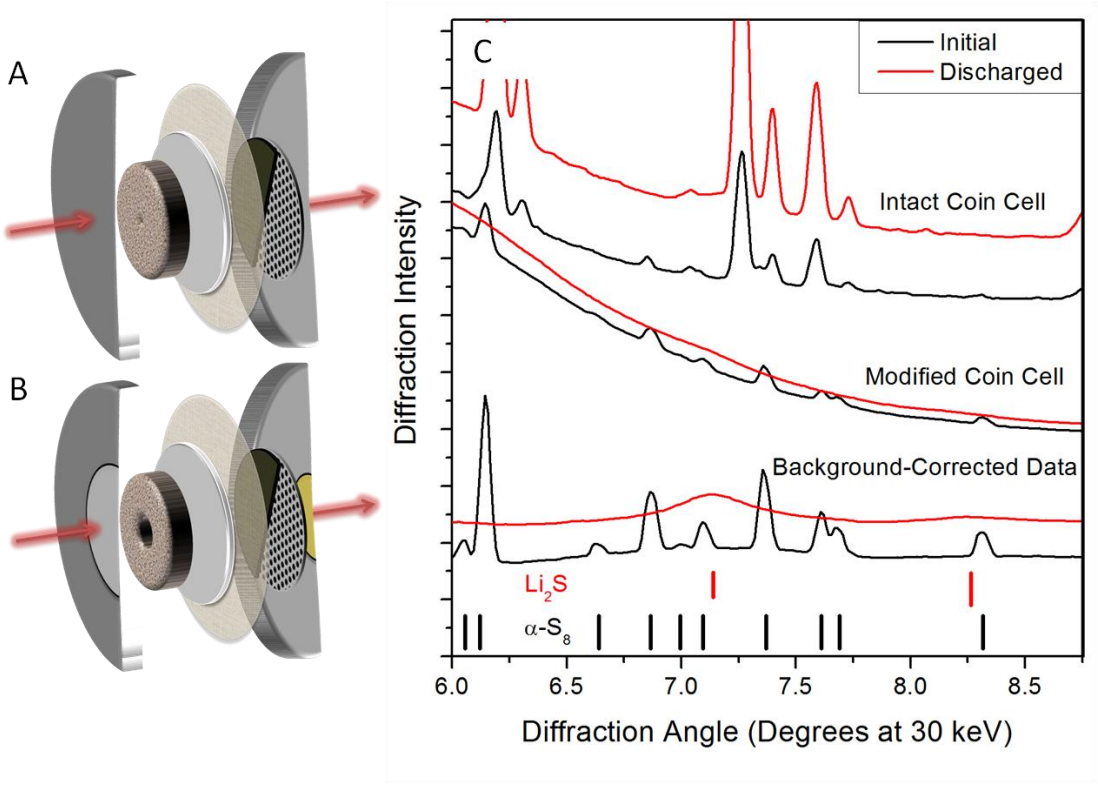

Figure 4-8. Coin-cell based in-operando cells for XRD. (A) Schematic of intact coin cell components (B) Schematic of modified coin cell components (C) Raw XRD spectra for initial and discharged sulfur cathodes within each type of coin cell, compared with background-subtracted data from a modified coin cell and the predicted diffraction positions for Li_2S and elemental sulfur.

In-operando XRD cells can be prepared with both transmission and reflection geometries,[44] but the transmission geometry is preferable. Reflection cells often use potentially toxic beryllium windows, and as the incident energy increases, diffraction peaks shift to lower angles that can be difficult to probe in a reflection geometry. A broad range of cell designs have been proposed in the literature.[44,50,51] By working at sufficiently high energy, it is even possible to collect diffraction sulfur cathodes within unmodified coin cells. However, significant improvements to signal to noise can be made by modifying standard coin cells to include aluminized kapton windows on both cathode and anode casings. (Figure 4-8) This design retains the cell geometry used in electrochemical testing of lithium-sulfur batteries and is inexpensive enough that replicate cells can easily be prepared for each experiment. Unfortunately, the use of

coin cells with polymer windows limits the diffraction study to a specific region of the cathode. Although incident x-ray beams can be made small enough to provide good (< 25 micron diameter) spatial resolution, full mapping of diffraction from a sulfur cathode necessitates the use of intact coin cells with a corresponding increase in interfering diffraction peaks.

Considering the number of total reports of in-operando XRD for batteries, there are surprisingly few reports of in-operando XRD for lithium-sulfur cells. Hassoun et al. used a lab diffractometer to probe a lithium sulfide cathode in a pouch cell, and observed lithium sulfide peaks disappear during galvanostatic oxidation.[52] They did not observe elemental sulfur reappear, and only showed diffraction for half a cycle. A very recent report from the Stanford Synchrotron Light Source (SSRL) used synchrotron XRD to characterize several different pouch cells. The authors saw elemental sulfur disappear during the initial stages of cell discharge and reappear after recharge, but did not detect crystalline lithium sulfide even in the fully discharged electrode. Interestingly, an ex-situ XRD on a cathode did show crystalline Li_2S. The authors proposed that the crystallization was induced by taking the electrode out of the electrochemical environment, but considering the cell design used and the unusual electrochemical results, it is also possible that the x-rays probed a region with poor internal contact and obtained non-representative results.

Use of the coin cell configuration shows significantly improved electrochemistry and representative XRD spectra, with features from elemental sulfur and lithium sulfide in the respective charged and discharged states. (Figure 4-8C) Furthermore, when polymer windows are used, a background signal can be identified that represents most of the scattering from the non-electroactive cell components. Subtraction of this background from the dataset results in clear diffraction signals for sulfur species. As shown in Chapter 6, additional analysis of these results can extract structural or

mechanistic information.

The great limitation of XRD for lithium-sulfur batteries is that the technique only probes the crystalline end products of the reaction, and there is no constraint that either sulfur or lithium sulfide has to be crystalline. As discussed in Chapter 3, the sensitivity to crystalline species means that XRD can be misleading unless crystalline and amorphous phases of a product respond concomitantly.

4.6 X-Ray Absorption Spectroscopy

X-rays can provide chemical information about specific elements through the application of x-ray absorption spectroscopy. This technique varies the incident photon energy close to a characteristic energy for emission of electrons from a specific atomic orbital, and measures the energy-dependent absorption coefficient associated with that transition. The resulting signal can be related to the local atomic structure and chemical state. The study of the response close to the characteristic energy (the edge) is called x-ray absorption near edge spectroscopy (XANES). In this energy region, the modulations can be large and are dominated by multiple scattering events between the photoelectron and the potential wells from neighboring atoms. The complex XANES signal can act as a fingerprint for specific chemical species and environments. While these interactions are difficult to solve analytically, there are codes that predict XANES signals using density functional theory[53,54] or using numerical approaches (FEFF, FDMNES). Unlike diffraction, which is only sensitive to crystalline phases, XANES provides mass-averaged information about all of the distinct chemical environments for the element of interest.

Sulfur K edge XANES is commonly used to characterize sulfur interactions within complex molecules,[55] sulfides,[56,57] and glasses,[58] or to speciate oxidized sulfur compounds in carbon.[59,60] The technique has also been applied to lithium-based and sulfur-containing battery systems, both ex-situ[61] and in-situ,[62] but surprisingly there

are no reports of its application to lithium sulfur batteries. In fact, prior to this work there were no reports of XANES for reduced alkali polysulfides and only one report of Li_2S XANES.[63]

The dearth of prior work is probably due to a combination of practical and spectroscopic concerns. Practically, studies of sulfur are made non-trivial by the low energy of the sulfur K edge (2472 eV). At this energy, photons are attenuated strongly, even with comparatively thin (< 100 micron) polymer windows, which complicates design of in-situ cells that provide reasonable signal and still prevent atmospheric contamination. In the results shown here and in Chapter 6, the cell design shown in 4-8B was successfully used with 8 micron-thick aluminized kapton windows, taking care to minimize exposure to non-inert atmospheres. XANES was observed by detecting x-ray fluorescence produced by the relaxation of outer shell electrons to the empty K shell. This process is proportional to the actual x-ray absorption event, and allows measurement of XANES without attenuation from the remaining cell components. Unfortunately, the proportionality constant is small for sulfur.[64]

In principle the technique is capable of high spatial resolution, given the right incident beam size and detector geometry, but the present work used a beam nearly the same size as the cell window for faster data acquisition. For the study of sulfur, mapping of sulfur chemical distribution in the plane of the cathode will always be limited by the size of the thin polymer window. However, the strong attenuation of x-rays may be used to resolve sulfur species within different regions of the cell. For example, if electrolyte solution is trapped between the window and the cathode, the signal is dominated by sulfur species in solution instead of from sulfur species in the cathode. Similarly, if the cell is assembled with the lithium anode adjacent to the window, the signal is dominated by species at the anode.

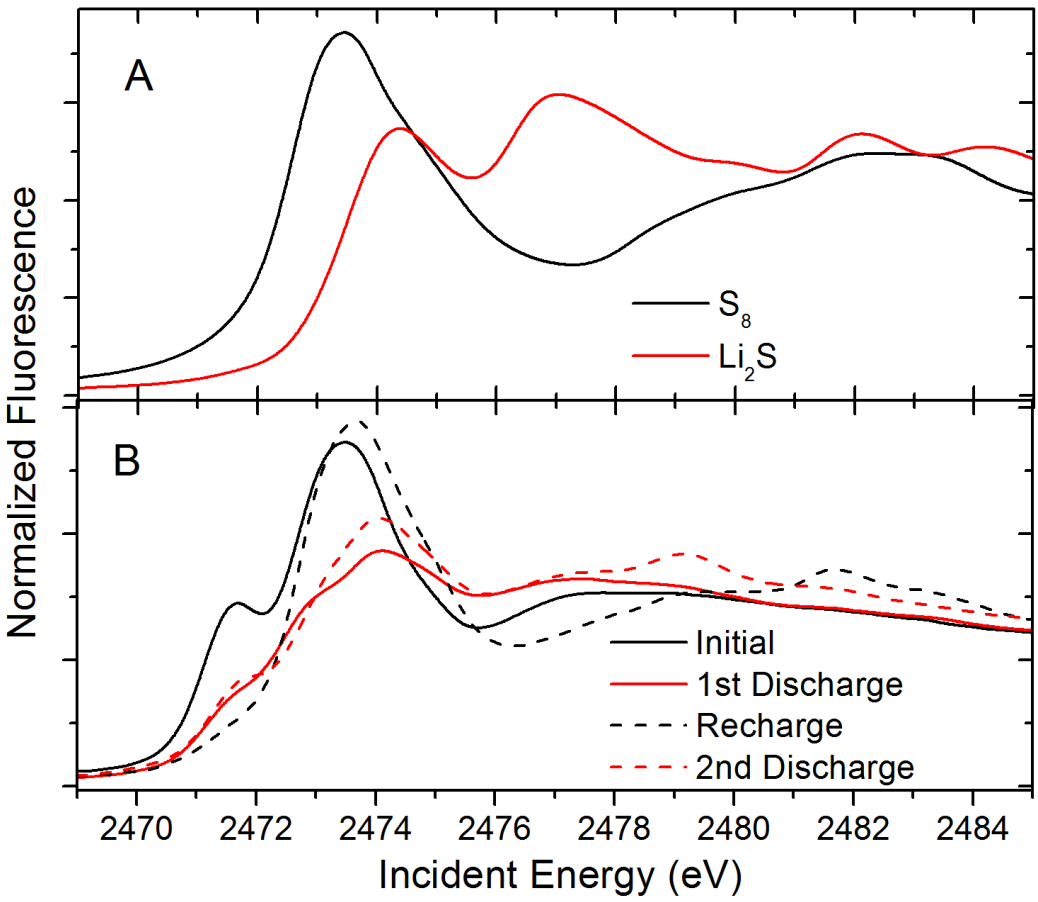

Figure 4-9. In-Operando sulfur K-edge XANES data for (A) standards of sulfur and lithium sulfide and (B) lithium sulfur battery at specified states points during the first two cycles. 1 M $LiClO_4$ in 1:1 dioxolane:dimethoxyethane used for battery electrolyte.

From a more fundamental perspective, the XANES signals for reduced sulfur species are significantly less intense than for oxidized sulfur compounds, with fewer distinct features.[65] The probability of absorption at the K edge is strongly influenced by bonding in the valence 3p orbitals,[55,65] with oxidized sulfur species forming a polar covalent bond and a larger transition dipole moment. At the same time, the contraction of the core electronic levels for oxidized sulfur results in a shift of the K edge, up to 13 eV in the case of SO_4^{2-}.[65] While catenation occurs for the reduced sulfur species, there is no similar enhancement in the transition probability and a much smaller shift in the

edge position. For example, comparison of the XANES for sulfur and lithium sulfide (Figure 4-9A) shows a shift of only 1 eV. The fact that the shift is to higher energies further complicates the analysis, since a simple orbital energy model would expect the edge to shift to lower energies with increased electronic density. This shift may be rationalized by the strong coulombic interactions between S_2^- and eight neighboring Li^+ ions;[7,57] however, this explanation means that lithium sulfide cannot be used to predict the magnitude or direction of the edge shift for polysulfide species. Moreover, as discussed above, the local structure sulfur atoms in many of the polysulfides is very similar. This raises serious concerns about the ability to resolve each chemical environment, especially since the width of the features is broad relative to the spectral range (FWHM ~ 1eV).

Despite these concerns, Figure 4-9B shows that several distinct features can be resolved from the in-operando XANES during the course of cycling. As the sulfur is reduced, the edge shifts to higher incident energy. This may indicate the charge of the polysulfides is more effectively screened by lithium ions at shorter chain lengths. While somewhat speculative, it is possible that the less-soluble shorter polysulfides precipitate as an amorphous lithium polysulfide, with increased coulombic shielding relative to the solution phase polysulfides. Several minor features also become more apparent in the spectra for the discharged battery. Perhaps most noticeably, all of the in-operando results have an additional peak at lower incident energy (2471.5 eV) that is not present in the spectra for sulfur or lithium sulfide. This peak energy matches the reported position for S_3^- contained in ultramarine pigments.[66] The presence of S_3^- is consistent with optical spectroscopic data discussed above, as well as reports of the unusual stability of the anion,[9] and the comparatively large shift in spectral position is consistent with the distinct electronic structure of radical anions versus dianions.

X-ray absorption is a promising technique for probing all sulfur species within

lithium-sulfur cells, including species that soluble and insoluble, crystalline and amorphous. However, the information content from the technique is fundamentally limited by the poor spectral acquisition, and additional control experiments are required to determine how the XANES changes for specific polysulfide compositions. Additionally, careful cell design and x-ray beam control is required to insure resolution of the intended region of the cell.

4.7 Conclusions

Based on the foregoing overview of the techniques and results for reduced sulfur species, it is safe to conclude that no single technique is adequate to characterize the complex ensemble of sulfur species formed in the operation of a lithium sulfur battery. Table 4-2 is a summary of the key criteria for the techniques reviewed in this chapter. In general there is a tradeoff between selectivity and the number of species detected. For UV-Vis, Raman, and XAS, this selectivity decreases as the chain length increases because of converging electronic and structural properties. However, for electrochemistry, UV-Vis, and XRD, the techniques as described in this chapter simply do not detect some of the sulfur species. This means that these techniques can only answer specific questions about the reactions in the cell.

UV-Vis is clearly the best technique for probing sulfur species in solution, and should be useful to more fully explain the reactions during the first portion of cell discharge when many sulfur species are in solution. However, the first portion of cell discharge only accounts for ~15% of the total capacity, and many lithium sulfur cells already approach the theoretical values. The best technique for probing sulfur species during the more critical second stage of battery operation is confocal Raman. Reactions during the second plateau appear to involve both insoluble and soluble species, with the observed capacity related to the rates of chemical equilibria which form the electroactive species. Confocal Raman can probe the spatially-resolved chemical and

morphological changes within and between the battery electrodes that appear to be related to significantly decreased capacity in the second voltage plateau. The comparatively long acquisition times are experimentally undesirable, but are not an issue for low-rate or quasi-equilibrium studies of the sulfur reaction mechanism.

Table 4-2. Summary of key metrics for applying analytical techniques to in-operando characterization of sulfur species in lithium-sulfur batteries.

Technique	Sulfur Species Detected	Typical Acquisition Time	Signal separation between distinct sulfur species	Spatial Resolution
Electrochemistry	Radical anions	< 30 s	Excellent for known reactions	<50 micron Limited by electrode size
Transmission UV-Vis	All soluble sulfur species	< 30 s	Good for shorter species (< 9 atoms)	< 1mm Limited by optics
Confocal Raman	All sulfur species	300-1200 s	Fair for shorter species Poor for > 6 atom chains Excellent for radical anions	< 50 micron
XRD	Crystalline S_8 and Li_2S	< 30 s (synchrotron) ~ 600 s (lab)	Excellent	< 100 micron Limited by window size
XANES	All sulfur species	300-600 s	Poor for polysulfides Good for radical S_3^-	< 1 mm Limited by beam optics

Even with excellent spatial and chemical selectivity, the inability to prepare single-component standards for any of the lithium polysulfides is a serious obstacle to fully characterizing the species present in the lithium sulfur battery, one that increases the importance of collecting complementary datasets using techniques with differing sensitivities (e.g. XANES and XRD, or UV-Vis and Raman). Additional efforts to model the structure and spectra for reduced sulfur species will also be valuable. However, in the end, the system will remain complex and difficult to fully decouple. Analysis with tools for multivariate curve resolution[67] will maximize the use of information available from each dataset.

The techniques reviewed in this chapter are only some of the analytical techniques that could be adapted to in-operando studies of the sulfur system. Some techniques have been specifically proposed that for development (i.e. DR-UV-Vs and confocal fluorescence microscopy) and others could be adapted with varying degrees of difficulty (e.g. electron spin resonance, nuclear magnetic resonance, non-resonant inelastic x-ray scattering, and advanced vibrational spectroscopy techniques, including polarization-modulation infrared reflection absorption spectroscopy). The challenges and advantages identified in this chapter can assist in the development of these techniques for in-operando characterization.

REFERENCES

(1) Sudworth, J. L.; Tilley, A. R. *The Sodium Sulfur Battery*; Chapman & Hall: London, 1985.

(2) Ryu, H.; Kim, T.; Kim, K.; Ahn, J.-H.; Nam, T.; Wang, G.; Ahn, H.-J. *J. Power Sources* **2011**, *196*, 5186–5190.

(3) Kim, H. S.; Arthur, T. S.; Allred, G. D.; Zajicek, J.; Newman, J. G.; Rodnyansky, A. E.; Oliver, A. G.; Boggess, W. C.; Muldoon, J. *Nature Communications* **2011**, *2*, 427.

(4) Berghof, V.; Sommerfeld, T.; Cederbaum, L. S. *The Journal of Physical Chemistry A* **1998**, *102*, 5100–5105.

(5) Meyer, B.; Peter, L.; Spitzer, K. In *Homoatomic Rings, Chains and Macromolecules of Main-Group Elements*; Rheingold, A. L., Ed.; Elsevier Scientific Publishing Company: Amsterdam, 1977; pp. 477–497.

(6) Luther III, G. W. *Geochim. Cosmochim. Acta* **1991**, *55*, 2839–2849.

(7) Gao, J.; Lowe, M. A.; Kiya, Y.; Abruna, H. D. *The Journal of Physical Chemistry C* **2011**.

(8) Eichinger, G.; Fritz, H. P. *Journal of Electroanalytical Chemistry and Interfacial Electrochemistry* **1975**, *58*, 369–374.

(9) Steudel, R. *Top. Curr. Chem.* **2003**, 127–152.

(10) Leghie, P.; Lelieur, J.-P.; Levillain, E. *Electrochem. Commun.* **2002**, *4*, 406–411.

(11) Meyer, B.; Peter, L.; Spitzer, K. *Inorg. Chem.* **1977**, *16*, 27–33.

(12) Williamson, M. A.; Rimstidt, J. D. *Geochimica et cosmochimica acta* **1992**, *56*, 3867–3880.

(13) Rauh, R. D.; Abraham, K. M.; Pearson, G. F.; Surprenant, J. K.; Brummer, S. B. *J. Electrochem. Soc.* **1979**, *126*, 523–527.

(14) Rauh, R. D.; Shuker, F. S.; Marston, J. M.; Brummer, S. B. *J. Inorg. Nucl. Chem.* **1977**, *39*, 1761–1766.

(15) Zhang, S. S.; Read, J. A. *J. Power Sources* **2012**, *200*, 77–82.

(16) Dubois, P.; Lelieur, J.; Lepoutre, G. *Inorg. Chem.* **1988**, *27*, 73–80.

(17) Han, D.-H.; Kim, B.-S.; Choi, S.-J.; Jung, Y.; Kwak, J.; Park, S.-M. *J. Electrochem. Soc.* **2004**, *151*, E283.

(18) Kim, B.-S.; Park, S.-M. *J. Electrochem. Soc.* **1993**, *140*, 115–122.

(19) Evans, A.; Montenegro, M. I.; Pletcher, D. *Electrochem. Commun.* **2001**, *3*, 514–518.

(20) Reimers, J. N.; Dahn, J. R. *J. Electrochem. Soc.* **1992**, *139*, 2091–2097.

(21) Balasubramanian, M.; Sun, X.; Yang, X.; McBreen, J. *Journal of power sources* **2001**, *92*, 1–8.

(22) Kodama, R.; Terada, Y.; Nakai, I.; Komaba, S.; Kumagai, N. *J. Electrochem. Soc.* **2006**, *153*, A583.

(23) Wang, F.; Robert, R.; Chernova, N. A.; Pereira, N.; Omenya, F.; Badway, F.; Hua, X.; Ruotolo, M.; Zhang, R.; Wu, L.; others *J. Am. Chem. Soc.* **2011**.

(24) McCloskey, B. D.; Bethune, D. S.; Shelby, R. M.; Girishkumar, G.; Luntz, A. C. *The Journal of Physical Chemistry Letters* **2011**, *2*, 1161–1166.

(25) Ji, X.; Nazar, L. F. *J. Mater. Chem.* **2010**, *20*, 9821.

(26) Peled, E.; Sternberg, Y.; Gorenshtein, A.; Lavi, Y. *J. Electrochem. Soc.* **1989**, *136*, 1621–1625.

(27) Kumaresan, K.; Mikhaylik, Y.; White, R. E. *J. Electrochem. Soc.* **2008**, *155*, A576–A582.

(28) Dominko, R.; Demir-Cakan, R.; Morcrette, M.; Tarascon, J.-M. *Electrochem. Commun.* **2011**, *13*, 117–120.

(29) Merritt, M. V.; Sawyer, D. T. *Inorg. Chem.* **1970**, *9*, 211–215.

(30) Martin, R. P.; Doub Jr, W. H.; Roberts Jr, J. L.; Sawyer, D. T. *Inorg. Chem.* **1973**, *12*, 1921–1925.

(31) Paris, J.; Plichon, V. *Electrochim. Acta* **1981**, *26*, 1823–1829.

(32) Gaillard, F.; Levillain, E.; Lelieur, J. P. *J. Electroanal. Chem.* **1997**, *432*, 129–138.

(33) Levillain, E.; Gaillard, F.; Leghie, P.; Demortier, A.; Lelieur, J. *J. Electroanal. Chem.* **1997**, *420*, 167–177.

(34) Seel, F.; Guttler, H.-J.; Simon, G.; Wieckowski, A. *Pure Appl. Chem.* **1977**, *49*, 45–54.

(35) Marmorstein, D. Solid state lithium/sulfur batteries for electric vehicles: Electrochemical and Spectroelectrochemical Investigations, University of California, Berkeley, 2002.

(36) Steudel, R. *Inorganic Ring Systems* **1982**, 149–176.

(37) Janz, G. J.; Downey Jr, J. R.; Roduner, E.; Wasilczyk, G. J.; Coutts, J. W.; Eluard, A. *Inorg. Chem.* **1976**, *15*, 1759–1763.

(38) Janz, G. J.; Coutts, J. W.; Downey Jr, J. R.; Roduner, E. *Inorg. Chem.* **1976**, *15*, 1755–1759.

(39) Eckert, B.; Steudel, R. *Top. Curr. Chem.* **2003**, 181–191.

(40) Gaillard, F.; Levillain, E.; Dhamelincourt, M.-C.; Dhamelincourt, P.; Lelieur, J. P. *J. Raman Spectrosc.* **1997**, *28*, 511–517.

(41) Ledé, B.; Demortier, A.; Gobeltz-Hautecœur, N.; Lelieur, J.-P.; Picquenard, E.; Duhayon, C. *J. Raman Spectrosc.* **2007**, *38*, 1461–1468.

(42) Luo, Y.; Cai, W.-B.; Xing, X.; Scherson, D. A. *Electrochemical and Solid-State Letters* **2004**, *7*, E1.

(43) Panitz, J. C.; Novák, P.; Haas, O. *Appl. Spectrosc.* **2001**, *55*, 1131–1137.

(44) Morcrette, M.; Chabre, Y.; Vaughan, G.; Amatucci, G. G.; Leriche, J.-B.; Patoux, S.; Masquelier, C.; Tarascon, J.-M. *Electrochim. Acta* **2002**, *47*, 3137–3149.

(45) Meyer, B. *Chem. Rev.* **1976**, *76*, 367–388.

(46) Sharma, R. A. *J. Electrochem. Soc.* **1972**, *119*, 1439–1443.

(47) Okamoto, H. *J. Phase Equilib.* **1995**, *16*, 94–97.

(48) Sangster, J.; Pelton, A. D. *Journal of phase equilibria* **1997**, *18*, 89–96.

(49) Sangster, J.; Pelton, A. D. *J. Phase Equilib.* **1997**, *18*, 82–88.

(50) Braun, A.; Shrout, S.; Fowlks, A.; Osaisai, B.; Seifert, S.; Granlund, E.; Cairns, E. *Journal of Synchrotron Radiation* **2003**, *10*, 320–325.

(51) Nikolowski, K.; Baehtz, C.; Bramnik, N. N.; Ehrenberg, H. *J. Appl. Crystallogr.* **2005**, *38*, 851–853.

(52) Hassoun, J.; Sun, Y. K.; Scrosati, B. *J. Power Sources* **2011**, *196*, 343–348.

(53) Cavalleri, M.; Odelius, M.; Nordlund, D.; Nilsson, A.; Pettersson, L. G. M. *Phys. Chem. Chem. Phys.* **2005**, *7*, 2854.

(54) Neese, F. *ORCA – an ab initio, Density Functional and Semiempirical program package*; University of Bonn, 2008.

(55) Solomon, E. I.; Hedman, B.; Hodgson, K. O.; Dey, A.; Szilagyi, R. K. *Coord. Chem. Rev.* **2005**, *249*, 97–129.

(56) Kravtsova, A.; Stekhin, I.; Soldatov, A.; Liu, X.; Fleet, M. *Phys. Rev. B* **2004**, *69*.

(57) Alonso Mori, R.; Paris, E.; Giuli, G.; Eeckhout, S. G.; Kavčič, M.; Žitnik, M.; Bučar, K.; Pettersson, L. G. M.; Glatzel, P. *Anal. Chem.* **2009**, *81*, 6516–6525.

(58) Métrich, N.; Berry, A. J.; O'Neill, H. S. C.; Susini, J. *Geochim. Cosmochim. Acta* **2009**, *73*, 2382–2399.

(59) Beauchemin, S.; Hesterberg, D.; Beauchemin, M. *Soil Sci. Am. J.* **2002**, *66*, 83–91.

(60) Frank, P.; George, S. D. .; Anxolabéhère-Mallart, E.; Hedman, B.; Hodgson, K. O. *Inorg. Chem.* **2006**, *45*, 9864–9876.

(61) Lefebvre-Devos, I.; Olivier-Fourcade, J.; Jumas, J. C.; Lavela, P. *Physical Review B 61*, 3110–3116.

(62) Totir, D. A.; Antonio, M. R.; Schilling, P.; Tittsworth, R.; Scherson, D. A. *Electrochim. Acta* **2002**, *47*, 3195–3200.

(63) Branci, C.; Sarradin, J.; Olivier-Fourcade, J.; Jumas, J. C. *Chem. Mater.* **1999**, *11*, 2846–2850.

(64) Krause, M. O. *J. Phys. Chem. Ref. Data* **1979**, *8*, 307–327.

(65) Jalilehvand, F. *Chem. Soc. Rev.* **2006**, *35*, 1256.

(66) Fleet, M. E.; Liu, X. *Spectrochim. Acta B* **2010**, *65*, 75–79.

(67) de Juan, A.; Tauler, R. *Crit. Rev. Anal. Chem.* **2006**, *36*, 163–176.

CHAPTER 5

ELECTROCHEMICAL AND COMPUTATIONAL STUDIES OF THE SULFUR REDUCTION MECHANISM IN LITHIUM ELECTROLYTE SOLUTIONS

5-1. Introduction

The lithium-sulfur (Li-S) system is arguably the most promising prospect for next-generation high energy density electrochemical energy storage. Lithium and sulfur have a theoretical charge storage capacity of over 1600 mAh/g-sulfur and typical discharge voltage near 2 V, for an overall energy density of well over 2000 Wh/kg-S. On a gravimetric basis, these numbers indicate that Li-S could have up to an order of magnitude higher energy density than current technologies. Although the density of both lithium and sulfur are significantly below those of active materials in lithium-ion batteries, the Li-S system is still expected to provide comparable volumetric energy density due to the exceptional gravimetric capacity of the pure components. Furthermore, both can be included in battery electrodes in their condensed, elemental form at room temperature and pressure, simplifying electrochemical cell design and fabrication.

Despite the tremendous promise, the Li-S system has yet to find broad application. Most reports of Li-S energy storage cells show first cycle capacities far below predicted values (often below 50%[1] and almost universally below 85%[2,3] of the theoretical 1672 mAh/g) and subsequent cycling shows significant capacity fading. In general, the best performance to date has been obtained from composites of sulfur with high surface area and/or nanostructured carbon,[2,4–9] especially at low loadings of sulfur to carbon.[10] Based on the electrochemical results from sulfur cathodes in coin

cells, several researchers have proposed the poor performance to be due to loss of polysulfides into solution[3] or poor utilization of the active materials due to the formation of electrically insulating deposits of Li_2S, Li_2S_2, or S_8.[4,10,7,11] Unfortunately, these researchers have typically proposed these failure modes without in-situ spectroscopic or diffraction for support, making these proposals interesting but speculative and leaving their influence entirely impossible to quantify.

The actual causes of system failure remain an area of active research because of the complexity of sulfur chemistry. The combination of electronegativity, diffuse electron density, and d-orbitals results in sulfur exhibiting many types of bonding and reactivity. Elemental sulfur forms more allotropes than any other element,[12] and the reduced sulfur species with different chain lengths, charges, and structures forms a "zoo" of possible intermediate states between the neutral ring S_8 and the fully reduced sulfide. In light of this complexity, it is not surprising that the mechanism for the electrochemical reduction of sulfur to lithium sulfide is incompletely understood, even though this mechanism is of supreme importance to understand the operation of Li-S cells. For example, is the almost universal failure to obtain theoretical capacity due to practical or fundamental reasons? What are the kinetic limitations and thus the limiting power density? What phenomena are responsible for the poor cyclability? The answers to these and related questions determine the practicality of wide-scale implementation of the Li-S system.

Electrochemistry probes the thermodynamics and kinetics of electron-transfer events, and thus it would seem to be an ideal probe of the sulfur reduction reactions. Electrochemical techniques directly detect those species that have charge transfer kinetics sufficiently fast to result in measureable current in the experimental time scale, and also indirectly probe chemical equilibria involving electroactive species, as long as the rate constant for the chemical reaction falls within the time window of the

technique. (Table 5-1) When multiple techniques are used, it is possible to confirm hypotheses of reaction mechanisms and extract correlated variables (e.g. n and D, the number of electrons passed and the diffusion coefficient for the species). Unfortunately, the sensitivity of electrochemistry is balanced by its lack of chemical specificity, since all thermodynamically favored, kinetically facile electron transfer reactions will contribute to the signal. This can complicate interpretation of results from complex systems, such as the reduction of elemental sulfur.

Over the years a number of researchers have used electrochemistry as a probe of the reduction mechanism of elemental sulfur with varying conclusions about the operative reduction mechanism. Some of the earliest reports of sulfur electrochemistry in aprotic solutions came from the Sawyer group in the early 1970s. They observed two nearly equal reduction waves separated by about 0.6 V and, based on chronopotentiometry and UV-Vis spectroscopy, initially assigned the respective processes to the chemical steps:[13]

$$S_8 + e^- \rightarrow S_8^- \text{ (first wave) (1)}$$

$$2S_8^- \leftrightarrow (S_8^-)_2 \text{ (K >> 1, } k_b \text{ fast) (2)}$$

$$S_8^- + e^- \rightarrow S_8^{2-} \text{ (second wave) (3)}$$

A subsequent report from Bonnaterre and Cauquis[14] also observed two reduction waves of nearly equal intensity, but correctly determined that each wave corresponded to 2 e^-/S_8. With the support of UV-Vis spectroscopy during bulk electrolysis, these researchers proposed the following reduction and disproportionation processes:

$$S_8 + 2e^- \rightarrow S_8^{2-} \text{ (first wave) (4)}$$

$$4S_8^{2-} \leftrightarrow 4S_6^{2-} + S_8 \text{ (5)}$$

$$S_6^{2-} + 2e^- \rightarrow \rightarrow S_4^{2-} \text{ (second wave) (6)}$$

Unfortunately, while this mechanism is consistent with their assignments of the spectral features, the exact mechanisms for reactions 5 and 6 were neither clearly

identified nor chemically intuitive. A subsequent publication from the Sawyer group supported the spectroscopic conclusions of Bonnaterre and Cauquis, but assigned the second reduction wave to a different reaction:

$$S_8^{2-} + 2e^- \rightarrow S_8^{4-} \quad (7)$$

$$S_8^{4-} \leftrightarrow 2S_4^{2-} \quad (8)$$

$$S_4^{2-} + S_8^{2-} \leftrightarrow 2S_6^{2-} \quad (9)$$

An appreciable concentration S_6^{2-} was observed and ascribed to reactions 5 and 9 but not considered to play a significant role in the electrochemistry. This is at variance with slightly later reports by Delamar et al.[15,16] who proposed S_6^{2-} could be reduced and slowly equilibrate to form S_4^{2-}:

$$S_6^{2-} + 2e^- \rightarrow 2S_3^{2-} \quad (10)$$

$$S_6^{2-} + 2S_3^{2-} \leftrightarrow 3S_4^{2-} \quad (11)$$

Paris and Plichon[17] supported the reactions proposed in earlier reports, but specified that the radical anion S_3^- was the most probable electroactive species:

$$S_6^{2-} \leftrightarrow 2S_3^- \quad (12)$$

$$S_3^- + e^- \rightarrow S_3^{2-} \quad (13)$$

UV-Vis spectroscopy and rotating disk voltammetry supported their conclusion that the second wave was due to the reduction of S_3^- anions and had S_4^{2-} as a product. The most recent conceptual contribution from electroanalytical studies of sulfur stemmed from a series of papers from Lelieur et al.[18–22] Using cyclic voltammetry, potential steps, and in-situ UV-Vis spectroelectrochemistry, the researchers made assignments for both observed reduction waves and fit a detailed mechanism to the electrochemical data to obtain kinetic and thermodynamic parameters. In the first wave, the researchers proposed the following steps:

$$S_{8,c} + e^- \rightarrow S_{8,c}^- \text{ (c = cyclic conformation)} \quad (14)$$

$$S_{8,c}^- \leftrightarrow S_{8,l}^- \text{ (l = linear chain conformation)} \quad (15)$$

$$S_{8,l}^{-} + e^{-} \rightarrow S_{8,l}^{2-} \quad (16)$$

The reduction potential of the linear polysulfide was proposed to be more positive than the cyclic anion due to stabilizing the negative charge on terminal sulfur atoms,[23,24] although not all researchers support the ring-opening mechanism.[25,26]

In the second reduction wave, Lelieur et al. concluded that the only electroactive species were the radical anions S_4^- and S_3^-, with S_3^- the dominant electroactive species in DMF under electroanalytical conditions and cyclic voltammetric time scales.[18,22]

$$S_{8,l}^{2-} \leftrightarrow 2S_4^{-} \quad (17)$$

$$S_4^{-} + e^{-} \rightarrow S_4^{2-} \quad (18)$$

$$4S_8^{2-} \leftrightarrow 4S_6^{2-} + S_8 \quad (5)$$

$$S_6^{2-} \leftrightarrow 2S_3^{-} \quad (12)$$

$$S_3^{-} + e^{-} \rightarrow S_3^{2-} \quad (13)$$

While the work from Lelieur et al. has presented the most complete and self-consistent mechanism for reduction of sulfur, the authors' extensive use of simulations to extract reaction parameters has been a source of concern. Also disconcerting is the heavy reliance on the high-order, non-elementary disproportionation reaction 5 to generate the electroactive S_3^- species in the second wave.

Several additional publications have examined the influence of different solvents,[26,27] electrode materials,[26] and temperature[28] on the cyclic voltammetry of sulfur but have not proposed alternate reaction pathways or used voltammetric (i.e. steady-state) techniques. The most recent electrochemical studies have focused on understanding the reduction mechanism of sulfur in the battery environment, but again have used techniques (e.g. cyclic voltammetry[29] and electrochemical impedance spectroscopy[30–32]) from which it can be difficult to obtain kinetic and thermodynamic parameters for a complex, multi-step reaction.

As part of an extended study on the reactions in the lithium-sulfur system, this

research applies several electroanalytical techniques to the study of sulfur reduction in lithium-containing tri(ethyleneglycol)dimethylether (triglyme), a proposed solvent for lithium-sulfur batteries. Electrochemical methods will not, by themselves, identify the chemical identities of the reactants, but the results can support a proposed mechanism. In this work, our intent was to determine the dominant features of the electrochemical reduction mechanism for sulfur in an ethereal solvent, using as a point of departure the mechanism proposed by Lelieur. Since most of the electroanalytical studies have been performed in higher-dielectric media (e.g. DMF), the application of electoanalytical methods (i.e. cyclic voltammetry,chronoamperometry, rotating disk electrode voltammetry, and ultramicroelectrode voltammetry) in a technologically-relevant solvent provides a foundation for additional understanding of the sulfur reduction mechanism in prototype batteries. Quantum chemical computations of reduction potentials and thermodynamic relationships provides additional insights into which processes are thermodynamically favored during the first or second reduction process.

Table 5-1. Time Windows for Electrochemical Techniques[33]

Electrochemical Technique	Time Window (s)	Physical Constraints on upper limit of time window
Rotating Disk Electrode Voltammetry	10^{-3}-0.03	Breakdown of laminar flow due to convection
Ultramicroelectrode	10^{-5}-1	Onset of convection
Chronopotentiometry	10^{-6}-50	Onset of convection
Chronoamperometry	10^{-7}-10	Onset of convection
Cyclic Voltammetry	10^{-7}-1	Onset of convection
Coulometry	100-3000	Migration from counter electrode (when applicable)

5-2. Electroanalytical Results

A. Cyclic Voltammetry

Cyclic voltammetry (CV) is not a steady-state technique, making it difficult to decouple kinetic and thermodynamic parameters, but it is a useful technique to provide a quick survey of the electrochemical response. Figure 5-1 presents the cyclic voltammetric (CV) response of a dilute sulfur solution (2 mM S_8) in triglyme. Two distinct reduction peaks are observed at 2.3 and 2.0 V vs. Li/Li^+, as has been reported previously for sulfur in a wide range of solvents.[26] The voltage between peaks is much smaller than in higher-dielectric organic solvents (e.g. DMSO and DMF)[22,23,26] but is consistent with the CV peak separation in other ethereal solvents.[26,27] The presence of two peaks supports a mechanism dominated by reduction of a limited number of species. However, the current transients in the mass transport controlled region (after the reduction peak) are higher than the expected diffusional ($t^{-1/2}$) response, leaving

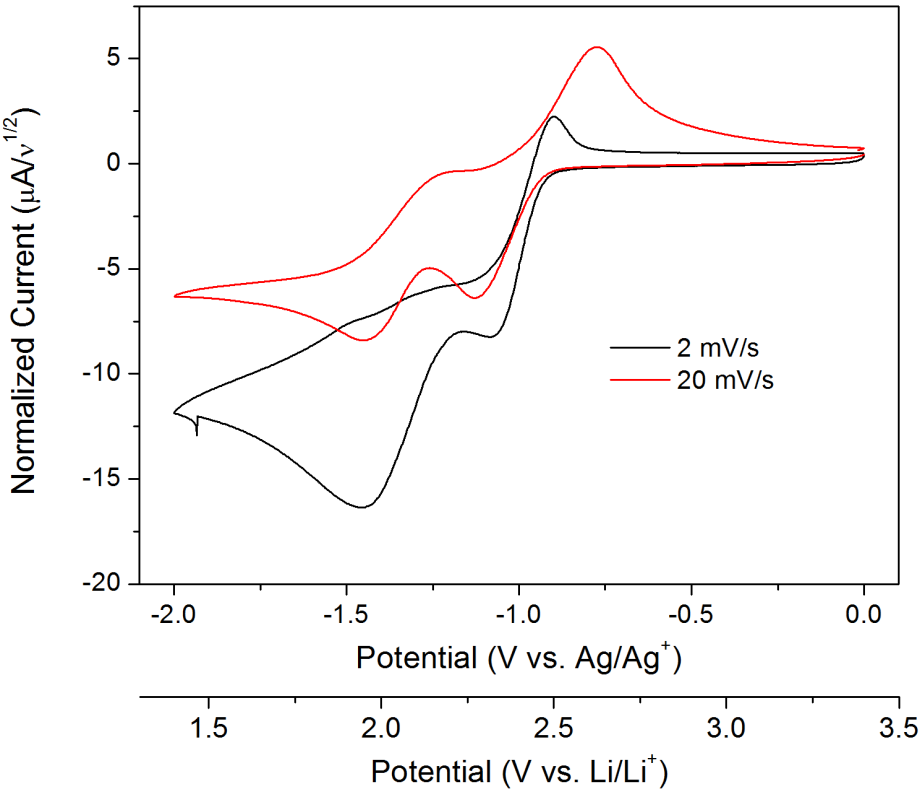

Figure 5 - 1. Cyclic voltammetry of elemental sulfur at glassy carbon electrode in triglyme at selected sweep rates. 2 mM S_8 + 0.1 M LiTFSI + triglyme.

open the possibility for minor contributions from other sulfur species. At 20 mV/s, the first reduction peak is significantly larger than the second, while at 2 mV/s the peak heights are comparable, in agreement with a series of chemical steps between the first and second electroactive species. Interestingly, and unlike in DMF,[19,26] both peaks are largely irreversible. The lower dielectric of triglyme apparently favors additional chemical steps that consume the reduced species, especially the reduced species from the second wave.

B. Chronoamperometry

In order to probe the first reduction reactions, we used used a potential step to the middle of the first reduction wave. Chronoamperometry is a versatile technique for probing chemical reactions, with the capability to probe both long and short timescales. The current transient after a potential step can provide a diagnostic probe

of the induced reaction, with experimental and theoretical models for electrodeposition,[34] preceding and following chemical reactions,[33,35] and chemical reactions between two electron transfers[36] – such as that predicted by Lelieur et al. in reactions 14-16. The latter case has a distinctive response. When plotted in Cottrell space (current vs. $t^{-1/2}$) the reponse exhibits two straight lines from the first and second electron transfer, with a cross-over between regimes defined by the rate of the intervening chemical step.[36]

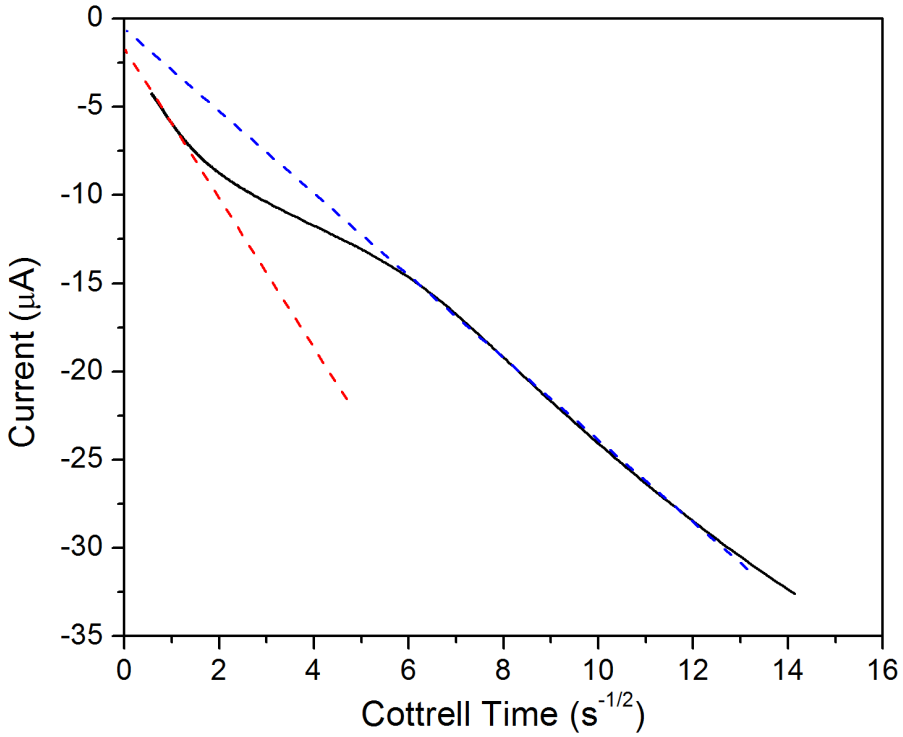

Figure 5-2. Current transient after potential step to 2.3 V vs. Li/Li^+ in 2 mM S_8 + 0.1 M LiTFSI + triglyme. 2 mm diameter glassy carbon electrode.

Figure 5-3 shows the current transient obtained in a sulfur solution at a glassy carbon electrode after a potential step from open circuit to 2.3 V vs. Li/Li^+. As expected for an ECE mechanism, there are clearly two diffusional regimes corresponding to the first and second electron transfer, with the second slope (red line) roughly twice as large as the first (blue line). If the first regime corresponds to a 1 e^- reduction, the diffusion coefficient for sulfur in triglyme is $6e^-6$ cm^2/s. This is all consistent with

reactions 14-16, but a closer inspection of the data does raise some interesting questions. While the first slope has an intercept very close to zero, as expected for a purely diffusional process, the second slope has a clearly non-zero intercept. The step time is still short enough (1-15 seconds) and the electrode large enough that mass transport should be dominated by semi-infinite linear diffusion. This implies that the non-zero intercept is due to additional reduction processes, beyond those proposed by Lelieur et al., occurring at the potential of the first reduction peak in the CV. This is consistent with the non-diffusional current transient after the first reduction peak (Figure 5-1) and may be consistent with the disproportionation reaction 5, even though the molecularity of the reaction appears chemically unreasonable.

The cross-over between diffusional regimes can be used to estimate the forward rate of the intervening chemical step. Conceptually, the cross-over is a measure of when the system shifts from a 1 e^- process to a 2 e^- process, and can be resolved by plotting the normalized current ($i_{obs}/i_{theoretical,2e-}$) as a function of time. The exact relationship is complex, but working curves are available for comparison with experimental results.[33,36] For sulfur in triglyme, this analysis yields an estimated rate of 5.4 +/- 0.5 s^{-1}. This is significantly smaller than reported previously (e.g. 200 s^{-1} based on curve-fitting CVs in DMF). The additional reduction processes occurring at longer times means this rate is a lower limit, since additional reduction current will appear to delay the cross-over from 1 to 2 electrons.

C. Rotating Disk Electrode Voltammetry

Unlike cyclic voltammetry and chronoamperometry, rotating disk electrode (RDE) voltammetry is a steady-state technique. Rotation of the electrode establishes a region of laminar flow at the electrode surface, within which transport to the electrode surface occurs via diffusion. Control of the rotation rate varies the thickness of this diffusion layer and thus the residence time for electroactive species. For the relevant

time window (Table 5-1) RDE offers exceptional control of the electrochemical conditions, and can be used to obtain both qualitative and quantitative information about reaction mechanisms. It was attractive to use RDE voltammetry to further investigate the chemical reactions coupled to both reduction waves.

An important initial experiment for RDE is to verify that the response is truly steady state, that is, independent of voltage ramp rate. Figure 5-3 presents the initial sweep rate dependence, and at moderate sweep rates (5-10 mV/s) the response is largely steady state. Surprisingly, the electrode at lower sweep rates the electrode was passivated after the second reduction wave. After continued equilibration the electrode recovers its activity, indicating that the deposited species can comproportionate and/or redissolve, but this result is an important caution for RDE work in the sulfur system. The dramatically varying solubility of reduced sulfur species (ranging from >10 M for Li_2S_8 to <1 mM for Li_2S) means that the lowest polysulfides can deposit on the electrode surface even if they are a minor product of the reaction. This will complicate the analysis whenever a significant charge is passed into solution, as occurs with the slowest sweep rates. Indeed, since the products that cause passivation at 2 mV/s are also forming at the other sweep rates, the RDE results are dependent on the rate of the precipitation being slower than the rate of comproportionation. The unknown rates, and how these rates are affected by the diffusion layer thickness, raise serious questions about obtaining quantitative results from the RDE of sulfur solutions. Indeed, if polysulfides adsorb or precipitate on the electrode surface, even the qualitative trends observed in the RDE response could be obfuscated.

Indirect evidence that polysulfides do precipitate on the electrode surface, even at faster sweep rates, is apparent in the hysteresis between the scans to cathodic and anodic potentials. (Figure 5-3) In every sweep, the sweep to anodic potentials is shifted to more negative potentials, consistent with accumulation of reduced sulfur

species and a non-equilibrium condition. Thus, although features of response are typical for RDE, the sulfur system is clearly too complex for straightforward resolution via RDE analysis. Additional experiments were conducted at 5 mV/s with the only objective being qualitative insights into the types of reactions during sulfur reduction.

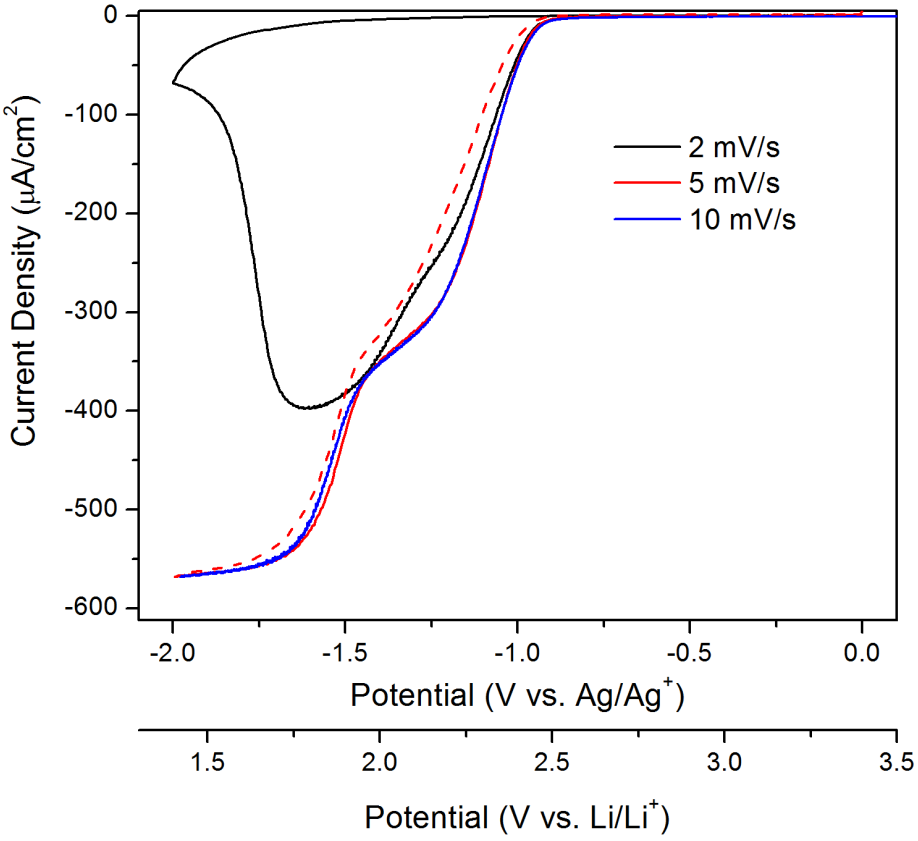

Figure 5- 3. Sweep rate dependence of sulfur RDE response. 2 mM sulfur + 0.1 M LiTFSI + triglyme, with 5 mm diameter glassy carbon electrode, rotating at 100 rpm. Dashed line is the anodic sweep at 5 mV/s.

As seen in Figure 5-4, varying the rotation rate results in systematic variation of the position and intensity of both reduction waves. The first wave both shifts to larger overpotentials and decreases in slope. Interestingly, the wave appears to split into multiple shoulders at higher rotation rate, suggesting multiple reduction processes occur during this potential range. Even at low rotation rates, the wave does not exhibit

a typical mass-transport-limited response. This is consistent with the cyclic voltammetry at slow sweep rates, where the current transient after the first peak is also

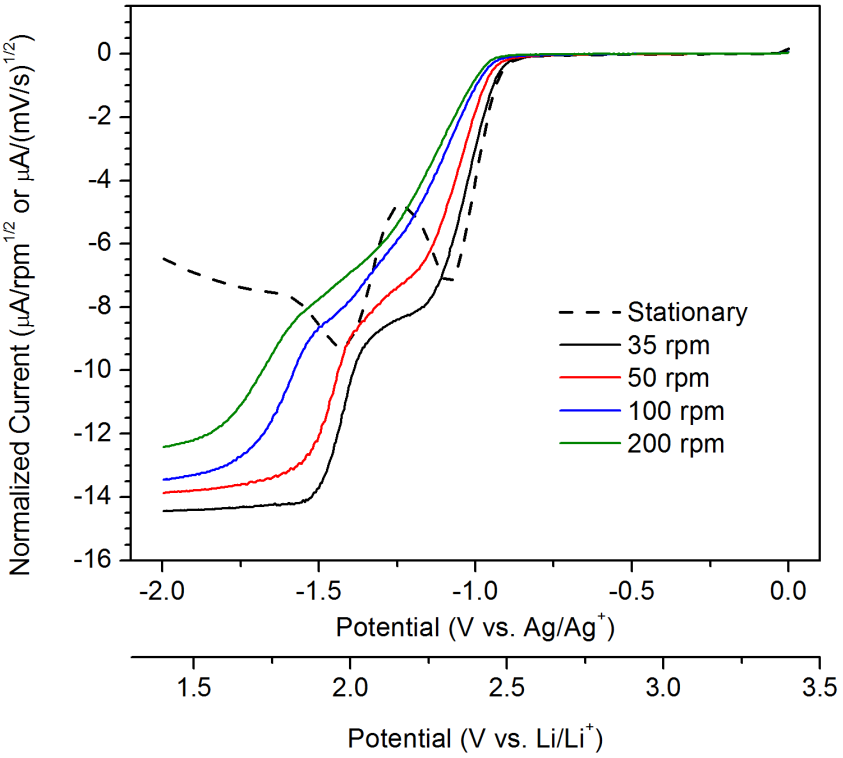

Figure 5- 4. Rotation rate dependence in RDE response. 2 mM sulfur + 0.1 M LiTFSI + Triglyme. Measured with a 5 mm diameter glassy carbon RDE.

not purely diffusional (Figure 5-1). The identity of the additional redox-active species is unknown, but will be discussed in more detail below.

The reduction wave shifts to more negative potentials as it splits into two shoulders and as the rotation rate increases. The combination of peak shift and diminished wave height is in agreement with homogeneous comproportionation that reduces some of the neutral sulfur. For example:

$$S_{8,c} + S_{8,l}^{2-} \leftrightarrow S_{8,l}^{-} + S_{8,c}^{-} \quad (19)$$

However, Lelieur et al. considered this reaction and, based on models of CVs, estimated that the comproportionation was heavily disfavored, at least in DMF.[19] Alternately, the faster rotation rates may decrease the overall wave height due to loss

of the intermediate reduced species S_8c-. The apparent shift in half-wave potential may be due to convolution of the reduction of S_8 with other sulfur species with similar reduction potentials, as discussed below.

Unlike the first reduction wave, the second wave does exhibit a steady-state plateau at slow rotation rates, supportive of the assignment to a single sulfur species (i.e. S_3^-).[18] This is in contrast with the CV results, which show both peaks have non-diffusional tails, but is a consequence of the different time scales for CV and RDE. Since RDE only probes chemical reactions that occur within the diffusion layer, it is more difficult to probe slow chemical steps – such as those occurring at or more negative of the second wave – using RDE than using CV.

With increasing rotation rate, the second reduction wave also shifts to more negative potentials and noticeably decreases in intensity. The decreased wave height is almost certainly due to the kinetics of the chemical step to form the electroactive species, but the cathodic shift could be due to several factors. The shift is as expected for a chemical reaction that consumes the reduced product, but may also be explained by slower diffusion or even precipitation of the reduced species. The latter processes may also explain the hysteresis observed between forward and reverse sweeps (Figure 5-3). Interestingly, the slope of the second reduction wave is consistently larger than the slope of the first wave. While not quantitative, this does indicate that the charge transfer kinetics of the second reduction process is faster than the first, consistent with the reports from Lelieur et al. for the reduction of S_8($k=4E^-3$ cm/s)[19] and the lower radical anions S_3^- or S_4^- ($8E^-3$ cm/s)[18] in DMF.

5-3. Computational Predictions of Reduction Potentials

The electrochemical results are largely consistent with the mechanism reported by Lelieur et al., but all three techniques suggest the presence of additional reduction steps between the first and second peaks/waves. The identity of these electroactive

species has not yet been chemically characterized, but quantum chemical (QC) calculations may be used to establish which reduction processes are most reasonable. Over the last twenty years, QC has developed into a mature technique with several easily accessible software packages for investigations of electronic structure and chemical reactions. Researchers in several groups, including the Abruña group, have demonstrated that reduction potentials can be calculated with reasonable accuracy (generally < 100 mV mean unsigned error over a wide range of structures)[37–39] even using computationally-inexpensive density functional theory (DFT). In molecules with small structural reorganizations, the energy of the lowest unoccupied molecular orbital (LUMO) can be directly correlated to the reduction potential; for most molecules, including the sulfur species, the reorganization is sufficiently large that the reduction potential should be directly calculated from the free energy difference between the oxidized and reduced species. In the results presented below, each calculation was performed using a polarizable continuum solvent model to correct for the effects of solvation, but no correction was made for entropic contributions to the free energy. The predicted reduction potentials were then scaled to match the observed reduction potentials, assuming that the first and second reduction peaks were close to the reduction potentials for S_8 and S_3^-. Although this procedure results in reduction potentials that appear electrochemically reasonable, the most important result is the relative reduction potential.

Figure 5-5 summarizes the calculated reduction potentials for a number of sulfur species that could participate in the reduction of elemental sulfur, including cyclic sulfur, S_8, radical anions S_n^-, $1 \leq n \leq 10$, and a representative dianion, S_6^{2-}. The reduction potential of the radical anions is almost linear with the inverse chain length over the interval $3 \leq n \leq 10$. This is reminiscent of the variation of oxidation potential with oligomer length in conducting polymers, where longer oligomers are more easily

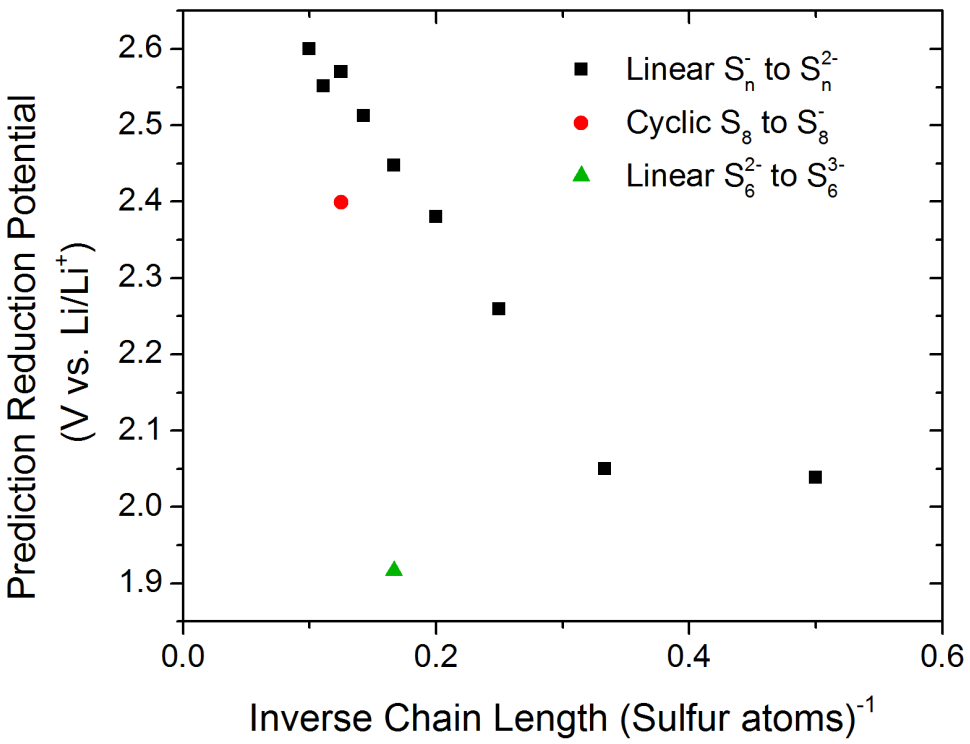

Figure 5- 5. QC predicted one electron reduction potentials for sulfur species. Energy of oxidized and reduced sulfur species without lithium ions calculated using B3LYP with 6-311++G(2df) basis set.

oxidized due to increased electronic delocalization .[40] The presence of delocalized bonding in the polysulfides has been proposed[41] and is supported by inspection of the topology of the frontier molecular orbitals, all of which have significant π-type bonding interactions along the sulfur chain. (Figure 5-6)

The reduction potential of cyclic elemental sulfur (2.40 V) is significantly more negative than the value predicted for the neutral 8-sulfur chain (not shown, 2.93 V). The negative shift is a consequence of the stability of the neutral ring structure: the cyclic conformation is most stable for sulfur clusters larger than S_4,[42] and among the sulfur rings S_8 also has the least steric strain.[43] Electrochemically, the negative shift of the neutral ring results in the second reduction having a greater driving force than the first reduction, and further supports the ECE-type mechanism proposed for the initial

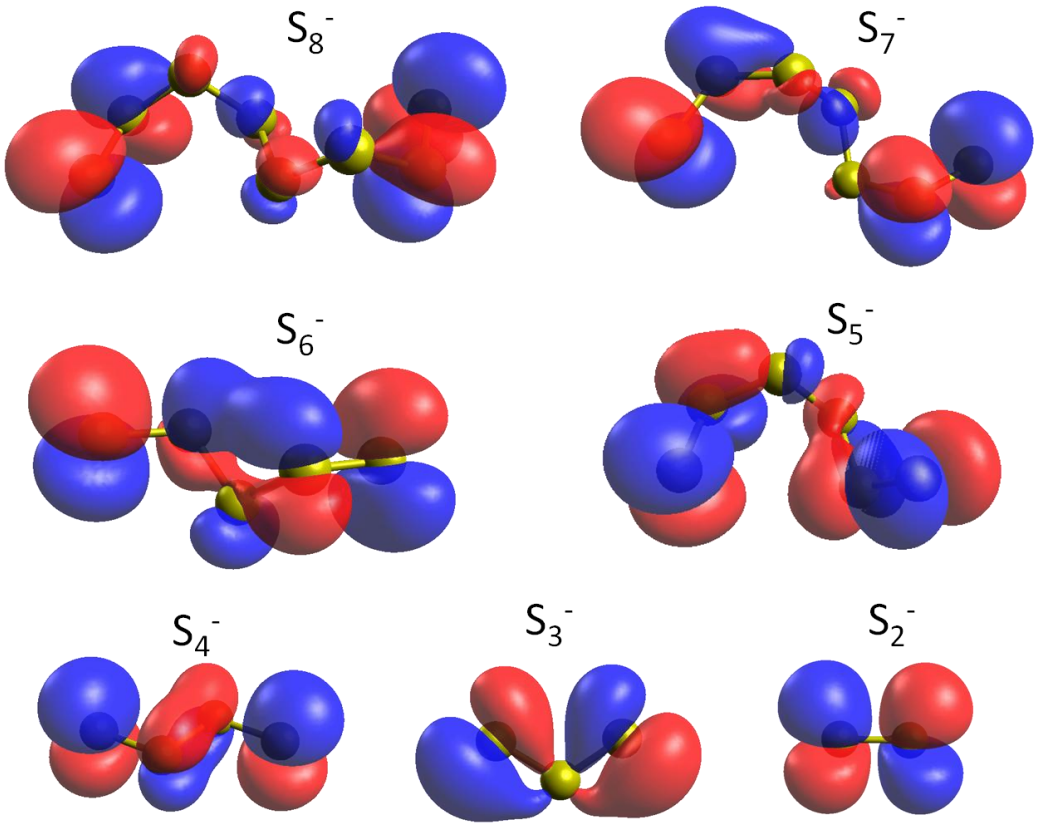

Figure 5-6. Highest occupied molecular orbitals for polysulfide radical anions.

reduction of elemental sulfur.[23] The ordering of the predicted reduction potentials are also consistent with previous estimates of the reduction potentials for S_8,c and S_8,l- in DMF.[22]

These results indicate that linear anions longer than n = 4 can be reduced at or close to the same potential as cyclic elemental sulfur. Although Lelieur et al. reported that S_8 and radical anions are the only species that can be electrochemically reduced in DMF,[20] their report only considers the reduction of S_8l- in the first wave and the shorter radical anions S_4^- and S_3^- in the second reduction wave. The possibility of reducing longer chain radical anions opens additional reduction pathways. For example, after reducing cyclic S_8 to linear S_8^{2-} in reactions 14-16, the dianion could comproportionate with neutral sulfur to form additional electroactive long-chain

radical anions:

$$S_{8,c} + S_{8,l}^{2-} \leftrightarrow S_x^- + S_y^- \quad (x+y=16) \quad (20)$$

Alternately, the S_8^{2-} could unimolecularly dissociate into radical anions, one of which is electroactive:

$$S_{8,l}^{2-} \leftrightarrow S_x^- + S_y^- \quad (x>4,\ x+y=8) \quad (21)$$

We can predict which reactions are thermodynamically favored by a simple comparison of the energies of reactants and products, as shown in table 5-2. This comparison is admittedly primitive, since it does not include any barrier calculations for kinetics, nor the effect of applied potential and lithium interactions; however, it provides a first perspective on the distribution of species among solution-phase equilibria.

Table 5-2. Calculated energy for selected chemical equilibria of reduced sulfur species.

Reaction	Energy (eV)
Disproportionations	
(5) $4\ S_8^{2-} \rightarrow 4\ S_6^{2-} + S_8$	+0.18
(9) $S_4^{2-} + S_8^{2-} \rightarrow 2\ S_6^{2-}$	**-0.17**
(11) $S_6^{2-} + 2\ S_3^{2-} \rightarrow 3\ S_4^{2-}$	**-0.35**
(20) $S_8^{2-} + S_{8,c} \rightarrow S_x^- + S_y^-$	+0.66 (x = 10) +0.69 (x = 9) +0.43 (x = 8) (***19***)
(24) $S_5^{2-} + S_8^{2-} \rightarrow S_7^{2-} + S_6^{2-}$	**-0.07**
(27) $2\ S_8^{2-} \rightarrow S_7^{2-} + S_9^{2-}$	+0.16
Dissociations	
(15) $S_{8,c}^- \rightarrow S_{8,l}^-$	+0.30
(12) $S_6^{2-} \rightarrow 2\ S_3^-$	**-0.27**
(21) $S_8^{2-} \rightarrow S_x^- + S_y^-$	+0.64 (x = 6) +0.21 (x = 5) (***22***) +0.25 (x = 4) (***17***)
(25) $S_7^{2-} \rightarrow S_4^- + S_3^-$	-0.04
$S_9^{2-} \rightarrow S_6^- + S_3^-$	+0.16

Interestingly, even if the reactions forming radical anions are thermodynamically unfavorable, the electrochemical reduction of S_x^- would drive them forward via LeChatelier's principle. The forward rate for the unimolecular dissociations have not been directly measured, although the electrochemical data of Lelieur et al. are fit with forward rates ranging from 80-1000 s^{-1} for reactions 17 and 12, respectively. It is

reasonable that, for a reaction involving cleavage of a given bond, the unimolecular dissociation would have faster forward rates than the bimolecular comproportionation because there is no requirement for intermolecular collision; however, the relative contribution from each class of reaction would be determined by the experimental conditions (e.g. temperature and concentration).

For electroanalytical conditions, the unimolecular dissocation forming S_5^- is particularly interesting as a possible explanation of both the additional current observed after the reduction of S_8 and a direct route to form the electroactive S_3^- species.

$$S_{8,l}^{2-} \leftrightarrow S_5^- + S_3^- \quad (22)$$

$$S_5^- + e^- \rightarrow S_5^{2-} \quad (23)$$

$$S_{8,l}^{2-} + S_5^{2-} \leftrightarrow S_7^{2-} + S_6^{2-} \quad (24)$$

$$S_6^{2-} \leftrightarrow 2S_3^- \quad (12)$$

$$S_7^{2-} \leftrightarrow S_3^- + S_4^- \quad (25)$$

The simplicity of this reaction step makes it a reasonable explanation for at least a fraction of the S_3^- reduction wave observed in electroanalytical studies.

The predicted reduction potentials are also consistent with two distinct reduction processes in the electroanalytical studies. Although the longer polysulfides extend over a range of potentials, S_3^- and S_2^- are reduced close to the same potential. Clearly, additional characterization techniques are required to discriminate between reduction of the shortest sulfur anions. The QC results also strongly suggest that the second reduction process is not due to reduction of the dianions.[18,23] For example, reduction of S_6^{2-} to S_6^{3-} is predicted to occur over 100 mV more negative than S_3^-. If this electrochemical process occurs, it must be a minor contribution to the current after the reduction peak of S_3^-.

Finally, the QC results can be used to evaluate alternate reaction pathways that appear

reasonable but have not been considered in the electrochemical literature. For example, linear S_8^{2-} has been reported to rapidly disproportionate to adjacent polysulfides:[44]

$$2S_8^{2-} \leftrightarrow S_7^{2-} + S_9^{2-} \quad (27)$$

The dissociation of both S_7^{2-} and S_9^{2-} into radical anions is more energetically favorable than the dissociation of S_8^{2-}. With additional data on the barriers and thus rates of disproportionation is should be possible to evaluate how much this pathway contributes to the electrochemical response.

5-4. Rationalization of Li-S Cell Discharge

Having a rough outline of the sulfur reduction mechanism under electroanalytical conditions, it is interesting to see how well the mechanism explains the electrochemistry for prototype lithium-sulfur batteries. Typically, battery cells can be used to obtain chronopotentiometric and coulometric data on electrochemical systems. However, as discussed in chapter 7, the solubility of sulfur species in battery solvents prevents quantitative analysis of the electrochemical response. For example, soluble sulfur species can dissolve into excess electrolyte in the cell, changing the electroactive mass for coulometry normalization, or mediate charge transfer from the anode, artificially shortening the time required for sulfur reduction.

Figure 5-7 shows an exemplary voltage profile during a slow (12 hour) discharge of a lithium-sulfur battery. In agreement with the CV and RDE results, two distinct electrochemical features are observed with potentials that match reasonably well with the reduction waves under electroanalytical conditions. The length of the first voltage plateau is corresponds to nearly a full 2 e^-/S_8, as expected for the formation of S_8^{2-}. However, as predicted from the results of sections 5-1 and 5-2, there is also a reasonable amount of charge (~1 e^-/S_8) passed between the two voltage plateaus. An inflection in the profile near 2.2 V indicates the presence of a distinct reduction

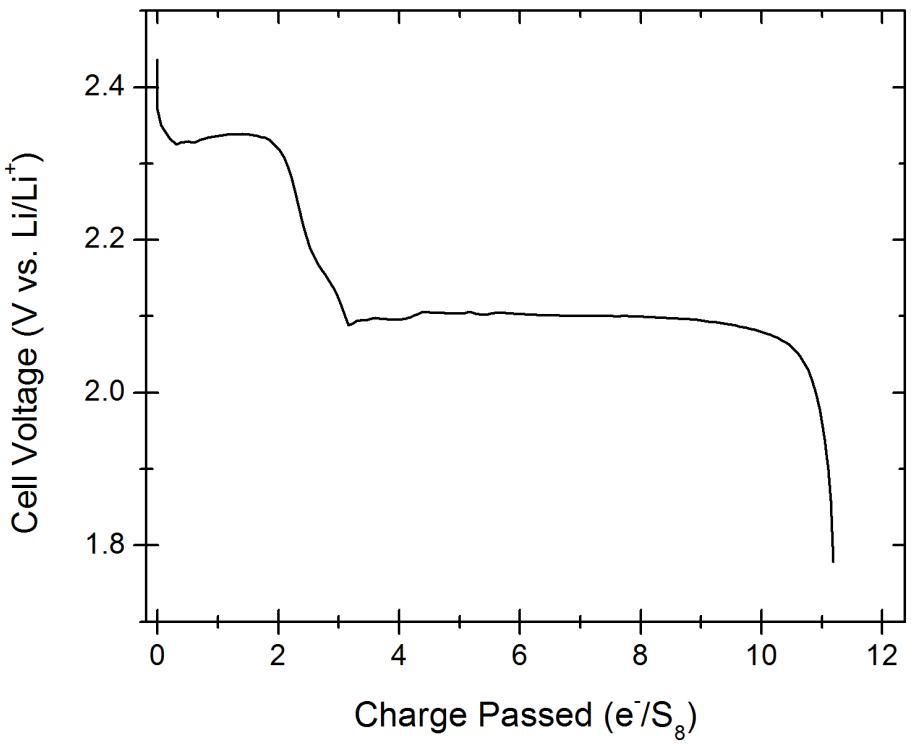

Figure 5-7. Voltage profile during discharge of lithium-sulfur coin cell. Applied rate 100 mA/g-sulfur; electrolyte solution 1 M LiTFSI in tetra(ethyleneglycol) dimethyl ether.

species, probably S_4^-, such as would be formed by reaction 17**.**

The similarities between the reduction of sulfur in electroanalytical and battery conditions implies that the mechanism is the same under both conditions, even though the drastic differences in sulfur concentration and applied rate change the relative importance of specific reactions. Of critical importance is that at least the initial phases of reduction are mediated by solution-phase sulfur species. This conclusion means that any practical lithium-sulfur cell will have to address the high solubility of long-chain polysulfides to prevent loss of active material into solution.

Unlike in electroanalytical conditions, though, there is much more charge passed in the second reduction process on the battery time scale. This is desireable for device

applications, but unfortunately the key mechanistic steps cannot be explained using the approach of this chapter. Electroanalytical studies did show that the charge passed in this voltage regime depends on the applied rate, but none of the techniques were able to probe the process(es) occurring on the time scale of multiple hours. The best option, coulometry with chronopotentiometry, is inappropriate using coin cell geometries, but will be discussed in more detail in chapter 7.

5-5. Conclusions

The reduction of sulfur in lithium-containing aprotic solvents is exceptionally complex, with several possible reduction pathways. Electroanalytical approaches are able to establish that the first processes are a reduction of cyclic S_8 to the radical S_8-, which then undergoes a chemical step prior to reduction to the linear S_8^{2-}. The S_8^{2-} dianion can then disproportionate or dissociate to form additional electroactive species that can be reduced at close to the same potential, within the first reduction wave, and the shorter electroactive radical anions, such as S_3^{-}, that are reduced in the second reduction wave. QC computational results support the presence of multiple sulfur species that can be reduced at or close to the first reduction wave, and this model can be used to rationalize the voltage profile of a lithium-sulfur battery discharge. Unfortunately, the widely varying solubility and slow reactions of reduced sulfur species complicates the electroanalytical interrogation of chemical steps occurring during the second reduction wave, and these processes will be best studied using a new electrochemical cell format.

REFERENCES

(1) Gao, J.; Lowe, M. A.; Kiya, Y.; Abruna, H. D. *The Journal of Physical Chemistry C* **2011**.

(2) Jayaprakash, N.; Shen, J.; Moganty, S. S.; Corona, A.; Archer, L. A. *Angew. Chem. Int. Ed.* **2011**, *50*, 1–6.

(3) Ji, X.; Evers, S.; Black, R.; Nazar, L. F. *Nature Communications* **2011**, *2*, 325.

(4) Ji, X.; Lee, K. T.; Nazar, L. F. *Nat. Mater.* **2009**, *8*, 500–506.

(5) Ji, L.; Rao, M.; Aloni, S.; Wang, L.; Cairns, E. J.; Zhang, Y. *Energy & Environmental Science* **2011**, *4*, 5053.

(6) Liang, X.; Wen, Z.; Liu, Y.; Zhang, H.; Huang, L.; Jin, J. *J. Power Sources* **2011**, *196*, 3655–3658.

(7) Cao, Y.; Li, X.; Aksay, I. A.; Lemmon, J.; Nie, Z.; Yang, Z.; Liu, J. *Phys. Chem. Chem. Phys.* **2011**, *13*, 7660.

(8) Liang, C.; Dudney, N. J.; Howe, J. Y. *Chem. Mater.* **2009**, *21*, 4724–4730.

(9) Wang, H.; Yang, Y.; Liang, Y.; Robinson, J. T.; Li, Y.; Jackson, A.; Cui, Y.; Dai, H. *Nano Lett.* **2011**.

(10) Li, X.; Cao, Y.; Qi, W.; Saraf, L. V.; Xiao, J.; Nie, Z.; Mietek, J.; Zhang, J.-G.; Schwenzer, B.; Liu, J. *J. Mater. Chem.* **2011**, *21*, 16603.

(11) Cheon, S.-E.; Choi, S.-S.; Han, J.-S.; Choi, Y.-S.; Jung, B.-H.; Lim, H. S. *J. Electrochem. Soc.* **2004**, *151*, A2067–A2073.

(12) Meyer, B. *Chem. Rev.* **1976**, *76*, 367–388.

(13) Merritt, M. V.; Sawyer, D. T. *Inorg. Chem.* **1970**, *9*, 211–215.

(14) Bonnaterre, R.; Cauquis, G. *J. Chem. Soc., Chem. Commun.* **1972**, 293.

(15) Delamar, M.; Marchon, J. C. *Journal of Electroanalytical Chemistry and Interfacial Electrochemistry* **1975**, *63*, 351–357.

(16) Delamar, M. *Journal of Electroanalytical Chemistry and Interfacial Electrochemistry* **1975**, *63*, 339–349.

(17) Paris, J.; Plichon, V. *Electrochim. Acta* **1981**, *26*, 1823–1829.

(18) Gaillard, F.; Levillain, E.; Lelieur, J. P. *J. Electroanal. Chem.* **1997**, *432*, 129–138.

(19) Levillain, E.; Gaillard, F.; Leghie, P.; Demortier, A.; Lelieur, J. *J. Electroanal. Chem.* **1997**, *420*, 167–177.

(20) Levillain, E.; Gaillard, F.; Lelieur, J. P. *J. Electroanal. Chem.* **1997**, *440*, 243–250.

(21) Levillain, E.; Demortier, A.; Lelieur, J. P. *J. Electroanal. Chem.* **1995**, *394*, 205–210.

(22) Leghie, P.; Lelieur, J.-P.; Levillain, E. *Electrochem. Commun.* **2002**, *4*, 406–411.

(23) Martin, R. P.; Doub Jr, W. H.; Roberts Jr, J. L.; Sawyer, D. T. *Inorg. Chem.* **1973**, *12*, 1921–1925.

(24) Wong, M. W. *Topic in Current Chemistry* **2003**, 193–198.

(25) Han, D.-H.; Kim, B.-S.; Choi, S.-J.; Jung, Y.; Kwak, J.; Park, S.-M. *J. Electrochem. Soc.* **2004**, *151*, E283.

(26) Jung, Y.; Kim, S.; Kim, B.-S.; Han, D.-H.; Park, S.-M.; Kwak, J. *Int. J. Electrochem. Sci.* **2008**, *3*, 566–577.

(27) Yamin, H.; Gorenshtein, A.; Penciner, J.; Sternberg, Y.; Peled, E. *J. Electrochem. Soc.* **1988**, *135*, 1045–1048.

(28) Evans, A.; Montenegro, M. I.; Pletcher, D. *Electrochem. Commun.* **2001**, *3*, 514–518.

(29) Dominko, R.; Demir-Cakan, R.; Morcrette, M.; Tarascon, J.-M. *Electrochem. Commun.* **2011**, *13*, 117–120.

(30) Park, J.; Chang, B.; Yoo, J.; Hong, S.; Park, S. *BULLETIN-KOREAN CHEMICAL SOCIETY* **2007**, *28*, 1523.

(31) Kolosnitsyn, V. S.; Kuzmina, E. V.; Karaseva, E. V.; Mochalov, S. E. *J. Power Sources* **2011**, *196*, 1478–1482.

(32) Yuan, L.; Qiu, X.; Chen, L.; Zhu, W. *J. Power Sources* **2009**, *189*, 127–132.

(33) Bard, A. J.; Faulkner, L. R. *Electrochemical Methods: Fundamentals and Applications*; 2nd ed.; John Wiley & Sons, Inc., 2001.

(34) Budevski, E.; Staikov, G.; Lorenz, W. J. *Electrochim. Acta* **2000**, *45*, 2559–2574.

(35) Galvez, J.; Alcaraz, M. L.; Vera, J. *Anal. Chem.* **1994**, *66*, 2935–2942.

(36) Alberts, G. S.; Shain, I. *Anal. Chem.* **1963**, *35*, 1859–1866.

(37) Winget, P.; Cramer, C. J.; Truhlar, D. G. *Theor. Chem. Acc.* **2004**, *112*.

(38) Burkhardt, S. E.; Lowe, M. A.; Conte, S.; Zhou, W.; Qian, H.; Rodríguez-Calero, G. G.; Gao, J.; Hennig, R. G.; Abruña, H. D. *Energy & Environmental Science* **2012**, *5*, 7176.

(39) Schmidt am Busch, M.; Knapp, E.-W. *J. Am. Chem. Soc.* **2005**, *127*, 15730–15737.

(40) Rodríguez-Calero, G. G.; Lowe, M. A.; Kiya, Y.; Abruña, H. D. *The Journal of Physical Chemistry C* **2010**, *114*, 6169–6176.

(41) Rauh, R. D.; Shuker, F. S.; Marston, J. M.; Brummer, S. B. *J. Inorg. Nucl. Chem.* **1977**, *39*, 1761–1766.

(42) Raghavachari, K.; Rohlfing, C. M.; Binkley, J. S. *J. Chem. Phys.* **1990**, *93*, 5862.

(43) Kao, J.; Allinger, N. L. *Inorg. Chem.* **1977**, *16*, 35–41.

(44) Steudel, R. *Top. Curr. Chem.* **2003**, 127–152.

CHAPTER 6

MECHANISTIC INSIGHTS INTO OPERATIONAL LITHIUM-SULFUR BATTERIES BY IN-SITU X-RAY DIFFRACTION AND ABSORPTION SPECTROSCOPY

6-1. Introduction

Electrochemical energy storage often involves a tradeoff between chemical complexity and theoretical capacity. Current lithium-ion battery cathodes store charge via ion intercalation into crystalline structures, resulting in a theoretical capacity limited by the mass of the crystalline host (e.g. CoO_2, $FePO_4$) and, in general, no more than one electron is stored per formula unit. In addition, the practical capacities reached in devices is often well below theoretical values. On the other hand, the most promising chemical systems for future energy storage involve reactions between lithium and molecules of electronegative elements (e.g. S_8, O_2) that can access multiple electrons per formula unit, promising dramatic gains in capacity (~10X that of existing lithium-ion batteries) albeit at the cost of increased mechanistic complexity and chemical changes during the reaction. The increased chemical complexity that comes with a shift towards molecular charge storage portends a need for new and chemically-informed approaches to battery design, testing, and characterization.

The lithium-sulfur system is especially attractive and promising due to the combination of sulfur's reduction potential (>2V vs. Li/Li^+), extraordinary theoretical gravimetric capacity (16 electrons per S_8, or 1,672 mAh/g), and condensed phase. However, its full theoretical capacity has not yet been accessed reversibly due to the complex chemistry and mechanistic interplay between lithium and polysulfides. While various mechanisms for sulfur reduction have been proposed based on parameterized

models,[1] electrochemical probes within batteries,[2–4] or electroanalytical studies,[5–7] the diversity of possible reactions, combined with the paucity of data on specific intermediates, means that many of the proposed mechanisms are speculative and inconsistent. Additional experimental data, especially under realistic battery operating conditions, about reduced sulfur species are necessary to resolve previous analytical and battery-level studies and provide rational guidelines for approaching the full capacity from the lithium-sulfur system.

The complexity of the sulfur mechanism has been the subject of a number of analytical studies,[6–9] although most have pursued the reaction mechanism in solvents that are not appropriate for lithium batteries (e.g. N,N-dimethylformamide; DMF)[6,10,11] and at much lower, electroanalytical concentrations.[6,8,10,12–14] These *in-situ* spectroelectrochemical studies support the following outline of the sulfur reduction mechanism; at least at low sulfur concentrations:[7]

- Elemental sulfur is initially reduced to form S_8^- and then S_8^{2-}
- S_8^{2-} rapidly equilibrates to yield several different polysulfides (S_n^{2-}), including S_6^{2-}
- S_8^{2-} and S_6^{2-} dissociate to form S_4^- and S_3^-, respectively, with S_3^- as the predominant species
- Only the radical anions S_3^- and S_4^- are subsequently reduced in a second electrochemical process. Depending on the solvent, this process is 300-800 mV more negative than the first reduction process.[15]

The dissociative equilibria between and among polysulfides and the electrochemically active radical anions[8,9] emphasize the need for studies under technologically-relevant conditions of solvent, electrolyte and concentrations. Moreover, the research at electroanalytical concentrations has not probed the appearance of fully-reduced

lithium sulfide, which, as the final reduction product, is of utmost importance for lithium-sulfur batteries.

On the other hand, researchers studying lithium-sulfur batteries have proposed various mechanisms, albeit without *in-situ* diffraction or spectroscopy data, which agree that sparingly soluble elemental sulfur is first reduced to soluble polysulfides (S_n^{2-}, n>2) and subsequently to insoluble lower polysulfides (Li_2S_2 or Li_2S)**.**[16–21] While the first step is in general agreement with electroanalytical studies, the second reaction is inferred from observed cell capacities,[16] electrochemical impedance measurements[4] and ex-situ diffraction.[3,22] Inadequate experimental data on sulfur reduction products are a major obstacle to further understand and control the failure modes of lithium-sulfur cells. For example, insoluble Li_2S_2 has been proposed to be a major discharge product and the cause of poor cyclability (i.e. rapid capacity fade) [16,17,20,21,23] even though there are no reports of its direct observation. Mechanistically, it is still unclear whether the reduction of polysulfides occurs sequentially[1] (i.e. higher polysulfides are reduced before lower polysulfides) or concurrently,[24] and the relative importance of mediated reductions[25] (e.g. disproportionations) and direct electrochemical reduction.[24]

The lack of data on reduced sulfur species in lithium-sulfur batteries derives, in large part, from the difficulty of characterizing the air-sensitive ensemble of partially-soluble, partially-reduced, and partially-crystalline sulfur species within the concentration and volumetric constraints of typical prototype cells. While the complexity of the system is imposing, x-ray diffraction and absorption spectroscopy can provide the respective phase and elemental specificity to resolve both crystalline and chemical changes during cell charge/discharge cycles. Moreover, the relatively weak interaction of high energy photons with matter (i.e., high penetration depth) means that these techniques can provide a bulk-sensitive response from sulfur within

sealed batteries.

Herein, we present in-situ XRD and sulfur K-edge XANES results from the first discharge/charge cycle of operational lithium-sulfur batteries. Both techniques have previously been demonstrated for other battery systems,[26,27] but surprisingly, this is the first study that applies both to sulfur cathodes. To the best of our knowledge, there are no reports of in-situ sulfur K-edge XANES for sulfur cathodes, while there are two previous reports of in-situ XRD for the lithium-sulfur system. Both used pouch-type cells, and both had electrochemical responses that appeared significantly different than typical reports for the sulfur system.[28,29] The most recent also reported an inconsistency between in-situ and ex-situ studies of their sulfur cathodes, with crystalline Li_2S only apparent in the ex-situ studies. While this could be due to a slow crystallization process, as the authors propose, the resistive electrochemical response and the difficulty in ensuring adequate internal contact within pouch cells at least raises questions of whether the x-rays probed a representative region of the cathode.[29]

This study uses in-situ cells constructed by simple modifications to standard 2032 coin cells, a popular format for testing lithium-sulfur batteries. The well-defined geometry ensures good contact and more representative electrochemical response. The electrochemical features are correlated with time-dependent XRD from the crystalline end products, and XANES from all sulfur species present in the battery. Together, the data show that the reduction of sulfur to lithium sulfide proceeds primarily through disproportionations of polysulfides, with specific sulfur species playing a dominant role in the overall mechanism.

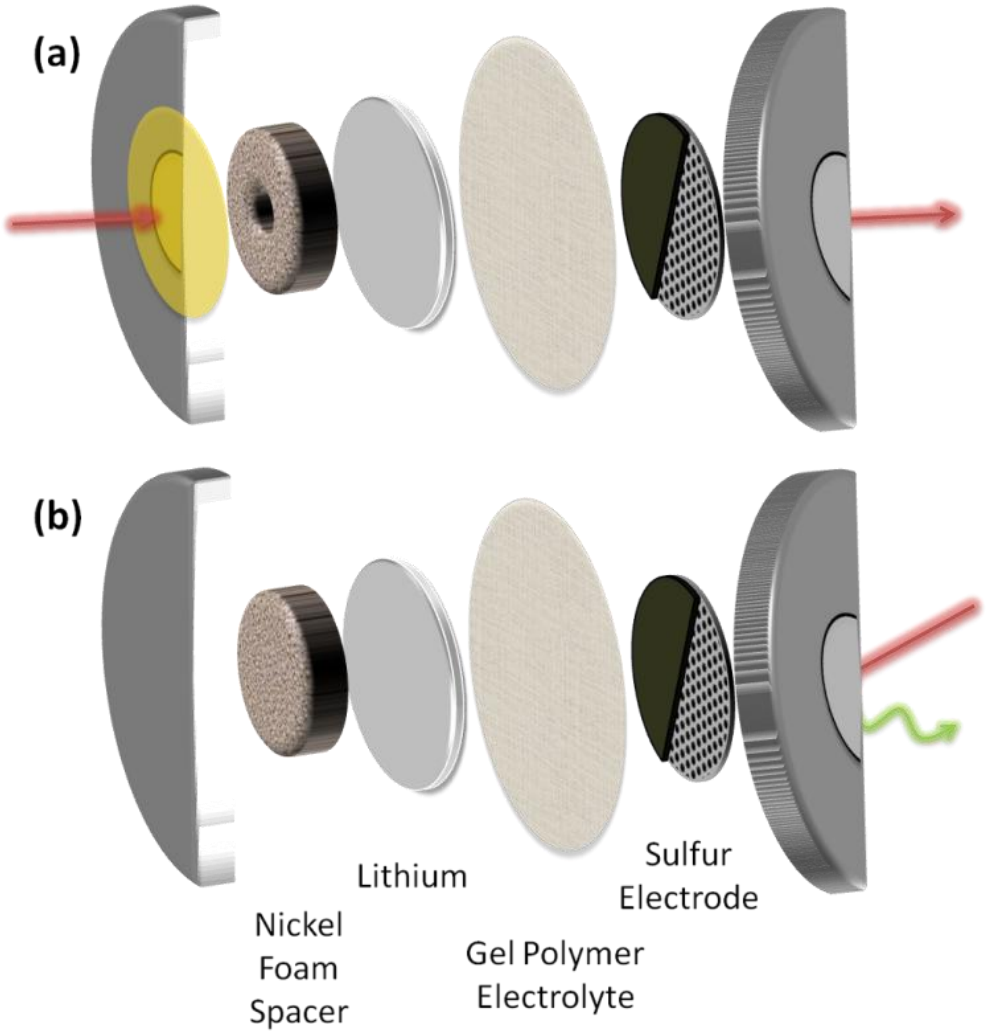

Figure 6-1. Modified coin cells and scattering geometries for in-situ x-ray studies of lithium sulfur batteries. (a) Cell designed for XRD in transmission geometry. (b) Cell designed for sulfur K-edge XAS with fluorescence detection.

6-2. Methods

VI.a. Battery Preparation

A sulfur-carbon composite was prepared by physically mixing elemental sulfur and carbon black (50:45 by mass), transferring the mixture into a Teflon-lined steel

autoclave, and heating for 10 h at 155 °C. Elemental sulfur electrodes were prepared by grinding the sulfur-impregnated carbon black composite and polyvinylene difluoride (PVDF) (95:5 wt.%) with N-methyl-pyrrolidone in a mortar and pestle and spreading the slurry with a doctor's blade. The film was then dried in vacuum for 12 hours, weighed, and stored in an argon-filled glovebox until use. For this work, films were cast on a carbon-coated aluminum mesh current collector to minimize attenuation of the lower-energy x-rays necessary for x-ray absorption spectroscopy at the sulfur K edge. Typical sulfur loadings were 1-2 mg/cm^2.

Prototype lithium-sulfur cells were fabricated using modified CR2032 coin cell casings. 3 mm diameter holes were drilled through the casings, and kapton windows were epoxied around the holes (Figure 6-1). For XRD measurements, 100 µm-thick windows were used on both anode and cathode casings to minimize atmospheric contamination (Figure 6-1a), while the XANES study used an unmodified anode casing and a 8 µm thick kapton window on only the cathode casing to minimize photon attenuation at the sulfur K-edge (2472 eV) (Figure 6-1b). A 70 nm-thick film of aluminum was deposited on both sides of all kapton windows to reduce air and moisture diffusion through the windows while providing good electrical contact.

Cells were prepared using lithium anodes and a film of poly(vinylidene fluoride-co-hexafluoropropene) (PVDF-HFP) saturated with 1 M $LiClO_4$ in tetra(ethylene glycol) dimethyl ether as a gel polymer electrolyte. The PVDF-HFP film was prepared as previously reported by Tarascon et al.[30] All cells were stored in hermetically-sealed, argon-filled vials until probed using synchrotron x-ray radiation, and characterized within 4 days of preparation to prevent significant self-discharge.

VI.b. X-Ray Measurements

Diffraction data were acquired in a transmission geometry with 30 keV incident radiation at beamline A2 of the Cornell High Energy Synchrotron Source

(CHESS). Diffraction was collected using a 2D detector (GE), then integrated to obtain 1D diffraction patterns using Fit2D.[31]

XAS spectra were collected at beamline X19A of the National Synchrotron Light Source (NSLS). Batteries were cycled in a He-purged sample chamber, with x-ray fluorescence detected using a large area passivated implanted planar silicon detector (Canberra Industries, Inc.). Datasets were background subtracted and normalized using the Athena software package.[32] Care was taken to limit the duration of x-ray exposure to less than 10% of the battery operation, since extended irradiation of the battery at energies above the absorption edge was found to alter the electrochemical and spectroscopic response. This is a consequence of irradiating electronically isolated (solvated) sulfur species in solution, since no spectroscopic evidence for radiation damage was found using solid-phase standards (elemental sulfur or lithium sulfide) or ex-situ electrodes.

6.3 In-Situ X-ray Diffraction

In contrast to other chalcogen-alkali metal phase diagrams, the only crystalline phases in the lithium-sulfur system are the several allotropes of elemental sulfur (S_8) and the fully reduced cubic lithium sulfide (Li_2S).[33,34] This limits diffraction to inferring mechanistic information based on the appearance of the reaction end points. However, this limited information is still valuable since the appearance of Li_2S should be different for many of the reaction mechanisms proposed in the literature. Table 6-1 summarizes the expected appearance of Li_2S with four proposed polysulfide reduction mechanisms. It is notable that most of the mechanisms require Li_2S to appear near a specific state of charge. For example, the sequential reduction of long to short-chain polysulfides[35] should result in Li_2S appearing only at the end of the discharge, after passing ~1 e^- per sulfur atom. The exception is the reduction mechanism based on spectroelectrochemical studies at low concentrations. This mechanism proposes that

Li_2S is formed by chemical equilibria among reduced sulfur species, and it is probable that these equilibria are influenced by local sulfide concentrations and solubilities.

Table 6-1. Predicted trends in the appearance of Li_2S for proposed polysulfide reduction mechanisms

Number	Reaction	Reference	Appearance of Li_2S
1	$S_8^{2-} \rightarrow S_4^{2-} \rightarrow Li_2S_{2,Solid} \rightarrow Li_2S_{Soli}$	[35]	End of discharge, near 800 mAh/g
2	$S_8^{2-} \rightarrow S_7^{2-} + Li_2S_{Solid} \rightarrow \cdots$ $\rightarrow S_2^{2-} + Li_2S_{Solid} \rightarrow 2Li_2S_{Solid}$	[24]	End of first plateau and formation of S_8^{2-}, near 210 mAh/g
3	$S_8^{2-} \rightarrow S_6^{2-} \rightarrow S_4^{2-} \rightarrow S_2^{2-} \rightarrow Li_2S_{Solid}$ Simultaneous reduction of S_4^{2-} and S_2^{2-}	[1]	Beginning of 2nd plateau, near 330 mAh/g
4	$S_8^{2-} \leftrightarrow S_4^{-} + S_3^{-} \rightarrow S_4^{2-} + S_3^{2-} \leftrightarrow Li_2S$	[7], [25]	After formation of S_4^{2-}, near 420 mAh/g or S_3^{2-}, near 556 mAh/g

Reaction mechanism key: double arrows (↔) indicate chemical steps, single arrows (→) are direct electrochemical reduction steps.

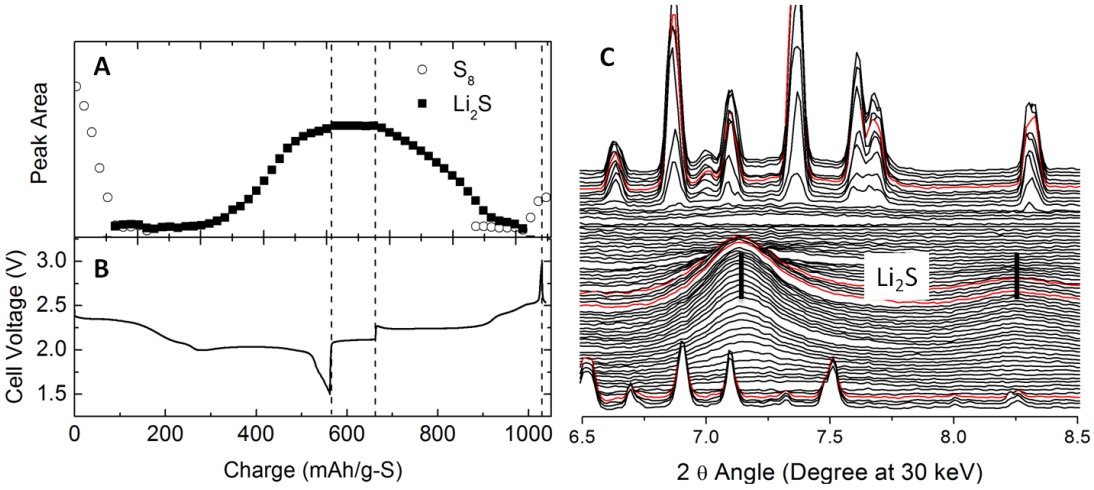

Figure 6-2. In-situ XRD data for lithium sulfur battery with liquid electrolyte. (A) Peak area integrated over 6.7-7.7° for S_8 (open circles) and 6.9-7.3° for Li_2S (closed squares). Vertical dashed lines indicate beginning and end of galvanostatic cycling. (B) Cell voltage during cycling, at rate of 100 mA/g-S. (c) Waterfall plot of data during cycling. Black vertical lines indicate expected positions for Li_2S.

Figure 6-2 presents typical diffraction data during the first galvanostatic discharge/charge cycle of an operational lithium-sulfur battery prepared with liquid electrolyte. As seen in Figures 6-2A and 6-2B, the integrated diffraction intensity from orthorhombic elemental sulfur linearly decreases with discharge time. By midway through the first discharge plateau, all crystallinity disappeared, consistent with the proposed reduction of elemental sulfur to an amorphous polysulfide. Significantly, diffraction from Li_2S is detected near the beginning of the second discharge plateau. This is in agreement with some ex-situ studies of partially-discharged sulfur cathodes, [3,36] although, as discussed above, the study of ex-situ sulfur cathodes is fraught with uncertainty. As seen in Figure 6-2C, the average Li_2S domain is significantly smaller than the average elemental sulfur domain (7 nm vs. >60 nm, respectively, as determined from the Scherrer equation), suggestive of nucleation and precipitation of Li_2S nanoparticles from solution. The Li_2S diffraction signal grows until the end of discharge, remains nearly constant during an open circuit equilibration at the end of

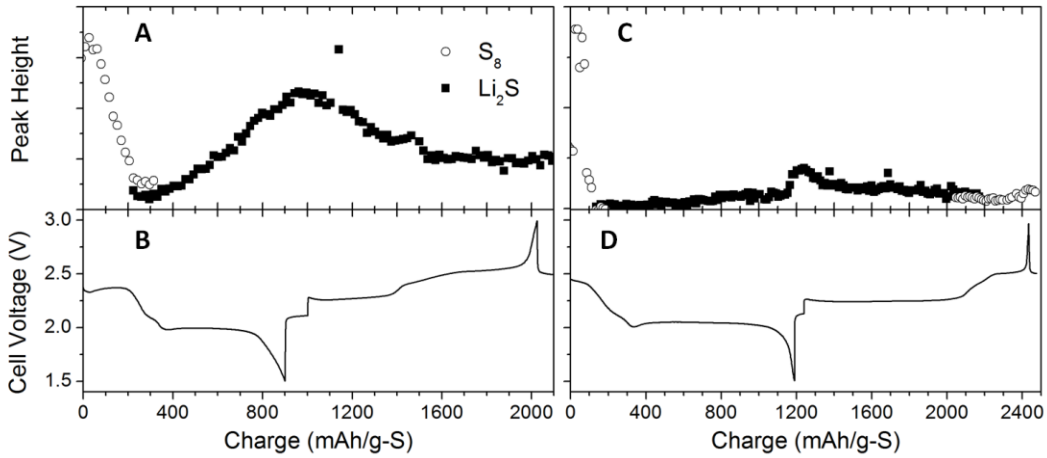

Figure 6-3. Diffraction from sulfur cathodes with different electrolytes. (A) and (B) are for a sulfur cathode with liquid electrolyte. (C) and (D) are for a sulfur cathode with a gel polymer electrolyte. (A, C) Peak area integrated over 6.7-7.7° for S_8 (open circles) and 6.9-7.3° for Li_2S (closed squares). (B, D) Cell voltage during cycling, at rate of 100 mA/g-S.

the discharge, and then disappears by the end of the first recharge plateau. At the end of the final plateau, elemental sulfur is formed, crystallizing in the monoclinic structure (Figure 6-1C). Although orthorhombic sulfur is thermodynamically favored, previous researchers have reported precipitation of monoclinic sulfur nanoparticles at room temperature.[37]

The diffraction for a sulfur cathode in liquid electrolyte indicates that approximately 300 mAh/g-S of charge is passed before the appearance of Li_2S. This also coincides with the beginning of the second plateau. Comparison of these results with Table 6-1 suggests that the most probable reaction mechanism involves the simultaneous reduction of S_4^{2-} and S_2^{2-}. However, additional experiments with sulfur cathodes raises questions about this conclusion. Figure 6-3 shows in-operando diffraction results for cathodes made from thermally-mixed composites of sulfur and carbon black. Thermal mixing generally results in improved electrochemical performance, with the improvements generally ascribed to the improved electrical contact with sulfur. Comparison of the discharge capacities (Figures 6-2B, 6-3B and

6-3D) confirm that this trend is also observed in the current samples. Interestingly, the x-ray diffraction results show that Li_2S appears later for the thermally-mixed samples than for the physically-mixed cathode (Figure 6-2). The delay is slight (~100 mAh/g) for the cathode in liquid electrolyte, but dramatic for the cathode in the gel polymer electrolyte (~800 mAh/g). The only reaction mechanism that could account for a varying onset of Li_2S is mechanism 3, in which chemical equilibria are responsible to form Li_2S. It is likely that the thermally-mixed sulfur and carbon has less dissolution of sulfur into the electrolyte solution, changing both local concentrations and where the chemical equilibria occur.

Unfortunately, the XRD results cannot unambiguously confirm the reaction mechanism because of the possibility that amorphous Li_2S is one of the end products. Since XRD is strictly sensitive to the crystalline species, the conclusions will be biased if the reaction forms amorphous Li_2S on a different time scale or via a different reaction pathway. At least some amorphous Li_2S is formed in these reactions, since crystalline Li_2S does not appear until well after 800 mAh/g for the cathode in the gel polymer electrolyte. (Figure 6-3C) The intensity of diffraction from Li_2S also significantly decreases for the cathode in the gel polymer electrolyte, even though more charge is passed into the cell.

While the XRD cannot prove the operative reaction mechanism, it can conclusively eliminate reaction 1 (formation of Li_2S at the end of discharge) and seems to suggest that the reaction mechanism is dependent on the local concentration of sulfur species near the cathode. Another significant point is that the cell performance is best under conditions in which Li_2S is not formed. This result suggests that other, non-phase-specific techniques may be better suited to probe the chemistry of the sulfur reduction reaction.

6-4. In-Situ X-ray Absorption

There are limited reports of XAS from polysulfides in solution or in the solid state, due to the competing constraints of the 'tender' incident x-ray energy of the sulfur K edge and the air-sensitivity of polysulfides, especially Li_2S. Thus, significant attention to cell design was required for the sulfur XANES research. Cells made with electrolyte solution trapped a thin (~200 micron) layer of solvent between the electrode and the window material. This quantity of solution was sufficient to completely attenuate the incoming x-rays before reaching the electrode, making the technique sensitive only to those species in solution. Thus, a study of sulfur species within the cathode was only possible for the sulfur cathode with a gel polymer electrolyte.

An additional complication is the lack of single-phase polysulfide standards between elemental sulfur and lithium sulfide, since a reasonable solution of any single polysulfide S_n^{2-} will rapidly equilibrate into several adjacent polysulfides S_{n-1}^{2-} and S_{n+1}^{2-}.[5] Thus, an in-situ study of sulfur reduction species is required to obtain truly representative and relevant data on the system.

Figure 6-4A presents a complete XAS dataset for the discharge and charge of a lithium-sulfur battery with a gel polymer electrolyte. The apparent symmetry of the dataset emphasizes that discharging and charging proceed through a reversible sequence of reactions. Several distinct features evolve through the cycle and are emphasized in the selected spectra shown in Figure 6-4B. The relative peak intensities, as indicated by the derivative of the spectra, are plotted in Figure 6-4C to correlate XAS and electrochemical features. Below we discuss the trends and propose tentative assignments to various sulfur species.

In the charged state, the spectrum from the sulfur cathode matches that of elemental sulfur (Figure 6-4B). At the start of the discharge, there is a distinct increase

in the main peak intensity (red data in Figure 6-4C) due to the formation of long-chain polysulfides (S_n^{2-}, n>7)[38] Under electroanalytical conditions, cyclic S_8 is reduced by two electrons to form an S_8^{2-} chain at potentials, versus lithium, that are very similar to the voltage of the first discharge plateau. [7] It is expected that disproportionation reactions will rapidly give rise to a distribution of long-chain polysulfides [39] which have XANES signals that are too similar for spectroscopic speciation/differentiation.

At the end of the first voltage plateau, the intensity of the first peak decreases and a new pre-peak appears (2.31 V spectrum in Figure 6-2b and black data in Figure 6-4C). A similarly-downshifted peak has been reported from solid-state compounds and assigned to the 1s-3p(π*) transition for S_3^- radical anions.[40] The spectra, in the first part of the transition period, show two clear isosbestic points at 2472.2 and 2475.5 eV, consistent with a simple conversion between two species. Thus, we propose that the pre-peak is from S_3^- radical anions formed by dissociation of longer-chain polysulfides. Sulfur electrochemical data have indicated that these equilibria are fast and favor radical anion formation.[10] The appearance of S_3^- is also consistent with several spectroelectrochemical studies at electroanalytical concentrations.[10–12] This assignment is also supported by the in-situ Raman results presented in Chapter 4.

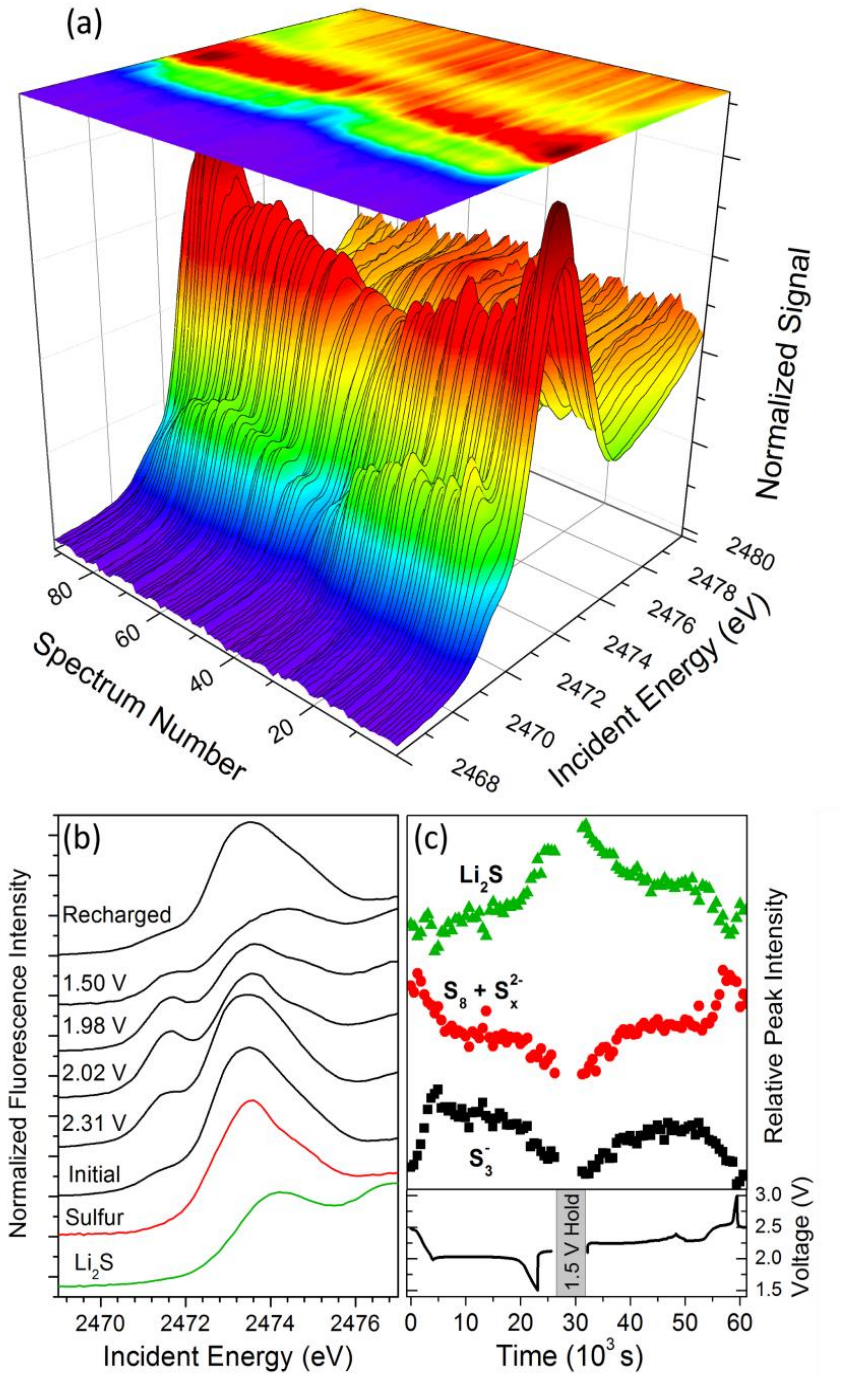

Figure 6-4. XAS data for a lithium sulfur battery with a gel polymer electrolyte. (a) Waterfall plot of dataset for a full galvanostatic cycle. (b) Spectra selected from specific points during the cycle. (c) Variation of fluorescence signal and cell voltage as a function of charge. Data points correspond to the intensity of the first derivative of each spectrum at 2471.1 eV (pre-peak, black), 2472.6 eV (main peak, red), and 2473.9 eV (Li_2S, green).

As the cell voltage continues to decrease to the second plateau, the main peak also shifts to slightly higher energies (2.02 V spectrum in Figure 6-4B). We propose that this shift is related to a decrease in the average polysulfide chain length (i.e. disproportionations to form S_x^{2-}, $4<x<8$). Charge is more localized for shorter polysulfides, which permits more effective screening by lithium counter-ions and a hypsochromic shift in the position of the main peak. For example, the main peak in the sulfur XANES of lithium sulfide is shifted nearly a full eV to higher energy relative to elemental sulfur (Figure 6-4B).

Through the lower voltage plateau, the spectra are dominated by the pre-peak and the shifted main peak (2.02 and 1.98 V spectra in Figure 6-4B). The invariance in the peak positions suggests that they are due to a specific set of sulfur species, such as S_3^- and S_4^{2-}. Raman spectroscopy suggests that both species are present in a discharged sulfur cathode. (Chapter 4) Both peak intensities slowly diminish in amplitude during the voltage plateau (Figure 6-4C) as S_3^- and, by equilibration, S_4^{2-} are electrochemically reduced and consumed. This is consistent with previous electroanalytical reports that have shown that the second (more negative) electrochemical process is due to the S_3^-/S_3^{2-} couple.[10,15] It is notable that the same two peaks persist while passing more than 400 mAh/g in the discharge, even though the theoretical capacity for the one electron reduction of S_3^- is only 278 mAh/g. There is also no apparent signal from the reaction product of the second plateau, a consequence of forming multiple or short-lived polysulfide species that do not contribute a single XANES feature.

Together, these observations suggest that the second set of reduction processes are dominated by the reactivity of the radical anion S_3^-. Early in the transition to the second plateau, this electroactive species is formed by dissociation of long-chain polysulfides, while the mechanism that for the persistence of S_3^- later in the plateau is

still uncertain. One reasonable explanation would be a series of disproportionation reactions that collectively can convert the reduced S_3^{2-} to a more reduced polysulfide and partially replenishing the oxidized species.[10,25] Typical reactions may include:

$$S_3^- + e^- \rightarrow S_3^{2-} \quad (1)$$

$$S_3^{2-} + S_n^{2-} \leftrightarrow S_6^{2-} + S_{n-3}^{2-} \, (3 < n < 8) \quad (2)$$

$$S_6^{2-} \leftrightarrow 2S_3^- \, (3)$$

$$2S_3^{2-} \leftrightarrow S_4^{2-} + S_2^{2-} \, (4)$$

$$2S_4^{2-} \leftrightarrow 2S_3^- + S_2^{2-} \, (5)$$

At the end of the lower voltage plateau, there is a concerted decrease in cell voltage and the peak intensities, as seen in the trends of Figure 6-4C and the XANES spectra in Figure 6-5. This is consistent with the assignment of the pre-peak to the dominant electroactive species (S_3^-) during the second voltage plateau. A new peak at higher energies, which matches the first XANES peak of the Li_2S standard (Figure 6-4B), becomes distinct as abruptly and at the same cell voltages as the diffraction peak from Li_2S (Figure 6-5B). This observation confirms that Li_2S is formed at the end of discharge for batteries with a gel polymer electrolyte. The lack of isosbestic points or intermediate peaks indicates that there must be additional disproportionation steps involved in the formation of lithium sulfide. After the cell voltage is held at 1.5 V for 1 hour, the intensity over the range 2471-2474 eV further decreases relative to the Li_2S signal (Figure 6-4C), supporting the conclusion that signals over this energy range are due to incompletely reduced polysulfide species.

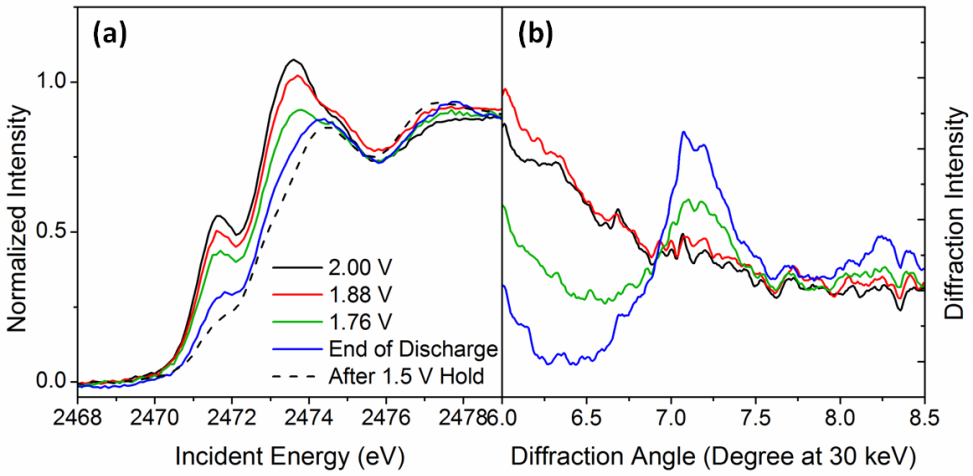

Figure 6-5. Final stage of lithium-sulfur battery discharge. (a) XANES results at selected cell voltages, at the end of the discharge, and after a 1 hour potential hold at 1.5 V. (b) XRD results at the same cell voltages and at the end of the discharge.

During recharging, the same spectroscopic signals are observed but in reverse sequence, suggesting that the same key species are involved in the process of sulfide oxidation. This is in contrast to models proposed in the literature,[35] and emphasizes the chemical reversibility of the reaction pathway.

6-5. Discussion of Mechanism

The above spectroscopic observations support a sulfur reduction mechanism primarily defined and controlled by disproportionation reactions. Figure 6-6 summarizes the data available through this in-situ XRD and XAS study and outlines a proposed mechanism for sulfur reduction in a Li/S battery with a gel polymer electrolyte. In the upper voltage plateau, elemental sulfur (cyclic S_8) is reduced and reacts to form longer chain polysulfides. These polysulfides dissociate to form a mix of radical anions and shorter-chain polysulfides during the transition between the voltage plateaus, and are further reduced through the lower voltage plateau by the electrochemical mediation of S_3^- radical anions and equilibration with more reduced polysulfides (e.g. S_3^{2-}). The fact that S_3^- is observed throughout the second discharge plateau, long beyond the theoretical charge associated with the average oxidation state

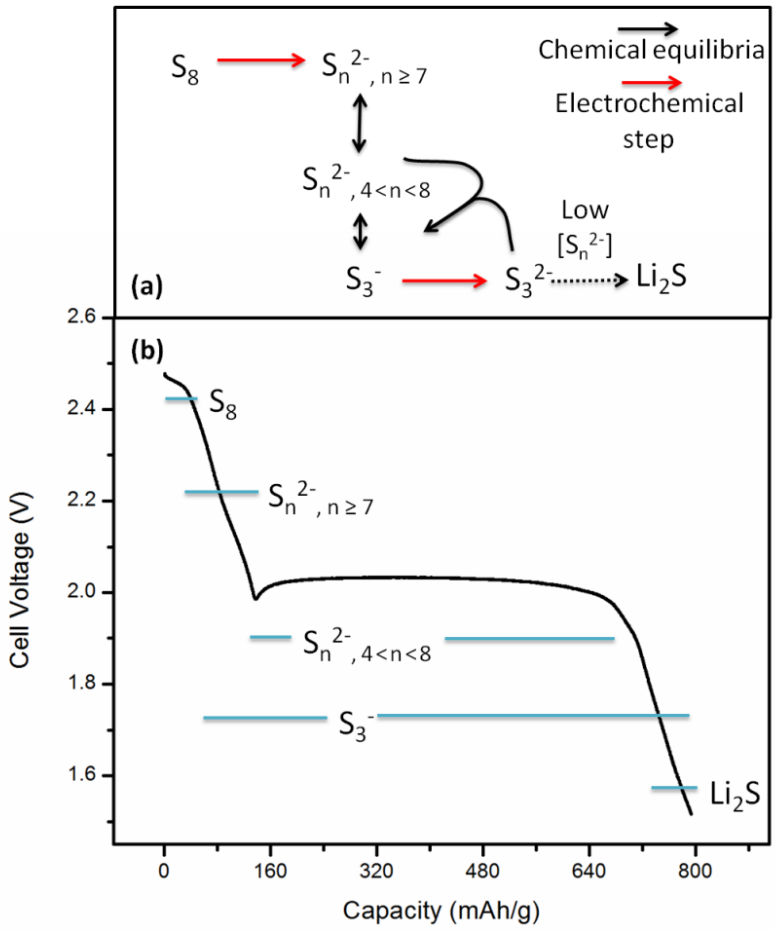

Figure 6-6. Summary and Proposed Mechanism. (a) Outline of electrochemical steps and chemical equilibria in sulfur reduction mechanism. (b) Summary of polysulfide species observed, overlaid with a typical discharge profile.

S_3^{2-} (557 mAh/g), indicates that the later stages of the second plateau are due to disproportionation reactions that replenish the radical anion. However, once the concentration of polysulfides is too low for these reactions to sustain a threshold concentration of radical anions, the cell voltage drops and discharge ends.

Chemical equilibria between/among polysulfides enable the reaction to approach chemical reversibility under the appropriate conditions, as is apparent in the sulfur XANES of Figure 6-4A. However, they also limit the practical discharge capacity of the battery if the chemical equilibria maintain a distribution of

incompletely reduced polysulfides. Reaction 5 provides an example of how this could occur – in order to replenish the radical anion S_3^-, two reduced polysulfides must interact. As the concentration of reduced polysulfides decreases, the probability of interaction will decrease and the system will be unable to replenish a sufficient concentration of the electroactive species.

Perhaps a more significant challenge is the possible loss of polysulfides into bulk solution, that is, away from the electrode. The possible effect of soluble sulfur on the cell capacity is demonstrated by the scenarios outlined in Table 6-2. In the ideal case, all sulfur is converted to lithium sulfide to obtain the full 1,672 mAh/g capacity. However, if even 1 mol% of the sulfur species is dissolved as S_8^{2-}, the accessible capacity drops by over 100 mAh/g (>6% of the full capacity). Based on the XANES spectra of the discharged battery in Figure 6-5A, in a more reasonable scenario there are non-negligible concentrations of multiple sulfur species at the end of the first discharge, including at least S_4^{2-} and S_3^-. Assuming that reasonable concentrations of these species persist, only 64% of the ideal capacity is possible, even with a high relative concentration of Li_2S. These illustrative examples predict achievable capacities that are significantly more than what we observed in this report, but are in line with the observed first discharge capacities of the best reported lithium-sulfur cells.[17,41–43] Thus, the presence of sulfur as electrochemically-inactive polysulfides can reasonably account for a significant fraction of the discrepancy from theoretical capacities.

Based on the proposed reaction mechanism, sulfur can be most fully and reversibly reduced under conditions in which there is a high concentration of sulfur species within the diffusion layer region of the electrode. Under these conditions, chemical equilibria facilitate formation of electroactive radical anions and the corresponding dianions for the respective reduction and oxidation reactions. This

agrees with several reports of promising battery performance using sulfur incorporated into mesoporous carbons,[17,41,43] which limit the diffusion of sulfur into solution[2] and maintain high local polysulfide concentrations. Further, the proposed mechanism highlights the possible strategy of altering chemical equilibria to favor formation of the electroactive sulfur species, especially S_3^-, in order to maximize the available capacity from elemental sulfur.

6-6. Conclusions

This work presents a joint in-situ XRD and XAS study of sulfur in a Li/S battery environment, demonstrating the utility of these techniques to probe the key species involved in lithium-sulfur battery operation and emphasizing the need for an in-situ molecular understanding of sulfur reduction pathways. Additional and ongoing efforts are necessary to probe the effects of specific cell parameters (e.g. electrolytes, carbons) on the reaction, as well as to collect and theoretically model absorption spectra for reduced sulfur species in support of the assignments discussed above. However, this research clearly shows that a limited number of sulfur species predominate through the cycle of a sulfur cathode and predicts that altering/controlling chemical equilibria to favor the formation of specific polysulfides can dramatically improve the capacity of lithium-sulfur cells.

Table 6-2. Simple predictions of maximum accessible capacity, assuming specific concentrations of incompletely reduced polysulfides do not completely equilibrate.

	Relative Species Concentration (% mol/% *mass sulfur*)				
Scenario	S_8^{2-}	S_6^{2-}	S_3^{-}	Li_2S	Accessible Capacity (mAh/g)
1	0	0	0	100/*100*	1672
2	1/*7.4*	0	0	99/*92.5*	1562
3	1/*5.3*	5/*19.7*	10/*19.7*	84/*55.3*	1044

REFERENCES

(1) Kumaresan, K.; Mikhaylik, Y.; White, R. E. *J. Electrochem. Soc.* **2008**, *155*, A576–A582.

(2) Dominko, R.; Demir-Cakan, R.; Morcrette, M.; Tarascon, J.-M. *Electrochem. Commun.* **2011**, *13*, 117–120.

(3) Yuan, L.; Qiu, X.; Chen, L.; Zhu, W. *J. Power Sources* **2009**, *189*, 127–132.

(4) Kolosnitsyn, V. S.; Kuzmina, E. V.; Karaseva, E. V.; Mochalov, S. E. *J. Power Sources* **2011**, *196*, 1478–1482.

(5) Levillain, E.; Gaillard, F.; Lelieur, J. P. *J. Electroanal. Chem.* **1997**, *440*, 243–250.

(6) Evans, A.; Montenegro, M. I.; Pletcher, D. *Electrochem. Commun.* **2001**, *3*, 514–518.

(7) Leghie, P.; Lelieur, J.-P.; Levillain, E. *Electrochem. Commun.* **2002**, *4*, 406–411.

(8) Martin, R. P.; Doub Jr, W. H.; Roberts Jr, J. L.; Sawyer, D. T. *Inorg. Chem.* **1973**, *12*, 1921–1925.

(9) Steudel, R. *Top. Curr. Chem.* **2003**, 127–152.

(10) Gaillard, F.; Levillain, E.; Lelieur, J. P. *J. Electroanal. Chem.* **1997**, *432*, 129–138.

(11) Han, D.-H.; Kim, B.-S.; Choi, S.-J.; Jung, Y.; Kwak, J.; Park, S.-M. *J. Electrochem. Soc.* **2004**, *151*, E283.

(12) Kim, B.-S.; Park, S.-M. *J. Electrochem. Soc.* **1993**, *140*, 115–122.

(13) Merritt, M. V.; Sawyer, D. T. *Inorg. Chem.* **1970**, *9*, 211–215.

(14) Tobishima, S.; Yamamoto, H.; Matsuda, M. *Electrochim. Acta* **1997**, *42*, 1019–1029.

(15) Jung, Y.; Kim, S.; Kim, B.-S.; Han, D.-H.; Park, S.-M.; Kwak, J. *Int. J. Electrochem. Sci.* **2008**, *3*, 566–577.

(16) Peled, E.; Sternberg, Y.; Gorenshtein, A.; Lavi, Y. *J. Electrochem. Soc.* **1989**, *136*, 1621–1625.

(17) Ji, X.; Lee, K. T.; Nazar, L. F. *Nat. Mater.* **2009**, *8*, 500–506.

(18) Kolosnitsyn, V. S.; Karaseva, E. V.; Seung, D. Y.; Cho, M. D. *Russ. J. Electrochem.* **2002**, *38*, 1314–1318.

(19) Shim, J.; Striebel, K. A.; Cairns, E. J. *J. Electrochem. Soc.* **2002**, *149*, A1321.

(20) Cheon, S.-E.; Ko, K.-S.; Cho, J.-H.; Kim, S.-W.; Chin, E.-Y.; Kim, H.-T. *J. Electrochem. Soc.* **2003**, *150*, A800–A805.

(21) Yamin, H.; Gorenshtein, A.; Penciner, J.; Sternberg, Y.; Peled, E. *J. Electrochem. Soc.* **1988**, *135*, 1045–1048.

(22) Cheon, S.-E.; Ko, K.-S.; Cho, J.-H.; Kim, S.-W.; Chin, E.-Y.; Kim, H.-T. *J. Electrochem. Soc.* **2003**, *150*, A796.

(23) Jeon, B. H.; Yeon, J. H.; Kim, K. M.; Chung, I. J. *J. Power Sources* **2002**, *109*, 89–97.

(24) Kolosnitsyn, V. S.; Karaseva, E. V. *Russ. J. Electrochem.* **2008**, *44*, 506–509.

(25) Jung, Y.; Kim, S. *Electrochem. Comm.* **2007**, *9*, 249–254.

(26) Morcrette, M.; Chabre, Y.; Vaughan, G.; Amatucci, G. G.; Leriche, J.-B.; Patoux, S.; Masquelier, C.; Tarascon, J.-M. *Electrochim. Acta* **2002**, *47*, 3137–3149.

(27) Totir, D. A.; Antonio, M. R.; Schilling, P.; Tittsworth, R.; Scherson, D. A. *Electrochim. Acta* **2002**, *47*, 3195–3200.

(28) Hassoun, J.; Sun, Y. K.; Scrosati, B. *J. Power Sources* **2011**, *196*, 343–348.

(29) Nelson, J.; Misra, S.; Yang, Y.; Jackson, A.; Liu, Y.; Wang, H.; Dai, H.; Andrews, J. C.; Cui, Y.; Toney, M. F. *J. Am. Chem. Soc.*

(30) Du Pasquier, A.; Warren, P. C.; Culver, D.; Gozdz, A. S.; Amatucci, G. G.; Tarascon, J. M. *Solid State Ionics* **2000**, *135*, 249–257.

(31) Hammersley, A. P.; Svensson, S. O.; Hanfland, M.; Fitch, A. N.; Häusermann, D. *High Pressure Res.* **1996**, *14*, 235–248.

(32) Ravel, B.; Newville, M. *J. Synchroton Radiat.* **2005**, *12*, 537–541.

(33) Sharma, R. A. *J. Electrochem. Soc.* **1972**, *119*, 1439–1443.

(34) Okamoto, H. *J. Phase Equilib.* **1995**, *16*, 94–97.

(35) Ji, X.; Nazar, L. F. *J. Mater. Chem.* **2010**, *20*, 9821.

(36) Ryu, H. S.; Ahn, H. J.; Kim, K. W.; Ahn, J. H.; Lee, J. Y. *J. Power Sources* **2006**, *153*, 360–364.

(37) Guo, Y.; Zhao, J.; Yang, S.; Yu, K.; Wang, Z.; Zhang, H. *Powder technology* **2006**, *162*, 83–86.

(38) Eckert, B.; Steudel, R. *Top. Curr. Chem.* **2003**, 181–191.

(39) Rauh, R. D.; Shuker, F. S.; Marston, J. M.; Brummer, S. B. *J. Inorg. Nucl. Chem.* **1977**, *39*, 1761–1766.

(40) Fleet, M. E.; Liu, X. *Spectrochim. Acta B* **2010**, *65*, 75–79.

(41) Liang, C.; Dudney, N. J.; Howe, J. Y. *Chem. Mater.* **2009**, *21*, 4724–4730.

(42) Liang, X.; Wen, Z.; Liu, Y.; Zhang, H.; Huang, L.; Jin, J. *J. Power Sources* **2011**, *196*, 3655–3658.

(43) Jayaprakash, N.; Shen, J.; Moganty, S. S.; Corona, A.; Archer, L. A. *Angew. Chem. Int. Ed.* **2011**, *50*, 1–6.

CHAPTER 7

CELL DESIGN FOR LITHIUM-SULFUR ELECTROCHEMICAL ENERGY STORAGE

7-1. Introduction

Lithium-sulfur batteries are tremendously appealing from a practical perspective. Sulfur is inexpensive, widely available, and in its elemental form, easily processed and purified. Based on the in-situ characterization of lithium-sulfur batteries described in earlier chapters, it is clear that the complexities of the reaction mechanism still permit the reversible transformation of a reasonable fraction of sulfur to between the neutral and fully lithiated states. Thus, there do not appear to be any mechanistic reasons why the full capacity of 1672 mAh/g-sulfur should not be realized. Furthermore, unlike the lithium-oxygen system, sulfur and lithium can both be stored in a closed system with attractive volumetric and outstanding gravimetric energy densities.

However, just because sulfur cathodes can be used in a closed system does not mean that they should be used as a 'drop-in replacment' for traditional lithium-ion cathode materials. The reactivity of sulfur and reduced sulfur species differs drastically from lithium intercalation chemistries, raising a number of possible material incompatibilities with common battery solvents[1] and cell components, especially metals.[2] In addition, early stages of sulfur reduction appear to occur in solution, making the battery electrolyte solution an active participant in the reaction.

Unfortunately, most research on sulfur cathodes has used traditional battery cell designs, such as swagelock, pouch, or especially coin cells, with scarce evidence of systematic control over sulfur/solvent ratios. For example, it is a generally accepted practice to report mass ratios of sulfur, carbon and cathode in the binder, but very rare

to report volume or mass of electrolyte added to the cell. Similarly, even though electrode size may be reported, there is no established practice for reporting the fraction of area or volume within the cell that is not occupied by electrodes, as necessary to determine the active/inactive volume in the cell. This lack of detail has less impact on comparing results from within a set of prototype lithium-sulfur batteries, when they are all prepared with the same or similar cell components and by the same researcher; however, it could have profound effects when scientifically evaluating the influence of a new material or approach.

It is a serious challenge to evaluate the effects of varying ratios of sulfur/solvent and active/inactive volume. As discussed in previous chapters, spectroscopic speciation of reduced sulfur species is non-trivial, and there is at present no single technique that can resolve the ensemble of sulfur species present in a battery. Potentiometric coulometry, as commonly measured with prototype lithium-sulfur cells, does not resolve specific species but can provide insights based on the total lithium-storage capacities. Surprisingly, only one report appears in the literature where the researchers systematically studied the influence of solvent quantity on sulfur discharge performance, and the authors observe a dramatic effect – a doubling of the solvent quantity resulted in a 250% increase in the first discharge capacity, up to 84% of theoretical capacity.[3] It is reasonable that this relationship would be influenced by differences between solvent types, electrode porosity and composition, and active/inactive volume, but this one result demonstrates that additional studies are warranted. This is particularly true since some of the best reports for prototype lithium-sulfur cells generally involve low loadings of sulfur[4,5] (e.g. < 30 wt% sulfur in the cathode) , conditions that may also result in lower sulfur/solvent ratios.

These questions are all the more pressing because the variable performance of sulfur cathodes. The best lithium-sulfur cells only reach ~85% of theoretical capacity at 1.5

V[4,6,7] on the first discharge and capacities decrease significantly on subsequent cycling.[4] Far more common in the literature is a first discharge capacity near 70-75%. In this chapter, we present a new electrochemical cell format that will be key to understanding if the performance is sub-theroretical because of sulfur distribution within the cell, a chemical reactivity of reduced sulfur with cell components, or a slow step in the reaction pathway.

7-2. Direct Observation of Sulfur Distribution in Coin Cell Geometry

To demonstrate the challenges associated with traditional cell formats, an optically transparent electrochemical cell was prepared with geometry very close to a standard 2032 coin cell. To make sure the cell provided representative results, the cell was assembled with the same cathode composition and size (0.97 cm^2), polymeric separator, and anode size, and a standard quantity of electrolyte solution (120 μL). The volume of the cell was approximately 10% less than a coin cell due to the use of o-rings instead of a polyethylene washer, with most of the discrepancy due to a slightly smaller cell diameter (1.88 cm for the optical cell vs. 2.00 cm for a coin cell).

As discussed in chapter 4, the variation of electronic structure with sulfur chain length results in several different colors, including reds from longer-chain polysulfides such as S_8^{2-} and greens from intermediate polysulfides such as S_3^{-}/S_6^{2-}/S_4^{2-}. Supernatant solutions above sulfur and the shortest polysulfides (i.e. Li_2S_2 and Li_2S) appear colorless due to the species' low solubility and high energy transitions, with absorbance in the UV. The presence of different polysulfides in solution than thus be probed semi-quantitatively using UV-Vis absorption spectra, or monitored qualitatively by optical imaging. Optical imaging has the advantage of providing both time and spatial resolution, without the requirement for a high-transmittance path through the entire cell.

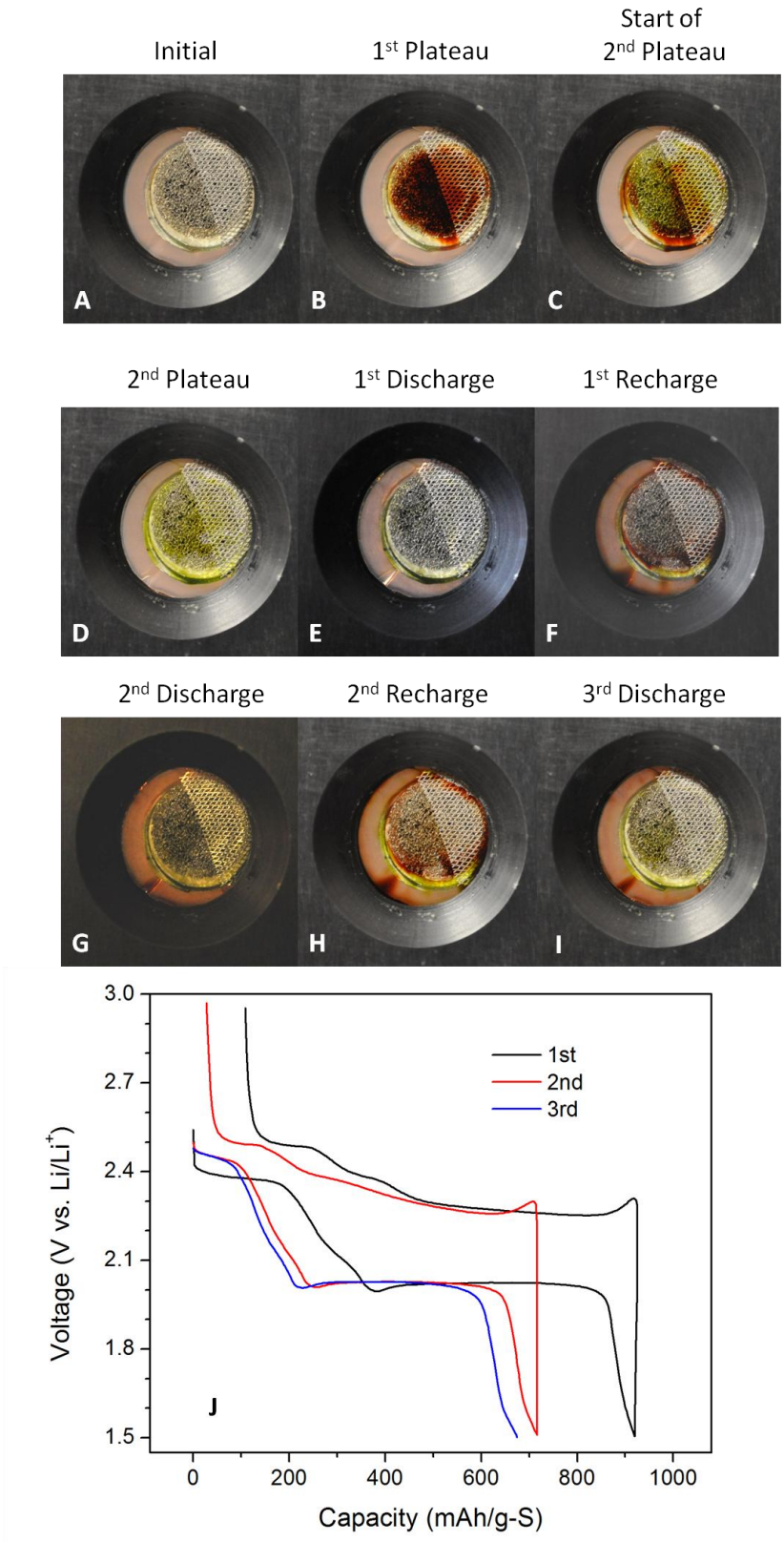

Figure 7-1. Optical imaging of polysulfide species in coin cell geometry. Cell prepared with 0.97 cm^2 cathode loaded with 1.7 mg S_8, 120 µL electrolyte composed of 1 M LiTFSI + 0.1 M $LiNO_3$ + tetra(ethyleneglycol)dimethyl ether, and 1.27 cm^2 Li anode. Cycled at a rate of 100 mA/g-sulfur between the limits 1.5 and 3.0 V vs. Li anode.

Figure 7-1 summarizes results during the first few discharge/charge cycles at a low rate (100 mA/g). During the first discharge (Figure 7-1A-E), the solution near the cathode rapidly turns deep red, as expected for the formation of long-chain polysulfides. The red color persists throughout the first voltage plateau (Figure 7-1B), then turns green at the start of the second voltage plateau (Figure 7-1C). The green color becomes gradually less intense through the second plateau (Figure 7-1D) and almost entirely disappears within the electrode area at the end of the discharge (Figure 7-1E) as the polysulfides are reduced to insoluble products. These observations are fully consistent with a previous XAS study of sulfur species present in the cathode through the first discharge (Chapter 6).

The most important insights gained from optical imaging are about the distribution of polysulfides in the cell. While the green color from short-chain polysulfides has almost disappeared within the cathode after the first discharge, significant green coloration is still present outside the cathode radius and especially just outside of the slightly larger anode radius (Figure 7-1E). On subsequent charge and discharge, a more complex distribution of polysulfides forms within the cell: after the first recharge red long-chain polysulfides are in solution around the cathode, with green polysulfides in a region where the anode is not fully covered by the cathode, and with some additional long-chain polysulfides present in a pocket of electrolyte solution separated from the anode and cathode (lower left of Figure 7-1F).

The images during the second discharge and charge show that the polysulfides gradually accumulate in the electrochemically inactive region of the cell. The pocket of red polysulfides in the lower left of Figure 7-1F becomes smaller but does not disappear in the fully discharged state (Figure 7-1G and I), and larger in the recharged state (Figure 7-1H). Interestingly, the second recharge also shows significantly more green color from intermediate polysulfides than does the first recharge. This

progressive increase of colored sulfur species in solution is correlated with a decrease in charge storage capacity. (Figure 7-1J)

This distribution of polysulfides and the decrease in cell capacity may be explained by the high solubility of reduced sulfur species in many battery solvents. Long-chain polysulfides (e.g. nominal composition Li_2S_8) are soluble to at least[8–10] 10 M [S] in ethereal solvents after equilibration for >24 hours. If the sulfur were constrained to the electrolyte solution between the electrodes, the effective concentration of sulfur in the solvent would be near this value, based on sulfur mass loading, electrode radii and a reasonable (100 μm) separation between the electrodes. However, considering the total quantity of electrolyte added to the cell, the average concentration of sulfur is only 0.44 M [S]. (Table 7-1) (Note that the atomic concentration is the preferred unit to avoid confusion due to the change in formula unit with degree of reduction: 1 M S_8 = 8 M S2-) This simple calculation suggests that, if the entire cell were allowed to come to equilibrium at the correct state of charge, all the sulfur could easily go into solution as long-chain polysulfides. Optical imaging indeed shows that long-chain polysulfides rapidly go into solution, with the solution within the electrode turning red within the first 50 mAh/g-sulfur.

Table 7-1. Effect of sulfur redistribution on sulfur remaining in cathode.

Bulk Electrolyte Concentration (M [S])	Cathode Local Concentration (M [S])	% Sulfur Remaining in Cathode
0	9.4	100
0.01	9.2	98
0.05	8.4	89
0.1	7.4	78
0.2	5.3	57
0.3	3.3	43
0.44	0.44	5

Assumptions: Anode and cathode both 1.2 cm diameter with 100 micron separation. Sulfur loading of 1.7 mg with 120 μL total electrolyte in cell.

The transport of polysulfides in the cell should be described by Fick's second law, that

is, it should be proportional to the concentration gradient; thus, the polysulfides are most likely to diffuse away from the region of highest concentration (i.e. the cathode) into the non-polysulfide-containing electrolyte solution, with the greatest transport of those polysulfides with the highest concentration in solution (i.e. the red long-chain polysulfides). This is in agreement with the experimental observations (Figure 7-1E-I). Red long-chain polysulfides consistently are observed furthest from the electrode, with the red color persisting long beyond the end of the first discharge plateau. Transport of the polysulfides back to the electrode would be expected to be slower than transport away from the electrode, since the local concentration of polysulfides in solution (<< 0.4 M) is significantly less than the initial concentration within the electrode (~10 M). In fact, additional experiments (Figure 7-2) observed that red polysulfides sufficiently separated from the carbon cathode film (~5 mm) were present all the way to the very end of discharge. This may have been disguised in the cell shown in Figure 7-1E by solvent accumulation outside of the window area.

The spatial heterogeneity of polysulfides occurs even in regions where the electrolyte solution is in contact with a conductive mesh. This suggests that the 'isolation' of polysulfides is due to two effects: ionic resistance and solution coming into contact with a relatively smaller electroactive surface area. Due to the high resistivity of the organic electrolyte solution (~1 mS/cm)[8], reactions at a conductive support even a short distance (~0.5 mm) away from the anode may introduce a significant potential

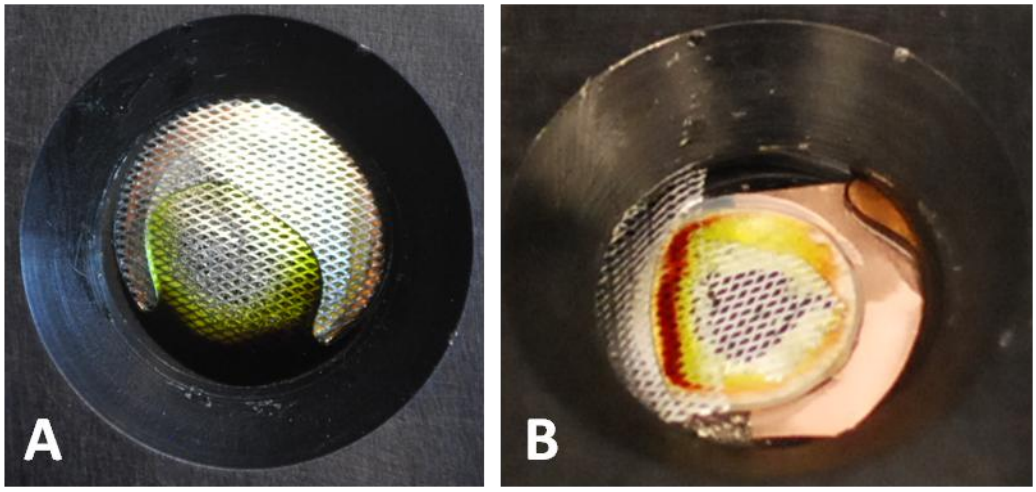

Figure 7-2. Optical images of discharged sulfur cathodes. (A) 50 wt% sulfur in cathode, loading 1.1 mg of sulfur, with the same cell geometry and electrolyte solution as in Figure 7-1, but with aluminum mesh across entire cathode region. Image taken after discharge to 1.5 V at rate of 100 mA/g-S. (B) 50 wt% sulfur in cathode, loading 0.5 mg sulfur, with 50 µL of the same electrolyte. Image taken after discharge to 1.5 V at rate of 100 mA/g-S and equilibration for 1 h.

drop relative to the electrode potential at the main cathode, depending on the thickness of the solvent layer. Perhaps more significantly, as the polysulfides diffuse out to the region with a planar conductive surface, the species enter a region where the ratio of electrode surface area to solution volume is dramatically smaller than the in the carbon cathode matrix. Even though there is electroactive surface area throughout the cathode side of the cell, the cell voltage and discharge time is dominated by the high surface

area carbon matrix. Since the quantity of sulfur within cathode matrix diminishes, but not the applied current, the remaining sulfur is subjected to increasing mass-averaged rates.

Upon extended cycling, the polysulfides should continue to diffuse out of contact with the cathode matrix until the concentration of sulfur species away from the cathode approaches the average concentration in the cell (~0.4 M). The flux of polysulfides out of the cathode region should be highest in the initial cycle, when the concentration gradient is largest, and steadily diminish on subsequent cycles. This is consistent with the electrochemical results shown here (Figure 7-1J) as well as nearly universally reported in the literature,[4–7,11–15] although this may include other contributions to the observed capacity fade (e.g. deposition of lithium sulfide on the anode surface).[16] Assuming the average concentration of sulfur in the bulk solution at the end of the first discharge approaches 100 mM [S], 100 times below the limiting concentration, over 20% of the sulfur would be lost into solution in the first discharge alone. (Table 7-1) This is roughly consistent with ex-situ[6,11,15] and in-situ (Chapter 6) probes of sulfur concentration in the electrolyte upon cycling. While this explanation does fully not explain the sub-theoretical capacities observed for lithium-sulfur cells at short cycles, it does demonstrate a thermodynamic driving force for capacity fading in standard cell designs.

In summary, optical imaging demonstrates that sulfur in coin cell cathodes rapidly establish a spatially heterogeneous distribution of concentrations and compositions, with a significant fraction of sulfur species into the excess electrolyte solution in the cell. Diffusion of sulfur species into the electrolyte results in lower capacities due to both loss of electrochemically active sulfur and the consequential increase in applied current density rate for the remaining sulfur, which imposes greater kinetic demands on the chemical equilibria that form the electroactive sulfur species. Unfortunately, the exact distribution of polysulfides will depend on a number of cell-specific parameters, including electrolyte quantity, cathode porosity, and mass of sulfur in the cathode, that make it difficult to extract quantitative performance data for comparison between research groups. While coin, swagelock, and pouch cells are familiar to experienced battery researchers, the solubility-driven redistribution of polysulfides makes these cell designs inappropriate for systematic studies of the sulfur reduction mechanism or how electrode additives (e.g. nanostructured carbons) influence the lithium-sulfur cell performance.

7-3. Criteria for Sulfur Electrochemical Cell Design

The experimental complications of studying sulfur electrochemistry demand a new electrochemical cell design that is less affected by the varying solubility of sulfur species. Based on the experimental observations above, the essential operational principles include:

- Constraining electrolyte solution to remain within the electroactive region, or very short distances away from electrochemically active surface
- Prevention of polysulfide diffusion to the lithium anode
- Ability to control and test varying loadings and concentrations of sulfur and/or electrode additives

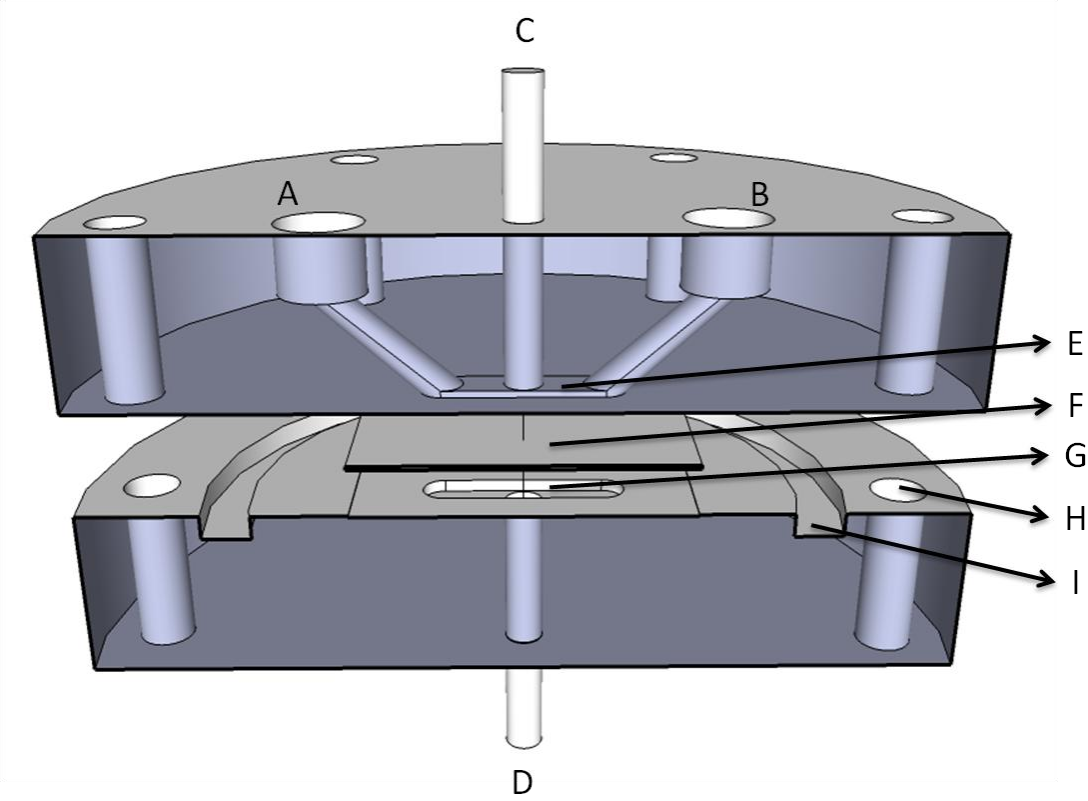

Figure 7-3. Schematic of cell for sulfur electrochemical studies. Body constructed from polyether ether ketone (PEEK). (A) Solution inlet (B) Solution outlet (C) Threaded stainless steel rod for contact with cathode and (D) anode. (E) Cathode reaction zone, to be filled with electrode and sulfur species, and sealed with a custom-cut teflon tape gasket (F) Ceramic lithium-ion conductive electrolyte membrane (G) Anode reaction zone. Lithium makes contact with stainless rod but is isolated from ceramic electrolyte by a Celgard separator saturated with 1 M LiTFSI + TEGDME (H) 6 bolt holes for cell assembly (I) O-ring groove for optional o-ring, for use of cell in aerobic conditions.

Figure 7-3 shows a cell design that meets these criteria through the use of a defined reaction volume and a solid lithium-ion conductive electrolyte membrane. The defined reaction volume enables probing the effect of electroactive surface area and/or electrode material, while the solid electrolyte opens a wide range of electrolyte studies – including electrolytes that are not stable in contact with lithium. The initial results for the new electrochemical cell are reported and discussed below.

7-4. Solvent Effects on Sulfur Electrochemistry

Initial work with the cell was performed under static conditions to demonstrate

materials compatibility with polysulfides and a selection of interesting solvents. TEGDME is a common solvent for prototype lithium-sulfur batteries, but N,N-dimethylformamide (DMF) and N-methylpyrrolidone (NMP) chemically react with lithium. This is unfortunate, since both solvents have much high dielectric constants that TEGDME and should form more conductive electrolyte solutions.The electrochemistry of sulfur in DMF[17–22] at dilute concentrations has been widely studied, but this is the first report of DMF and NMP for lithium-sulfur battery applications.

For this work, solutions were prepared with 1 M [S] at nominal composition Li_2S_8, without regard to the actual ensemble of sulfur species present in solution. The cell was assembled with a nickel foam electrode in the cathode compartment. A known quantity of solution was injected into the cell, and the cell cycled at the desired rates. For the most viscous solvent, TEGDME, several cycles were required to obtain a stable response due to slow electrolyte percolation through the nickel electrode.

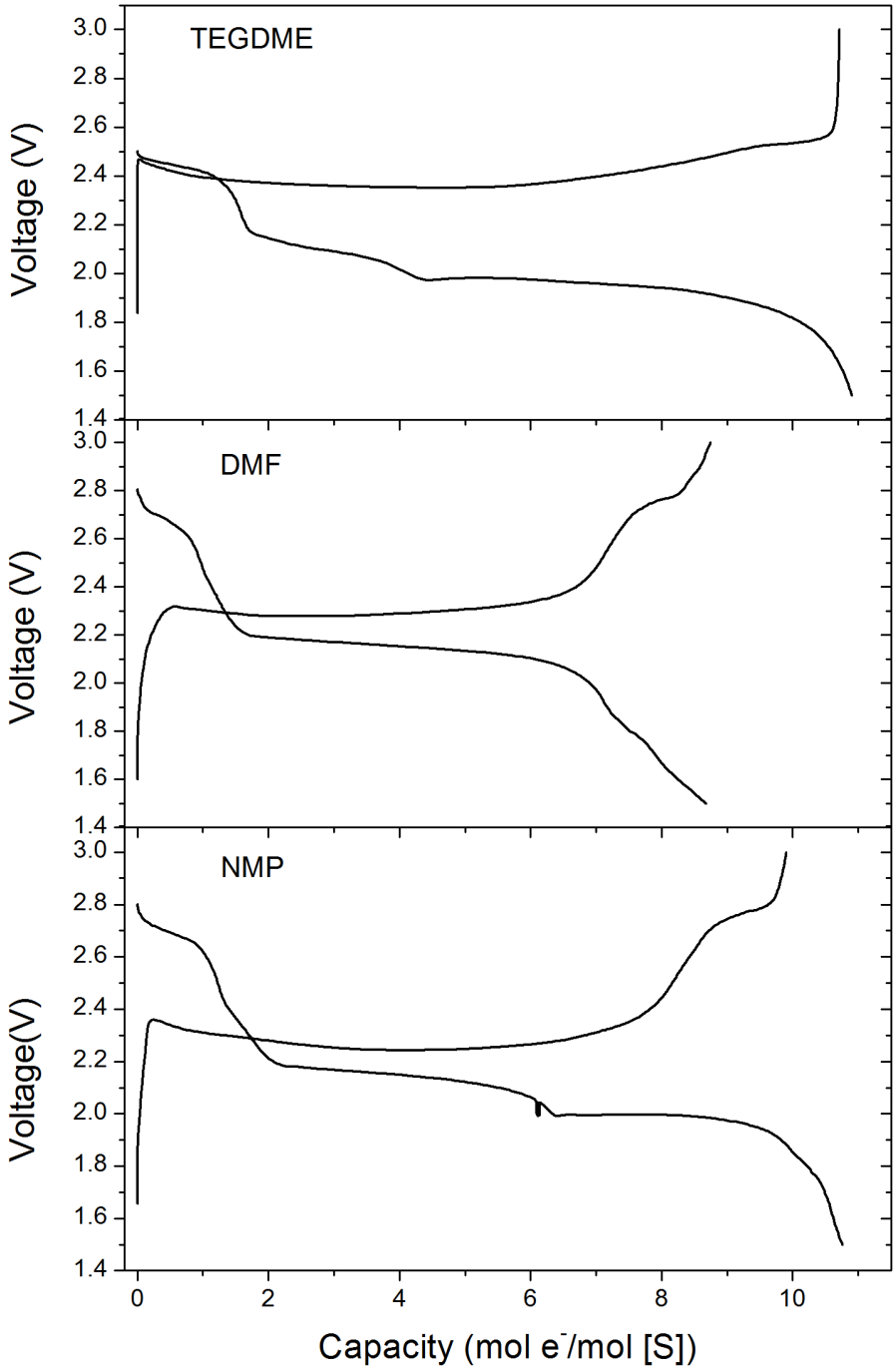

Figure 7-4. 50 mA/g-S discharge/charge cycle of polysulfide solutions in electrochemical cell. 1 M [S] (nominal composition Li2S8) + 1 M LiTFSI + solvent. Nickel foam as athode current collector.

The first stable cycle at slow rate (50 mA/g) is shown in Figure 7-4 for 1 M sulfur in TEGDME, DMF, and NMP. In each case the coulombic efficiency (cathodic

charge/anodic charge) near one, indicating that the solid electrolyte successfully prevents polysulfide diffusion to the lithium anode and the resulting shuttle behavior. The discharge in NMP is ~10% longer than the recharge, suggesting a chemical reactivity of reduced sulfur species with NMP.[23] However, cycles in TEGDME and DMF consistently had coulombic efficiencies of 100 +/- 2%. Below the responses in each of the solvents is discussed in more detail with an eye towards understanding the influence of solvent on the reduction mechanism.

TEGDME

The response of sulfur in TEGDME has three distinct plateaus, including the two plateaus that are almost universally reported at ~2.4 and 2.0 V, as well as third intermediate plateau (~2.1V) that is similar but more distinct than a quasi-plateau in Figure 7-1J as well as previous reports of sulfur cathodes in ethereal solvents[5,7,24] From the charge passed with each plateau, the voltage plateaus at 2.4 and 2.1 V can be roughly assigned to the 2 e^- formation of S_8^{2-} followed by the additional 2 e^- to reduce S_4^- to S_4^{2-}; these assignments are consistent with theoretical predictions of reduction potentials (Chapter 5) and previous spectroelectrochemical studies.[17] The plateau from formation of S_4^{2-} is more pronounced than in coin cell studies because the dissociation of S_8^{2-} to electroactive S_4^- (reaction 1) is favored at lower concentrations of sulfur.

$$S_8^{2-} \leftrightarrow 2S_4^- \quad (1)$$

The absolute ratio of S_4^- and S_8^{2-} are determined by the unknown dissociation constant for the reaction, but the change in ratios is only weakly dependent on the dissociation constant. Thus, for the range of dissociation constants of 0.1 – 1e-9, the equilibrium ratio of S_4^-/S_8^{2-} is a factor of 3.6-3.2 larger at 1 M [S] than at 10 M [S]. Assuming that the forward rate for dissociation is reasonably fast and independent of concentration, a lower concentration of polysulfides should results in a higher relative concentration of the electroactive S_4^- and a more pronounced voltage plateau from its reduction.

The final plateau in TEGDME is consistent with reduction of S_3^- and possibly S_2^- (Chapter 5) to eventually form Li_2S. The reactions to form these species are not known conclusively, but it is likely that they consist of both dissociation reactions from intermediate chain polysulfides, such as reaction 2, and disproportionations of shorter polysulfides, such as reactions 3-6:

$$S_6^{2-} \leftrightarrow 2S_3^- \quad (2)$$

$$S_3^{2-} \leftrightarrow S_2^{2-} + 2S_4^{2-} \quad (3)$$

$$2S_4^{2-} \leftrightarrow 2S_3^- + S_2^{2-} \quad (4)$$

$$S_2^{2-} + 2Li^+ \leftrightarrow Li_2S_{2\downarrow} \quad (5)$$

$$3Li_2S_{2,solid} \leftrightarrow Li_2S_{4,soluble} + 2Li_2S_{solid} \quad (6)$$

These reactions should also be influenced by a change in polysulfide concentration. Interestingly, both dissociations (reactions 2 and 3) and solid-state disproportionations that form soluble products (e.g. Li_2S_4 in reaction 6) should favor the right-hand side of the reactions at lower polysulfide concentrations. This suggests that the best performance for the lithium-sulfur system may come at lower concentrations of sulfur. Initial results at 3.3 M and 1.0 M [S] in DMF, as well as a previous report based on polysulfides in THF solution,[25] support this conclusion.

DMF and NMP

Constant current lithiation of sulfur in DMF and NMP shows several differences from the lithiation in TEGDME. Most noticeably, the first voltage plateau is at 2.7 V vs. Li/Li+, over 200 mV higher than in TEGDME, that extends for approximately 1 e^-/S_8 (Figure 7-4). A similar shift in first reduction potential has also been reported for dilute concentrations of sulfur in DMF, DMAc, and DMSO, all solvents with significantly higher dielectric constants than TEGDME (ranging from ε = 32-46 vs. ε = 7, respectively).[22] In contrast, the second voltage plateau in all three solvents is at approximately the same potential, 2.1 V (Figure 7-4). It is likely that higher dielectric

solvents stabilize the formation of long-chain polysulfide diradical chains and radical anions, species which have been predicted (Chapter 5) to be reduced 100-200 mV more positive than the cyclic S_8 molecule. While less charge is associated with the first well-defined voltage in the higher-dielectric solvents, the charge passed before the start of the second plateau is similar in all three solvents (~2 e^-/S_8).

The second voltage plateau in DMF and NMP is at the same potential as in TEGDME, but corresponds to nearly twice as much charge, while the third voltage plateau is only observed in NMP and TEGDME. These results indicate that there are significant differences in the chemical equilibria that occur in each of the solvents, with higher dielectric solvents favoring the reduction of S_4^- species (2nd plateau) instead of S_3^- (3rd plateau).

Rate Capability

Additional insights into the kinetics of the chemical steps coupled to the electrochemical response in each solvent are found in the rate dependent chronopotentiometry (Figure 7-5). It is notable that this experiment would be very difficult using either electroanalytical techniques (Chapter 5) or coin cells (Section 7-1) due to the combination of long (>10 h) experiment times and uncertain interactions between sulfur species and the anode or excess solvent in the cell.

At faster rates, the capacity decreases for every solvent, although different processes are affected in TEGDME versus DMF and NMP. In TEGDME, the majority of the capacity loss is due to the third plateau, indicating slow chemical steps in the formation of S_3^-, with almost no capacity loss in the second plateau (formation of S_4^-). On the other hand, in DMF and NMP the second plateau decreases in length, in the

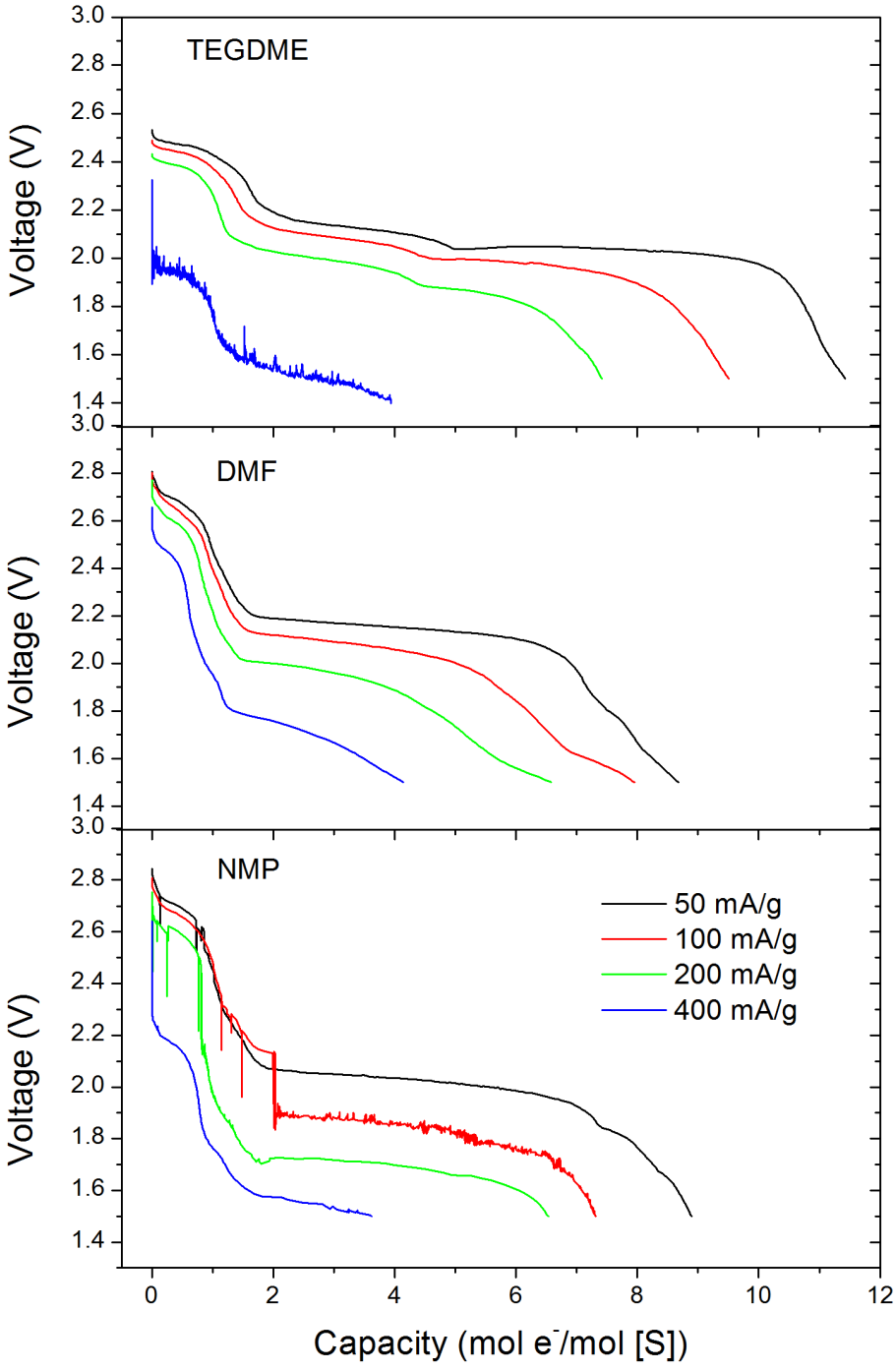

Figure 7-5. Electrochemical lithiation of polysulfide solutions at different rates. Solution composition as in Figure 7-4; 100 mA/g charge after each discharge.

limit of fast discharge rates approaching the plateau length observed in TEGDME. While additional spectroscopic results are needed to confirm the identities of the relevant chemical species, these results demonstrate the promise of the new cell design for electrochemical interrogation of the lithium-sulfur system.

7-6. Conclusions

Traditional designs for lithium-ion batteries are inappropriate for careful, systematic studies of the lithium-sulfur system due to the mixed solubility of sulfur species, along with the difficulty in probing the spatial heterogeneity of sulfur intermediates and products. Indeed, solubility-driven sulfur redistribution within coin cells is a reasonable explanation for the capacity fade observed in this and other studies. A new electrochemical cell design can prevent the loss of sulfur from the electrochemically-active region, and, by use of a ceramic lithium-ion conductive electrolyte, permits fundamental studies of sulfur reduction.

REFERENCES

(1) Gao, J.; Lowe, M. A.; Kiya, Y.; Abruna, H. D. *The Journal of Physical Chemistry C* **2011**.

(2) Eichinger, G.; Fritz, H. P. *Journal of Electroanalytical Chemistry and Interfacial Electrochemistry* **1975**, *58*, 369–374.

(3) Choi, J. W.; Kim, J. K.; Cheruvally, G.; Ahn, J. H.; Ahn, H. J.; Kim, K. W. *Electrochimica acta* **2007**, *52*, 2075–2082.

(4) Liang, C.; Dudney, N. J.; Howe, J. Y. *Chem. Mater.* **2009**, *21*, 4724–4730.

(5) Ji, L.; Rao, M.; Aloni, S.; Wang, L.; Cairns, E. J.; Zhang, Y. *Energy & Environmental Science* **2011**, *4*, 5053.

(6) Ji, X.; Evers, S.; Black, R.; Nazar, L. F. *Nature Communications* **2011**, *2*, 325.

(7) Jayaprakash, N.; Shen, J.; Moganty, S. S.; Corona, A.; Archer, L. A. *Angew. Chem. Int. Ed.* **2011**, *50*, 1–6.

(8) Chang, D.-R.; Lee, S.-H.; Kim, S.-W.; Kim, H.-T. *J. Power Sources* **2002**, *112*, 452–460.

(9) Rauh, R. D.; Shuker, F. S.; Marston, J. M.; Brummer, S. B. *J. Inorg. Nucl. Chem.* **1977**, *39*, 1761–1766.

(10) Yamin, H.; Peled, E. *J. Power Sources* **1983**, *9*, 281–287.

(11) Ji, X.; Lee, K. T.; Nazar, L. F. *Nat. Mater.* **2009**, *8*, 500–506.

(12) Wang, H.; Yang, Y.; Liang, Y.; Robinson, J. T.; Li, Y.; Jackson, A.; Cui, Y.; Dai, H. *Nano Lett.* **2011**.

(13) Yang, Y.; Yu, G.; Cha, J. J.; Wu, H.; Vosgueritchian, M.; Yao, Y.; Bao, Z.; Cui, Y. *ACS nano* **2011**.

(14) Zheng, G.; Yang, Y.; Cha, J. J.; Hong, S. S.; Cui, Y. *Nano Lett.*

(15) Diao, Y.; Xie, K.; Xiong, S.; Hong, X. *J. Electrochem. Soc.* **2012**, *159*, A421.

(16) Kolosnitsyn, V. S.; Karaseva, E. V.; Ivanov, A. L. *Russ. J. Electrochem.* **2008**, *44*, 564–569.

(17) Gaillard, F.; Levillain, E.; Lelieur, J. P. *J. Electroanal. Chem.* **1997**, *432*, 129–138.

(18) Leghie, P.; Lelieur, J.-P.; Levillain, E. *Electrochem. Commun.* **2002**, *4*, 406–411.

(19) Levillain, E.; Gaillard, F.; Lelieur, J. P. *J. Electroanal. Chem.* **1997**, *440*, 243–250.

(20) Levillain, E.; Gaillard, F.; Leghie, P.; Demortier, A.; Lelieur, J. *J. Electroanal. Chem.* **1997**, *420*, 167–177.

(21) Han, D.-H.; Kim, B.-S.; Choi, S.-J.; Jung, Y.; Kwak, J.; Park, S.-M. *J. Electrochem. Soc.* **2004**, *151*, E283.

(22) Jung, Y.; Kim, S.; Kim, B. S.; Han, D. H.; Park, S. M.; Kwak, J. *Int. J. Electrochem. Sci* **2008**, *3*, 566–577.

(23) Petrov, K.; Andreev, L. *Russ. Chem. Rev.* **1969**, *38*, 21–36.

(24) Zhang, S. S.; Read, J. A. *J. Power Sources* **2012**, *200*, 77–82.

(25) Rauh, R. D.; Abraham, K. M.; Pearson, G. F.; Surprenant, J. K.; Brummer, S. B. *J. Electrochem. Soc.* **1979**, *126*, 523–527.

CHAPTER 8

CONCLUSIONS AND FUTURE OUTLOOK

8-1. Overview

The research presented in this dissertation has developed the methodology required for in-operando studies of electrode materials for lithium-based batteries. In-operando studies are readily accessible for a range of characterization techniques, and provide multidimensional datasets that aid in understanding both spectral and electrochemical signals. Specific examples shown in this dissertation demonstrate the utility of this approach for understanding conversion reactions in anode materials (Chapter 3) and providing additional insights into the key species and reactions in the lithium-sulfur system (Chapters 4-7). In each of these cases, the direct coupling of electrochemical and spectral datasets was essential for demonstrating that the reactions were or were not occurring.

8-2. Analytical Studies of Sulfur Reactions

The electrochemical and spectroscopic studies of the sulfur reduction mechanism have supported a mechanism defined by dissociation and disproportionation reactions between polysulfide species, with the overall reduction of S_8 to Li_2S mediated by a limited number of electrochemically active species including S_8, $S_{8,I}^-$, S_3^-, and to a lesser extent, S_4^-. The exact electrochemical features depend on the time scale of the experiment, and it remains an imposing challenge to obtain kinetic and/or thermodynamic parameters for the key chemical equilibria in the system. However, the use of the new electrochemical cell design should allow determination of the kinetic limitations for processes involved in both lithiation plateaus. This will provide

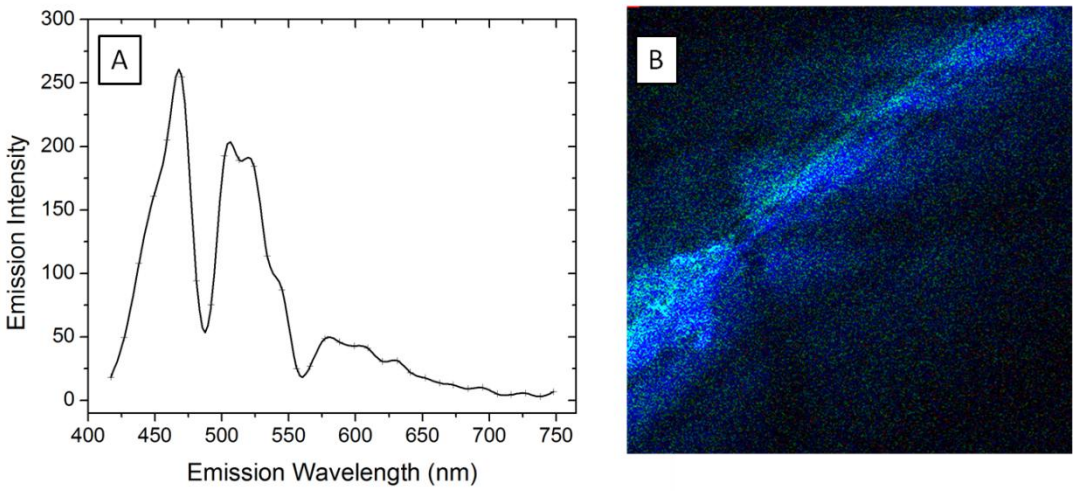

Figure 8-1. Data from confocal fluorescence microscopy on a discharged lithium-sulfur cell. (A) Emission spectra with 385 incident radiation. (B) Map of luminescence, with most color from the region just outside the electrode. Collected with 4x objective. Cell construction and assembly identical to that prepared for the optical microscopy studies in Chapter 7.

critical new insights into the rate capabilities for practical lithium-sulfur batteries. The new cell design will also enable systematic evaluation of how the reactions of polysulfides are altered by new solvent additives, electrode materials or architectures. Based on the critical review in Chapter 4, additional studies of sulfur cathodes by confocal Raman are a promising path towards understanding the complex morphological and chemical processes during sulfur lithiation. The high fluorescence signal observed in the confocal Raman studies also suggests that confocal fluorescence microscopy would be a valuable characterization technique. Luminescence from sulfide-containing materials is a well-known phenomena,[1] but there are at present no systematic reviews of fluorescence from alkali metal sulfides and very few studies of emission spectra from reduced sulfur species[2–4] (i.e. S_x^{n-} versus sulfide compounds such as ZnS). The limited studies focus on the species S_2^- in solid matrices, but do demonstrate that structural and electronic information is available from luminescence studies. Preliminary data acquisition from a discharged lithium sulfur battery (Figure 8-1) indeed shows distinct features (at 460 and 520 nm) and vibronic fine structure

between 500-700 nm. It is significant that this data can be acquired with spatial resolution, in a matter of seconds, and without extended irradiation with intense laser light – all desirable properties for analysis of the sulfur cell. Thus, while significant foundational work remains to develop the technique for the lithium-sulfur system, confocal fluorescence spectroscopy is also a very attractive technique to complement future Raman studies of lithium-sulfur batteries.

8-3. Future Studies -- Lithium-Sulfur Redox Flow Cell

The cell design proposed in Chapter 7 has the additional benefit that it can be used with the solution in static or flowing conditions. In general static solution studies are most useful for fundamental studies of sulfur reduction, while flowing solutions can be used to probe soluble reaction products or to replace the sulfur species present in the reaction volume. The latter mode of operation is particularly important as a means to investigating the concept of a lithium-sulfur redox flow battery, or lithium-sulfur reversible fuel cell.

Fuel cells decouple the energy density of a fuel from the power output of the device, and can be designed to maximize power output from the fuel (lithium) or oxidant (sulfur) by control of electrode composition and solution flow patterns. Historically, fuel cells have been used strictly for energy conversion, such as the electrochemically irreversible reaction of hydrogen and oxygen, and require an external source of chemical energy for indefinite use. However, the use of chemically reversible reactions in a fuel cell means that the system can be regenerated either by replacement of chemical reactants (chemical recharging) or by storing electric charge (electrochemical recharging). This flexibility, combined with the high theoretical specific energy density of the lithium-sulfur system, is the inspiration for a lithium-sulfur fuel cell. The Chiang group has also recently proposed a fuel cell based on lithium chemistry, but focused on the intercalation into a slurry of metal oxide

particles, such as $LiCoO_2$ or $LiTi_4O_5$.[5,6] Lithium-sulfur chemistry has significantly improved gravimetric energy density relative to these systems and fundamentally different interactions with solvent throughout its electrochemical reduction.

Preliminary work has shown that highly concentrated solutions of sulfur (at least 8 M [S]) can be prepared in several different aprotic solvents, including DMF, NMP, TEGDME, and DMAc. Note that this concentration approaches the initial local concentration between the electrodes of typical lithium-sulfur battery cells. These concentrations reach attractive energy densities per unit of solution volume relative to existing redox flow battery technologies (10-20 Wh/kg, or 20-30 Wh/L).[7] Table 7-2 shows predicted energy densities for several different concentrations of lithium-sulfur, and even at moderate concentrations of sulfur the energy density per unit volume is still promising.

Table 8-1. Predicted energy density for sulfur solutions.

Sulfur Concentration [S]	Volumetric Energy Density (Wh/l)	Specific Energy Density (Wh/kg)
Assuming Reduction to Li_2S		
Pure Li and S	3770	2400
10 M [S] as Li_2S_8	725	543
1 M [S] as Li_2S_8	91.1	71.3
0.1 M [S] as Li_2S_8	9.35	7.36
Assuming Reduction to Li_2S_4		
Pure Li and S	941	774
10 M [S] as Li_2S_8	181	136
1 M [S] as Li_2S_8	22.8	17.8
0.1 M [S] as Li_2S_8	2.34	1.84

Volumetric energy density includes volume of lithium anode and electrolyte solution, and assumes formation of ideal solutions. Specific energy density includes the mass of all sulfur and lithium involved in reaction.

One of the greatest challenges for the lithium-sulfur redox flow cell is the varying solubility of the different sulfur species. While Li_2S_8 is soluble to >8 M in common battery solvents, Li_2S_2 and Li_2S are only soluble at or below millimolar levels in ethereal solvents or DMF. Since Li_2S can be formed early in the second plateau (Chapter 6) it may be a significant challenge to prevent fouling the electrode by accumulation of insoluble reduction products. Solubility is a persistent challenge for redox flow cells, with the energy density for a fuel or oxidant typically limited by the limiting concentration of the least soluble species.[8] This is not universally true, since Chiang et al. demonstrate a system in which the active material remains insoluble throughout the course of the reaction. However, it is an imposing challenge to prevent precipitation of highly resistive reduced species at the positions in the electrode where they are generated and their concentration highest.

There are several promising avenues of investigation to circumvent the problem of precipitation. The simplest approach is to control the flow rate so that polysulfides are only reduced to an average oxidation state of Li_2S_4. While the solubility of Li_2S_4 is unknown, initial experiments flowing polysulfides through the lithium-sulfur electrochemical cell suggest that it may be at least 1 M [S]. If chemical equilibria form some insoluble short-chain polysulfides, these can be etched from the surface by comproportionation with long-chain polysulfides.[9] Unfortunately, this approach excludes 75% of the theoretical capacity from a sulfur-containing catholyte (Table 8-1). This disadvantage may be offset by the better rate capability for the first four electrons (Chapter 7). Additional electrochemical studies at different flow rates and concentrations should be able to readily establish the feasibility of this approach.

Table 8-2. High dielectric solvents of interest for preparing polysulfide catholytes

Solvent	*Static Dielectric*	*Viscosity*
N-methyl formamide	186.9	1.65
Dimethyl sulfoxide	46.5	1.99
3-methylsydnone	144.0 (40 C)[10]	5.50 (40 C) [10]
Water	78	1.00

A second approach to avoid precipitation is to change the solvent. High dielectric solvents should more easily solvate the highly charged S_2^- and S_2^{2-} anions. Carbonate solvents such as propylene carbonate ($\varepsilon = 64$) may not be an option due to the reactivity of carbonates with reduced sulfur species,[11] but there are several other promising high-dielectric solvents including dimethyl sulfoxide, sydnones modified with electron-donating groups,[12] or N-methylformamide. Due to the high chemical and dimensional stability of the ceramic solid electrolyte, it may even be an option to use very basic (pH > 13) aqueous catholyte solutions, as is done in polysulfide/bromide redox flow batteries.[8] Alternately, Lewis acids (e.g. BF_3, $AlCl_3$, or tris(pentafluorophenyl)boron[13]) may stabilize the most reduced polysulfides, although the possibility of side reactions would need to be excluded.

Finally, it would be desirable to use an electronically slurry (liquid suspension) that is sufficiently conductive to have sulfur reduced at and deposit on surfaces within the slurry rather the electrode contact. Preliminary attempts used a slurry of carbon black, poly(vinylenedifluoride), and sulfur in DMF, with the sulfur slurry flowed through the cell during application of a constant current. However, even with flowing slurry, the cell voltage transient was similar to the case with a static solution of polysulfides. While a larger absolute capacity was observed when normalized to the

cell volume, the capacity was lower when normalized to the sulfur present in the reaction volume. Furthermore, the effluent slurry no longer contained carbon, and upon cell disassembly the reaction cell volume was packed with deposited carbon. This emphasizes the complicated interactions maintained in the slurry. Deposition of sulfur compounds on the surfaces of conductive particles will inevitably change the interaction of those particles with the solvent/suspension agent, making it difficult to maintain a stable suspension. However, this approach could in principle enable access to much more capacity from the sulfur reduction reaction, and it warrants additional effort with conductive additives of alternate form factors (e.g. wires) and composition (e.g. Ni powders).

8-4. Publications

In the course of this research, productive interactions in either analytical methods or energy storage resulted in the following publications:

1. Stephen Burkhardt, **Michael A. Lowe**, Sean Conte, Weidong Zhou, Hualei Qian, Gabriel G. Rodriguez-Calero, Jie Gao, Richard G. Hennig, and Héctor D. Abruña, "Tailored Redox Functionality of Small Organics for Psuedocapacitive Electrodes", ***Energy Environ. Sci.***, 5 (2012) 7176-7187.
2. Jie Gao, **Michael A. Lowe**, Stephen Burkhardt, and Héctor D. Abruña, "Poly(2,5-Dimercapto-1,3,4-thiadiazole) (PDMcT) as a Cathode for Rechargeable Lithium Batteries with Dramatically Improved Performance", ***Chem. – Eur. J.*** DOI:10.1002/chem.201103535
3. Gabriel G. Rodriguez-Calero, **Michael A. Lowe**, Stephen E. Burkhardt, and Héctor D. Abruña, "Electrocatalysis of 2,5-Dimercapto-1,3,5-thiadiazole by 3,4-Ethylenedioxy-Substituted Conducting Polymers", ***Langmuir***, 27 (2011) 13904-13909.
4. Stephen E. Burkhardt, Sean Conte, Gabriel G. Rodriguez-Calero, **Michael A. Lowe**, Hualei Qian, Weidong Zhou, Jie Gao, Richard G. Hennig, and Héctor D. Abruña, "Towards organic energy storage: characterization of 2,5-bis(methylthio)thieno[3,2-b]thiophene", ***J. Mater. Chem.***, 21 (2011) 9553-9563.
5. Jie Gao, **Michael A. Lowe**, Yasuyuki Kiya, and Héctor D. Abruña, "The Effects of Liquid Electrolytes on the Charge-Discharge Performance of Rechargeable

Lithium/Sulfur Batteries: Electrochemical and In-Situ X-Ray Absorption Spectroscopic Studies", ***J. Phys. Chem. C*** 115 (2011) 25132-25137.

6. Jie Gao, **Michael A. Lowe**, and Héctor D. Abruña, "Spongelike Nanosized Mn3O4 as a High-Capacity Anode Material for Rechargeable Lithium Batteries", ***Chem. Mater.*** 23 (2011) 3223-3227.
7. **Michael A. Lowe**, Yasuyuki Kiya, Jay C. Henderson, and Héctor D. Abruña, "Pendant Thioether Polymer for Redox Capacitor Cathodes", ***Electrochem. Comm.*** 13 (2011) 462-465.
8. Wan Li, Cen Tan, **Michael A. Lowe**, Héctor D. Abruña, and Daniel C. Ralph, , "Electrochemistry of Individual Monolayer Graphene Nanosheets", ***ACS Nano*** 5 (2011) 2264-2270.
9. Yi Liu, **Michael A. Lowe**, Ken D. Finkelstein, Darren S. Dale, Francis J. DiSalvo, and Héctor D. Abruña, "X-ray Fluorescence Investigation of Ordered Intermetallic Phases as Electrocatalysts towards the Oxidation of Small Organic Molecules", ***Chem. – Eur. J.*** 16 (2010) 13689-13697.
10. Stephen E. Burkhardt, Gabriel G. Rodriguez-Calero, **Michael A. Lowe**, Yasuyuki Kiya, Richard G. Hennig, and Héctor D. Abruña, "Theoretical and Electrochemical Analysis of Poly(3,4-alkylenedioxythiophenes): Electron-Donating Effects and Onset of p-Doped Conductivity," ***J. Phys. Chem. C*** 114 (2010) 16776-16784.
11. Yi Liu, **Michael A. Lowe**, Francis J. DiSalvo and Héctor D. Abruña, "Kinetic Stabilization of the Ordered Intermetallic Phases as Fuel Cell Anode Materials," ***J. Phys. Chem. C*** 114 (2010) 14929-14938.
12. Gabriel G. Rodríguez-Calero, **Michael A. Lowe**, Yasuyuki Kiya, and Héctor D. Abruña, "Electrochemical and Computational Studies on the Electrocatalytic Effect of Conducting Polymers toward the Redox Reactions of Thiadiazole-Based Thiolate Compounds," ***J. Phys. Chem. C*** 114 (2010) 6169-6176.
13. Akira Miura, **Michael A. Lowe**, Brian M. Leonard, Chinmayee Subban, Yuji Masubuchi, Shinichi Kikkawa, Richard Dronskowski, Richard G. Hennig, Héctor D. Abruña, and Francis J. DiSalvo, "Silver Delafossite Nitride, AgTaN2," ***J. Solid State Chem.*** 184 (2011) 7-11.
14. Jie Gao, Michael A. Lowe, Héctor D. Abruña, "Manganese Oxide Materials, Methods, and Applications," ***U.S. Patent Application PCT/US12/40360.***

REFERENCES

(1) Smet, P. F.; Moreels, I.; Hens, Z.; Poelman, D. *Materials* **2010**, *3*, 2834–2883.

(2) Aierken Sidike; Kusachi, I.; Kobayashi, S.; Atobe, K.; Yamashita, N. *Phys. Chem. Miner.* **2007**, *35*, 137–145.

(3) Sidike, A.; Sawuti, A.; Wang, X.-M.; Zhu, H.-J.; Kobayashi, S.; Kusachi, I.; Yamashita, N. *Phys. Chem. Miner.* **2007**, *34*, 477–484.

(4) Schulman, J. H.; Kirk, R. D. *Solid State Commun.* **1964**, *2*, 105–108.

(5) Duduta, M.; Ho, B.; Wood, V. C.; Limthongkul, P.; Brunini, V. E.; Carter, W. C.; Chiang, Y.-M. *Advanced Energy Materials* **2011**, *1*, 511–516.

(6) Carter, W. C.; Chiang, Y.-M.; Duduta, M.; Limthongkul, P. High Energy Density Redox Flow Device.

(7) Ponce de Leon, C.; Frias-Ferrer, A.; Gonzalez-Garcia, J.; Szanto, D. A.; Walsh, F. C. *J. Power Sources* **2006**, *160*, 716–732.

(8) Weber, A. Z.; Mench, M. M.; Meyers, J. P.; Ross, P. N.; Gostick, J. T.; Liu, Q. *J. Appl. Electrochem.* **2011**, *41*, 1137–1164.

(9) Rauh, R. D.; Shuker, F. S.; Marston, J. M.; Brummer, S. B. *J. Inorg. Nucl. Chem.* **1977**, *39*, 1761–1766.

(10) Lemire, R. J.; Sears, P. G. *J. Solution Chem.* **1980**, *9*, 553–561.

(11) Gao, J.; Lowe, M. A.; Kiya, Y.; Abruna, H. D. *The Journal of Physical Chemistry C* **2011**, *115*, 25132–25137.

(12) Mascarenhas, R. J.; Shivaraj, Y.; Sherigara, B. S.; Mahadevan, K. M.; Kalluraya, B. *Russ. J. Electrochem.* **2006**, *42*, 776–781.

(13) Xie, B.; Lee, H. S.; Li, H.; Yang, X. Q.; McBreen, J.; Chen, L. Q. *Electrochem. Commun.* **2008**, *10*, 1195–1197.